PRECISION MEASUREMENT OF THE SOUND VELOCITY IN AN ULTRACOLD FERMI GAS THROUGH THE BEC-BCS CROSSOVER

by

James Adlai Joseph

Department of Physics
Duke University

Date:_____
Approved:

_____
Dr. John Thomas, Supervisor

_____
Dr. Steffen Bass

_____
Dr. David Skatrud

_____
Dr. Stephen Teitsworth

Dissertation submitted in partial fulfillment of the
requirements for the degree of Doctor of Philosophy
in the Department of Physics
in the Graduate School of
Duke University

2010

ABSTRACT

(Physics)

PRECISION MEASUREMENT OF THE SOUND VELOCITY IN AN ULTRACOLD FERMI GAS THROUGH THE BEC-BCS CROSSOVER

by

James Adlai Joseph

Department of Physics
Duke University

Date:_____
Approved:

_____
Dr. John Thomas, Supervisor

_____
Dr. Steffen Bass

_____
Dr. David Skatrud

_____
Dr. Stephen Teitsworth

An abstract of a dissertation submitted in partial fulfillment of
the requirements for the degree of Doctor of Philosophy
in the Department of Physics
in the Graduate School of
Duke University

2010

Abstract

A trapped Fermi gas near a collisional resonance provides a unique laboratory for testing many-body theories in a variety of fields. The ultracold Fermi gas produced in our lab is comprised of the lowest two spin states of ^{6}Li. At 834 G there is a collisional or Feshbach resonance between the two spin states. The scattering length between trapped atoms of opposing spins far exceeds the interparticle spacing of the gas. On resonance, a strongly interacting, unitary, Fermi gas is created which exhibits universal behavior. The unitary Fermi gas is a prototype for other exotic systems in nature from nuclear matter to neutron stars and high temperature superconductors.

For magnetic fields less than 834 G the scattering length is positive, and pairs Fermi atoms can form molecular dimers. These dimers, comprised of two fermions, are bosons. At ultracold temperatures the molecular bosons populate the lowest energy level and form a Bose Einstein Condensate (BEC). For magnetic fields greater than 834G the scattering length between fermions in opposing spin states is negative, like Cooper pairs formed between electrons in a superconductor. The Bardeen, Cooper, and Shriefer (BCS) theory was developed to describe the pairing effect in the context of superconductors. In our experiment we produce an ultracold unitary gas. By tuning the magnetic field to either side of the Feshbach resonance we can transform the gas into a weakly interacting BEC or BCS superfluid. Therefore, the region near a Feshbach resonance is called the BEC-BCS crossover.

This dissertation presents a precision measurement of the hydrodynamic sound

velocity in an ultracold Fermi gas near a Feshbach resonance. The sound velocity is measured at various magnetic fields both above and below resonance. Moreover, we are able compare our measurements to theoretical descriptions of hydrodynamic sound propagation. Further, our measurement of sound velocity exactly reproduces the non-perturbative case, eliminating the need to consider nonlinear effects. At resonance the sound velocity exhibits universal scaling with the Fermi velocity to within 1.8% over a factor of 30 in density. In a near zero temperature unitary gas the average sound velocity at the axial center was measured, $c(0)/v_F = 0.364(0.005)$, as well as the universal constant, β = -0.565(0.015). The measurement of sound velocity in an ultracold gas throughout the BEC-BCS crossover provides further evidence of the continuous connection between the physics of the BEC, unitary, and BCS systems.

For Angela

Contents

List of Figures

List of Tables

Acknowledgements

I have always been curious. There is little out there that gives me as much satisfaction as discovery. Growing up, my innate curiosity was encouraged by my parents. For this and for many other reasons I owe a lot to them. They provided a nurturing and supportive environment in which I was encouraged to explore. I also have two very smart older sisters, Nora and Abigayil who have been my life advisors for as long as I can remember. My entire family is still very present, and without their love I would not have been able to accomplish what I have.

My career as a graduate student has provided me with a plethora of learning opportunities. Not only have I been supplied with a series of interesting problems to solve from my class work, but I have also been privileged to be a part of a community where I'm encouraged to ask and answer my own questions. Working in the quantum optics lab with John as my PI has been an extremely fulfilling experience. We get to move beyond the textbook and study new types of matter. John radiates excitement about the work that we are doing. This excitement is contagious and each day I'm curious to see what happens next. It is awe inspiring to think that at any given moment I can be the first person to observe a given phenomena.

It has been a tradition in the lab to list a few of John's more notable quotations and there are a lot of memorable ones. However, I'm more impressed with what he does as opposed to what he says. Not only does he work tirelessly trying to understand the complex and exotic physical systems we produce in our lab, but he is eager to

share that knowledge with the graduate students working for him. On a personal level, he really cares about his students. John has been my advocate in my work as well as in my personal life. There has been many a hug (usually after a couple of glasses of wine but not always) that show how much he cares. Ok, I have to give in to maybe one quote: perhaps my favorite is, "That's so dumb, it just might work!"

These years have been good ones. Certainly, I've derived a lot of satisfaction from my work, but my life outside of the lab has been even more rewarding. I've been able to develop new friendships and expand past relationships. Simply, I have grown. During my time as a graduate student I met Angela. We fell in love and got married. Somewhere in there we got a puppy. I give my thanks to Zoe for convincing Angela to move in with me. It sounds so simple, but developing that relationship is the greatest and most difficult thing that I have ever done (a far second is this dissertation). Angela, you are my love and my life. I wake up each morning thankful that I get to fall asleep next to you each evening. Another benefit of marrying Angela is her folks, now my folks, too. We are lucky to have them live close by and are such loving people that I feel like we are home when ever we visit. Thank you for providing a safe place in sometimes troubled times.

My friends have also been an integral part of my graduate school experience. They allow me to leave the lab and contextualize what I have learned in the broader world. I am grateful in particular for a great friend and one of my best men, Jim who has talked me though a couple of tough decisions over glasses of scotch and is always ready to watch a Duke Basketball game. My other best man and lifelong friend Rob, though farther away geographically, remains close and we visit often. He is a source of tremendous empathy and humor in hard times. I also have to mention the poker

group who has met regularly every week for the past five years. Thanks for the good times, the stimulating discussions, and all the money.

I also feel close to my lab group. The members have changed over the years, but the camaraderie has stayed the same. When I joined the group there were three other graduate students and one post-doc. I worked primarily with Joe and Andrey in the beginning. Perhaps the most important thing I learned from Joe was to think broadly while focusing specifically; He emphasized for me that with an experiment so complicated and interdependent it is necessary to always keep the entire experiment in the back of your head when you are manipulating any single element. Andrey and I were the primary researchers for the sound velocity experiment. We worked a lot of long hours getting that data, and I learned a lot about research. Andrey was always available to answer questions, but perhaps more importantly actually listen to my suggestions even if they were sometimes naive. Thank you Joe for teaching me the ropes, and Andrey for trusting me to teach myself.

Other more senior lab members include Bason and Le. They were always available to answer questions and to brainstorm. Midway through my time here we acquired a new post-doc, Jessie. Goodby dancing Russian, hello Nordic swimmer. Jessie very quickly learned how to operate the experiment, and started making contributions almost immediately. Not only was he a great physicist, but he was a great organizer as well. With the influx of new graduate students, he was able to provide guidance and mentoring. When the system blew up his managing skills were a great asset to the lab. I learned a lot about leading from him.

Now that I am the senior member of the group I hope that I can be as supportive and nurturing as my predecessors. The lab is in good hands with the younger graduate

students. Graduate students Chenglin and Ethan with the help of Post-Doc Jessie have completed building a new experimental system and are currently up and running. I give them a lot of grief, but I think that they are doing a great job and really working hard. Ethan, thanks for the nerd updates and the viral videos. Chenglin, *Bai ishi show how!* Yingyi and Willie are conducting experiments in the other lab. They are hard workers who ask some fantastic and insightful questions. Yinyi, thanks for the photographs; Willie, I'm gonna have to get back to you on some of those questions.

The things that I am most proud of are my marriage, my family, my friends, and my work. I feel that I have contributed to our understanding of the world. I am certain that I have grown to understand myself a whole lot better. Most of all I am pleased to say that I started only one fire with the CO_2 laser, and that was quickly extinguished.

Chapter 1

Introduction

The range and scope of scientific contributions is immense. There are studies whose social impact can be understood immediately while the value of others can only be determined from a historical perspective. The study of archeology tells us where we have been. The study of computer science informs us where we are going. Likewise, in the hard sciences like biology, chemistry, and physics there are many investigations that provide the solid advancements that are required today, and others that are building the basic ground work for future advances.

The inspiration for the first transistor, for example, came about through a study of the material properties of dirty glass [1]. Now, with the advent of the computer chip we are so inundated with computers that it is hard to imagine what life would be like without them. The research presented in this dissertation is a mixture of pure science and practical investigations. Hopefully at some future time it will be recognized as having been a contribution to our understanding of the world. Certainly, our investigations are exploring the vast and promising sphere of the unknown. Our research also has bearing on diverse systems from nuclear matter to neutron stars and high temperature superconductors. The latter is of great practical importance.

In this dissertation I present a measurement of the sound velocity in an ultra-cold Fermi gas. A large amount of research has been conducted in the field of ultra-cold

atom physics. There are two types of basic particles, bosons and fermions, both of which are utilized in atom trapping experiments. In a quantum system where energy levels are discretized, the essential difference between the two basic particles is that multiple bosons are allowed to occupy the same energy level while fermions are not. The study of both of these systems at near zero temperatures is complementary as quantum statistics plays a major role at low temperatures.

Quantum degeneracy was first achieved using bosons with the production of a Bose-Einstein condensate (BEC) in 1995 in three separate labs [2–4]. The cooling of fermions into quantum degeneracy took much longer to achieve. The Pauli exclusion principle inhibits s-wave scattering in single component gases. This difficulty was overcome with the implementation of a Fermi gas comprised of two spin components as well as using a thermal bath of bosons to sympathetically cool fermions.

The production of the first degenerate Fermi gas was achieved in 1999 [5] in a gas comprised of two spin components of ^{40}K. At Duke, our lab produced the first all-optically trapped degenerate gas in 2001 using the two lowest hyperfine states of ^{6}Li. This data was later published in March 2002 [6]. In this gas the two spin components interacted via a negative scattering length. According to the Bardeen Cooper Schriefer (BCS) theory [7], the degenerate Fermi gas under these conditions should exhibit superfluidity. However, it was never possible to cool the gas sufficiently in these experiments to reach superfluidity. In 2001, two groups showed that it was possible to achieve quantum degeneracy through the sympathetic cooling of fermionic ^{6}Li with the bosonic ^{7}Li [8, 9].

Feshbach resonances turned out to be the key to cooling two component gases below the superfluid limit [10]. At a Feshbach resonance the s-wave scattering length between the two components is enhanced. At certain magnetic fields near the res-

onance the scattering length may be positive or negative, on resonance the s-wave scattering length diverges to $\pm\infty$. Because of the large scattering length on resonance, cooling is greatly enhanced and degeneracy is more readily achieved.

At resonance, the scattering length becomes larger than interparticle interaction length and can no longer be used to describe the interactions. As a result, all length scales except the interparticle spacing and thermal de Broglie wavelength disappear from the problem, and the gas may be characterized by the density and temperature. The gas is strongly interacting due to the large scattering length, and because the system is independent of the interatomic potential the gas is considered to be universal [11] or unitary [12, 13]. The production of a degenerate, strongly interacting Fermi gas was first achieved in 2002 by our group [14]. The critical temperature of the unitary gas is much higher than in the BCS regime. Consequently, it is easier to create superfluids in unitary system [15]. This was confirmed with the observation of vortex formation on both sides of the resonance [16]. I will explore the relationship between our current work and other strongly interacting systems namely the Quark-gluon plasma and high critical temperature (T_C) superconductors.

Near the Feshbach resonance the magnetic field can be used to tune the s-wave scattering length from $\pm\infty$ to both small positive and small negative values. It has already been noted that negative values in the scattering length indicate BCS type behavior. When the scattering length is small and positive it is possible to form bound dimmers comprised of the two spin components of the trapped Fermi gas [17]. As a result, we can start with a Fermi gas, and by changing the magnetic field end up with a gas of Bose molecules. Thus, it is possible to tune the s-wave scattering length from negative to positive values through the resonance. We call the entire region the BEC-BCS crossover, as we observe a continuous connection between the physics of

the BCS, unitary, and BEC gases [18]. This dissertation treats of our measurement of the sound velocity in the BEC-BCS crossover [19].

1.1 Motivation for studies

In their seminal papers on the matter, the possibility of a BEC was first proposed by Bose [20] and Einstein [21] back in 1924. BCS theory was introduced in 1956 [7] to explain how bound electron pairs behave in superconductors. In 1969 Eagles drew a connection between BCS and BEC theory [22]. With the advent of the first atom traps [23,24] the production of these theoretical systems became experimentally viable. In 1998 theorists started to tackle the many-body problem of the ground state properties of a Fermi gas with infinite scattering length [25]. It is clear that there is significant interest in the exploration of each individual region of the BEC-BCS crossover.

The wide tunability of the collisional properties of a Fermi gas near a Feshbach resonance allows us to experimentally explore the crossover region. In Section 1.1.1 I will discuss the large amount of theoretical work that attempts to characterize the physics within the BEC-BCS crossover in its constituent parts as well as a continuous theory. For the rest of this section (Sections 1.1.2 and 1.1.3) I will explore the relationship between our current work and other strongly interacting systems namely the Quark-gluon plasma and high critical temperature (T_C) superconductors.

1.1.1 Test bed for crossover theories

One of the great features of a trapped Fermi gas near a Feshbach resonance is that it provides a test bed for a large array of theoretical work because of the great diversity of

the physics than can be accessed. For positive scattering lengths molecular dimers are formed. These dimers, comprised of two fermions, are bosons. The Gross-Pitaevskii equation provides an accurate description of the many-body physics for a dilute Bose gas at low temperatures [26].

A simple mean-field model was developed to provide predictions of the equation of state of the zero temperature gas in the BEC-BCS crossover region [28]. In Section 3.3.2 I extend the results of this theory to provide a prediction of the sound velocity for both the BCS and BEC gases. While this theory does not provide a continuous description of the gas through the entire crossover region, it is easy to understand and allows the humble experimentalist a glimpse into the oftentimes complex theoretical world.

There are many other theoretical investigations that attempt to characterize the equation of state throughout the crossover region. The BCS theory was generalized to describe the crossover in terms of the s-wave scattering length a_s [27]. One result from this theory is that on the BEC side the molecule-molecule scattering length is incorrectly predicted to be $a_{mol} = 2a_s$ [17]. In Chapter 7, I will use our measurement of the sound velocity to show that the molecule-molecule scattering length was correctly predicted by Petrov using a four-body calculation resulting in the value $a_{mol} = 0.6a$ [29]. State of the art Quantum Monte Carlo techniques are now being employed to determine the equation of state of the gas at zero temperature [30, 31].

The purpose of our measurement of the sound velocity near a Feshbach resonance was to provide a measure of the equation of state of the gas through the BEC-BCS crossover region. We use our data to test predictions of the equation of state. In Section 7.3 I compare our sound velocity data to some of the theories mentioned in this section.

1.1.2 Quark-gluon plasma

According to the standard model there are 12 elementary particles, all of which are fermions. Six of these particles are quarks which combine in different ways, sometimes forming baryons such as protons and neutrons. The strong interactions between quarks are mediated by gluons in much the same way as photons mediate the electromagnetic force between charged particles. Under normal conditions quarks are tightly bound together through their exchange of gluons. However, under conditions of extreme density and temperature the quarks can become unbound. A collection of unbound quarks and gluons is called a quark-gluon plasma. A quark-gluon plasma is thought to be the condition of the universe just tens of microseconds after the big bang [32].

Since quarks are fermions, and gluons are mediating strong interactions there is a natural comparison to the resonant fermi gas. Current efforts are underway at Brookhaven National Laboratory's Relativistic Heavy Ion Collider (RHIC) to produce a quark-gluon plasma. Temperatures reached in these experiments exceed 2×10^{12} Kelvin while trapped fermi gases are cooled to hundreds of nK. This is a difference of nearly 19 orders of magnitude in temperature. However, one can see similarities in the behavior of these systems.

At RHIC an experiment was performed in which two gold nuclei accelerated to 100 GeV per nucleon and collided at a glancing blow [33] (i.e. slightly off angle from head on). The deformed nuclear reaction zone is mimicked by the cigar shape our atoms take on in the trapping potential. Both systems exhibit the same "elliptic flow" upon expansion [14]. This type of expansion is evidence that both systems are nearly perfect fluids, [34, 35]. Atom trapping experiments require less resources than collider experiments. Therefore, there is abundant interest in the use of our system

to help investigate strongly interacting systems in the context of nuclear matter [36].

1.1.3 High T_C superconductors

Ordinary metals conduct electricity with some finite resistance, where electron flow is impeded by collisions with other matter resulting in ohmic heating. Certain metals that can conduct electricity without impedance are known as superconductors. Superconducting materials can only conduct without resistance below a certain very cold critical temperature, T_C, marked by a phase transition. Superconductors provide a means of transmitting power without dissipation. The development of superconductors that could operate at room temperatures would have dramatic economic consequences.

Even though there has been an incredible amount of interest in producing high temperature superconductors, currently the highest temperature superconductor needs to be cooled to $T_C \approx 130^\circ$ Kelvin [37]. There has been a lot of effort devoted to understanding the underlying physics of superconductivity. BCS theory [38] posits that spin up and spin down electrons in superconductors couple together into what are called cooper pairs. The connection between the pairs, however, is tenuous and breaks down in the presence of thermal fluctuations. This same pairing effect is found in trapped Fermi gases with negative scattering lengths [39]. It is hoped that research into trapped Fermi gases can help further explain the nature of superconductors.

The exciting thing about trapped fermi gases is that they exhibit phase transitions into a superfluid state and relatively high temperatures [40–44]. The use of the word "relatively" here is important. In our experiments we cool the Fermi gas down to hundreds of nK. The temperature scales of the transition, however, is not governed by absolute temperature but by the ratio of the absolute temperature to the charac-

teristic temperature of the gas, the Fermi temperature, T_F. In resonant Fermi gases it is estimated that the critical temperature is roughly $T_C/T_F = 0.20$ [45]. Consider the fact that typical Fermi temperatures in metals are on the order of thousands of degrees Kelvin. This would translate into a transition temperature in the thousands of degree Kelvin. Therefore, there is a lot of interest in using studies of strongly interacting Fermi gases to help develop the next generation of high temperature superconductors.

1.2 Significance of current work

In our measurement of sound velocity we reach a precision level that allows us to distinguish between a variety of mean-field predictions and quantum Monte Carlo results. In order to accomplish this feat a complete understanding of the system was required. One major accomplishment of this work was the identification of sources of error and bias associated with our measurement (see Chapter 6). Furthermore, our investigations resulted in a large set of data that can be compared to predictions of the equation of state of the gas (see Chapter 7). In Section 1.2.1 I will place our measurement of the sound velocity in the BEC-BCS crossover in the context of recent experimental and theoretical investigations. In Section 1.2.2 I will my contribution to the experiment over the years that resulted in the high level of precision of our measurement.

1.2.1 Original studies of a Fermi gas in the BEC-BCS crossover

Our measurement of the sound velocity near a broad Feshbach resonance [19] provides further evidence of the continuous connection between the BCS and BEC superfluids.

In a gas, the sound velocity c is a function of the derivative of the pressure (P) with respect to density (n),

$$c = \sqrt{\frac{1}{m}\left(\frac{dP}{dn}\right)}, \tag{1.1}$$

where m is the mass of the atoms. The isotropic speed of sound at zero temperature in both the hydrodynamic limit and a superfluid is [46],

$$c = \sqrt{\frac{n}{m}\left(\frac{\partial\mu}{\partial n}\right)_T}, \tag{1.2}$$

where μ is the chemical potential of the gas. The measurement of the sound velocity determines the equation of state, which can be characterized as the relationship between the chemical potential and density.

Existing measurements of release energy [47], momentum distribution [48], and cloud size [49] could also be used for testing the equation of state. Precise interpretation of these measurements, however, would depend on microscopic models. Connecting the release energy to the equation of state requires prior knowledge of the chemical potential. Measurements of momentum distributions depend on the dynamics of magnetic sweeps [50], which turn off the interactions. Cloud size measurements are sensitive to the state of the gas at the edges, which, at finite temperature, may differ from the superfluid core [51] that is probed in the sound speed measurements. Model-independent measurements of collective breathing mode frequencies [52–55] probe only the density scaling of the chemical potential, not the magnitude. As a result, in the universal regime theories with different ground states predict identical breathing mode frequencies [56, 57], but different sound speeds. Moreover, through our experimental investigations we are able to evaluate hydrodynamic models of the sound propagations [46,58,59]. We are also able to compare our data to predictions of

the equation of state from models [60,77] and quantum Monte Carlos calculations [30].

1.2.2 Contributions to the experiment

A great deal of work went into acquiring the data that made this dissertation possible. However, none of my work would have been possible without the enormous efforts expended by other members of our group. Through the work of Ken O'Hara, Stephen Granade, Michael Gehm, Staci Hemmer, and Joe Kinast a complete atom trapping and cooling system was in place when I began working in the quantum optics lab at Duke. The design and implementation of the laser, magnet and vacuum systems, and all of their associated electronics and support systems can be wholly credited to them. Beyond establishing a working experiment, Joe Kinast insured that much system could be automated through computer control. Bason Clancy and Le Luo were busy constructing the new laboratory apparatus at this time, but they were always available to offer insight and assistance when asked.

My introduction to experimental education might be called experiential as I worked on system upgrades. During this period I was assisted by (or, more accurately, I assisted) both Joe and our postdoctoral researcher, Andrey Turlapov. One upgrade, included the replacing of the Coherent 699 Dye Laser with the newer 899 model. I also played a role in the installation of a new locking region as well as a new oven region on the main system. I am proud the say that the oven I helped install back then is still pumping out atoms today. Among the more bizarre problems were the mystery of the exploding circuit board in the CO_2 laser (caused by a coolant leak) and the case of the consistently glitchy magnetic field flipper box (still unsolved). Much of the technical difficulties encountered in the lab have been resolved through the construction of a new experimental apparatus. Our post-doctoral researcher Jessie

Patrika along with graduate students Chenglin-Chan and Ethan Elliot shouldered most of the burden of this project.

While all my early experiences were valuable, there are some experimental exercises of particular relevance to the material covered in this dissertation. First, there was the initial setup of the green laser beam used to excite our sound wave. Next, I developed an alignment procedure to maximize the number of atoms that could be trapped at our coldest temperatures. Also, I was instrumental as our lab produced a fully degenerate BEC for the first time. All of these procedures can be found in Chapter 4. I also developed a way to measure the condensate fraction from 1-dimensional density profiles. This procedure for measuring condensate fraction is outlined in Appendix B. A large amount of care was taken to make sure we removed all sources of systematic error in our measurement. To this end we developed correction factors for both systematic errors due to the shape of the trapping potential and for bias in the atom number measurement. I take personal pride in developing a way to take into account a systematic shift in the atom number, the details of which can be found in Chapter 6. Also included in this dissertation is a description of a simple mean field model (see Section 3.3.2). This theory does not provide a continuous description of the gas through the entire crossover region, however, it is easy to understand. It offers some insight into the oftentimes bewildering models developed by our theorist counterparts. Often times we rely too heavily on theoretical results without a completely understanding how they are produced. I thought it important to include at least one detailed description of some of the modeling that occurs in our field.

The shear amount of time spend grinding out sound data during the experiment gives me a sense of accomplishment. Nearly a hundred data points are included in the final graphs showing the sound velocity over the BEC-BCS crossover in Chapter

7. Each point consists of about 50 experimental runs. In addition, we performed a separate breathing mode experiment that corresponds to each data point. Factoring in the vigilance takes to keep the system performing at an optimal capacity underscores my satisfaction with this data set. Persistence is perhaps one of the essential ingredients in our field.

Even beyond honing a keen understanding of the underlying physics of the system, the field of atom trapping and cooling requires one to develop a diverse skill set including but not limited to a working knowledge of vacuum systems, laser system, electronics, plumbing, computer programming, and analysis. Above all of this is the essential skill of collaboration. I owe my own in-depth understanding of our experimental system to the encouragement and support of more senior members of the group. Perhaps my greatest satisfaction of all comes from passing that knowledge down to our groups next generation of experimentalists.

1.3 Dissertation organization

Chapter 1, the current chapter, provides an introduction to this dissertation and places our experimental work in a historical context and in relation to current work in multiple fields. Chapter 2 provides the basic theoretical background required for understanding the trapping of Fermi gases near a Feshbach resonance. In it I outline the physics of a dipole trap and a Fermi gas trapped in a confining potential. Chapter 2 also offers a discussion of the electronic states of ^6Li in a magnetic field and the s-wave scattering length near a Feshbach resonance. Finally, I include an overview of the zero Temperature theories associated with the limits near a Feshbach resonance (ideal gas, unitary gas, and weakly interacting Bose gas).

In Chapter 3, I present the theory of hydrodynamic sound propagation and apply it to our trapped gas. I determine the theoretical zero temperature sound velocity in the limits near a Feshbach resonance and discuss the propagation dynamics of a density wave in a trapped gas with density variation as opposed to a homogenous system. Also highlighted in Chapter 3 is a description of a simple mean field model of the equation of state and how it can be extended to provide a prediction of the sound velocity in the BEC-BCS crossover.

In order to fully understand the sound experiment, it is necessary to provide a description of the underlying experimental apparatus. Chapter 4 summarizes the basic experiment as it is employed in our lab. I Include a description of the apparatus, the physics underlying each stage of the experimental procedure, and important cooling and trapping techniques. Also included in chapter for are the experimental procedure required to produce a near zero temperature gas in the limits near a Feshbach resonance.

Chapter 5 details the sound velocity experiment. It begins with the experimental set up of the blue detuned beam used to excite sound waves in our experiment. Included in Chapter 5 is an analysis of the propagation dynamics of a density perturbation in a trapped gas, outlining how we extract a value for the speed of sound. In addition to the sound measurement, I describe the complementary measurements needed to characterize the characteristic energy of the gas, the Fermi energy E_F.

Chapter 6 introduces the concepts of systematic and statistical errors. I provide the error analysis of our measurement. I show how we determine correction factors for both the anharmonisty of the trap as well as the atom number. At the end of this chapter I highlight exactly how we extract a single normalized sound velocity value and its associated error.

Finally, In Chapter 7 I discuss the results of our experiment. I show why the theory of hydrodynamic sound propagation [58] we highlight in Chapter 3 is correct. I also discuss how we can characterize different regions of the crossover with the dimensionless parameter $1/(k_F a)$ where a is the s-wave scattering length and k_F is the Fermi wave number. The data is displayed along with zero-temperature theories associated with the limits of the BEC-BCS crossover, many-body theoretical predictions of the equation of state, and state of the are many body nonperturbative quantum Monte Carlo calculations.

I conclude this dissertation in Chapter 8. Here, the sound velocity experiment and the results we obtained are summarized. I speculate on improvements to the experimental apparatus and outline some key experimental concepts I feel are seminal to conducting a good experiment. The blue detuned beam used to excite our sound waves is a powerful experimental tool that I hope will be utilized in future experiments. At the end of Chapter 8 I outline a few experiments that can be preformed in the future.

There are 3 appendices following the bulk of this dissertation. Appendix A provides a table our sound data presented in the plots of Chapter 7. Appendix B explains how we can characterize the one dimensional profiles of finite temperature BECs and extract a condensate fraction. Appendix C provides the mathematica code used to produce the simple mean field curves.

Chapter 2

Trapped Fermi gases with tunable interactions

The field of atom trapping and cooling has experienced a boom over the past few decades. Ever more complicated experiments and theories are performed and developed on a daily basis. In this chapter I will attempt to cover the basic theory that is essential in understanding trapped Fermi gases. We need to understand all complexities pertaining to our system of interest in order to perform a precision measurement of the sound velocity.

The model system that is at the heart of all of our experiments is the ideal Fermi gas in a harmonic potential. This basic system is covered in most texts on thermodynamics [69], [72]. It is the natural starting point for studies of trapped Fermi gases. In our lab the trapped atoms are confined in optical fields. Section 2.1 describes the physics of a dipole trap generated by a focused laser beam. Next, in Section 2.2 I will describe the physics of a harmonically trapped ideal Fermi gas.

In our experiment we trap the two lowest hyperfine states of ^{6}Li. The interactions between atoms in these two states greatly effects the physics of the system. These interaction depend on an external magnetic field. In Section 2.3 I begin with a description of the electronic ground states of ^{6}Li. Next, I describe the scattering

process between to two the lowest hyperfine states of ^{6}Li. The presence of a collisional (Feshbach) resonance (see Section 2.3.3) allows us to alter the basic nature of our trapped gas. In our experiment we can access ideal and weakly interacting Fermi systems, strongly interacting systems, and weakly interacting Bose systems by tuning the magnetic field. In our experimental system there are magnetic fields at which the physics of the trapped atoms is representative of a particular theory. Presented in Section 2.4 are the various zero temperature theories associated with:

- An ideal gas
- A unitary Fermi gas
- A weakly interacting BEC.

Each of these systems has a different equation of state. Our sound velocity experiment provides evidence of a continuous connection between diverse physical systems. This chapter provides the basic zero temperature thermodynamic relationships a for well understood systems in the limits near a Feshbach resonance.

2.1 Atomic dipole trapping potential

In our experiment atoms are trapped at the focus of a CO_2 laser. The wavelength of the CO_2 laser is far detuned from the atomic resonance of the trapped atoms. At the focus of the laser is a large electric field gradient. An atom in the presence of an electric field will polarize. The induced atomic dipole is aligned along the electric field lines. The atom is then drawn towards the center of the laser focus where the electric field is strongest.

In our experiment, the electric field is generated by a Coherent DEOS LC100-NV CO_2 laser. The wavelength of the laser is $\lambda_{CO_2} = 10.6\,\mu$m, which is far detuned from the wavelength of the atomic resonance of the ^{6}Li atoms, $\lambda_{^6Li} = 671$ nm. The induced atomic dipole depends upon the field detuning and the atomic polarizability. A ^{6}Li atom will be accelerated by the interaction between induced dipole and the electric field gradient. The potential associated with the force an atom feels $\mathbf{F_{dip}} = -\nabla V_{dip}$ is given by [62, 63],

$$V_{dip} = -\frac{1}{2}\alpha\overline{\mathbf{E}^2}, \tag{2.1}$$

where the bar indicates that the electric field is averaged over many cycles. As we are working with an optical field we can assume a sinusoidal variation in the electric field such that $\mathbf{E}^2 = \mathcal{E}^2/2$, and the dipole potential can be written in terms of the field intensity $I = c\mathcal{E}^2/8\pi$,

$$V_{dip} = -\frac{2\pi}{c}\alpha I, \tag{2.2}$$

where c is the speed of light. I and c are positive quantities. Therefore, in order for the potential to be attractive the polarizability α must be positive.

The polarizability for the ground state of ^{6}Li is [62]

$$\alpha = \frac{\alpha_0\omega_0^2}{\omega_0^2 - \omega^2}, \tag{2.3}$$

where $\alpha_0 \equiv 2\mu_{eg}^2/\hbar\omega_0$ is the static polarizability, ω_0 is the atomic transition frequency, and ω is the frequency of the incident light. μ_{eg} is the dipole matrix element between the ground and excited state of the atom. For our experiment, the static polarizability is $\alpha_0 = 24.310^{-24}cm^3$ [68]. We use a CO_2 laser beam for our trapping potential because it far detuned from the atomic resonance frequency (i.e. $\omega \ll \omega_0$). This

means that the atomic polarizability of a ^{6}Li atom in the electric field of the laser is approximately equal to the static polarizability,

$$\alpha \approx \alpha_0. \tag{2.4}$$

The fact that our polarizability is positive indicates that our potential will indeed be attractive.

The laser itself is extremely stable and, as a result of the far detuned frequency and long wavelength, there is a very small probability of scatter. Approximately 1 photon per atom will be scattered every 40 minutes [45]. This means that the lifetime of the atoms in our dipole trap is very long, see Figure 2.1. The loss of atoms from the trap can be attributed to very small effects such as position and intensity noise in the CO_2 beam and background gas collisions. In his dissertation Ken O'Hara provides an in depth discussion of these effects [14].

The geometry of the trapping potential is reflected in the shape of the laser beam focus. For a gaussian beam propagating in the z-direction the intensity is

$$I(x,y,z) = \frac{I_0}{1+z^2/z_0^2} e^{-2\frac{x^2}{x_0^2}-2\frac{y^2}{y_0^2}}, \tag{2.5}$$

where I_0 is the maximum beam intensity and x_0, y_0, and z_0, determine the spatial size of the beam. The Rayleigh range, z_0, depends on the beam profile according to $z_0 = \pi x_0 y_0/\lambda$. The resultant potential is,

$$V_{dip}(r,z) = \frac{V_0}{1+z^2/z_0^2} e^{2\frac{x^2}{x_0^2}-2\frac{y^2}{y_0^2}}, \tag{2.6}$$

where $V_0 = \frac{2\pi}{c}\alpha_0 I_0$ is the maximum depth of the potential. The geometry of the laser

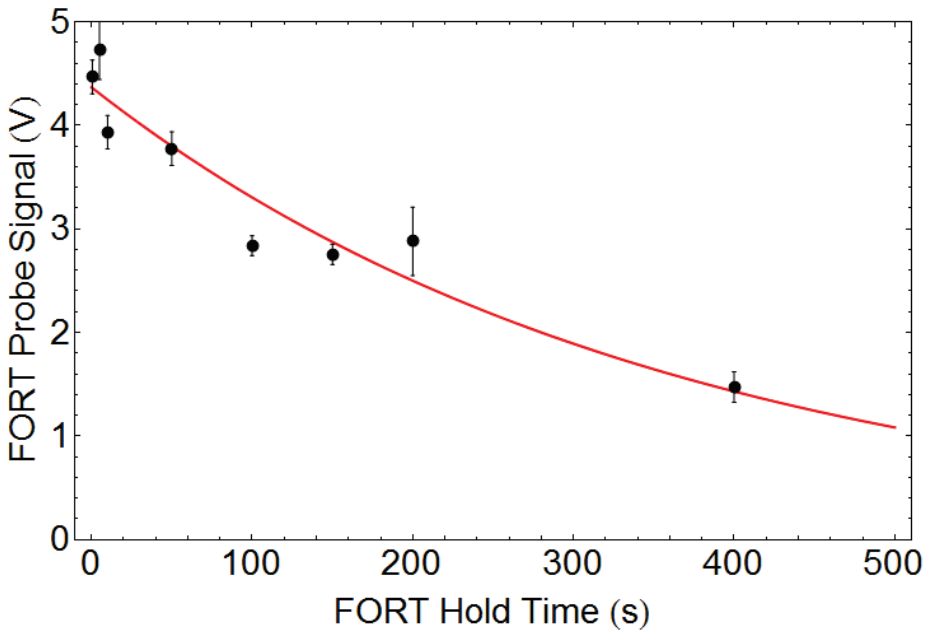

Figure 2.1: The atomic signal of atoms held in an ultra stable CO_2 beam trap for a variable amount of time. The lifetime of the signal is limited by background gas collisions. A measure of the number of atoms left in the trap is obtained by probing with on resonant light and observing the atomic florescence signal on a photomultiplier tube. We see an exponential decay in the atomic florescence signal with a $1/e$ time of 358 seconds, (nearly 6 minutes).

beam focus is often referred to as "cigar-shaped". The axial (z-direction) size of the trap is much larger than in than the radial (x- and y- direction) size. Further, the trap is nearly cylindrically symmetric (i.e. $x_0 \approx y_0$).

The trap depth is much larger than the characteristic energy of the Fermi gas, E_F. The laser beam is focused to a spot size of about $x_0 = y_0 = 50\ \mu m$ and has about P = 60 Watts of power. The intensity of the laser beam on the atoms is thus $I_0 = 2P/(\pi x_0 y_0)$. This translates to a trap depth of $V_0/k_B \approx 550\ \mu$Kelvin in temperature units.

In our experiment, the trapped atoms occupy the deepest portion of the optical potential where V_{dip} are well approximated by a harmonic potential. The approximation for the external harmonic trapping potential is,

$$V_{dip}(r,z) \approx -V_0 + \frac{1}{2}m\omega_x^2 x^2 + \frac{1}{2}m\omega_y^2 y^2 + \frac{1}{2}m\omega_z^2 z^2, \tag{2.7}$$

where $\omega_{x,y} = \sqrt{2V_0/mx_0^2, y_0^2}$, and $\omega_z = \sqrt{4V_0/mz_0^2}$. Note that the harmonic potential has an offset, $-V_0$ that does not vary spatially and therefore imparts no force on the atoms. This term can be dropped by referring the energy to the bottom of the trap. In the harmonic approximation our external trapping potential V_{ext} is,

$$V_{HO}(x,y,z) = \frac{1}{2}m\omega_x^2 x^2 + \frac{1}{2}m\omega_y^2 y^2 + \frac{1}{2}m\omega_z^2 z^2. \tag{2.8}$$

For some of our measurements we see a systematic error due to anharmonic effects. In latter chapters I will develop anharmonic correction factors using a gaussian shaped

trapping potential for V_{ext},

$$V_{GA}(x,y,z) = V_0\left(1 - e^{-\frac{m\omega_x^2}{2V_0}x^2 - \frac{m\omega_y^2}{2V_0}y^2}\right) + \frac{1}{2}m\omega_z^2 z^2. \tag{2.9}$$

At lower trap depths where the anharmonic effect is greatest, there is additional confinement due to the magnetic field gradient of the applied magnetic fields. At our lowest trap depths, the magnetic confinement dominates the axial (z-direction) trapping potential. Therefore, in equation (2.9) the variation in the z-direction remains harmonic.

2.2 Fermi gas in a harmonic trap

Our discussion of trapped gases begins with a noninteracting (ideal) Fermi gas trapped in a harmonic potential. This is a natural starting point, as ideal Fermi gases are a well explored physical system covered in the standard undergraduate thermodynamic texts [69]. Furthermore, we can produce an ideal Fermi gas in our laboratory. This allows us to run experiments that will be compared to experimentally useful theory has been worked out in recent papers [18, 73], in order to check for our experimental methodology.

Our goal in this section is to determine the relationship between the thermodynamic variables of a trapped ideal Fermi gas. In the previous section we determined that the harmonic approximation of a dipole trapping potential was, (equation (2.8),

$$V_{HO}(\mathbf{r}) = \frac{1}{2}m\omega_x^2 x^2 + \frac{1}{2}m\omega_y^2 y^2 + \frac{1}{2}m\omega_z^2 z^2, \tag{2.10}$$

where ω_i is the trap frequency in one spatial dimension and m is the atomic mass.The

harmonic oscillator energy levels associated with a single particle trapped in this potential are,

$$\epsilon(n_x, n_y, n_z) = \hbar(\omega_x n_x + \omega_y n_y + \omega_z n_z), \tag{2.11}$$

where n_i is a non-negative integers and the 1/2 zero point energy factors have been dropped.

Given that no two fermions can occupy the same energy level, and that our experiments contain a large number of atoms, the total energy of the system far exceeds the level spacing ($E_0 \gg \hbar\omega_i$). Therefore, we can replace the discrete single particle spectrum with a continuous density of states,

$$g(\epsilon) = \frac{\epsilon^2}{2(\hbar\overline{\omega})^3}, \tag{2.12}$$

where $\overline{\omega} = (\omega_x\omega_y\omega_z)^{1/3}$ is the average trap frequency. The Fermi occupation number as a function of energy is,

$$f(\epsilon) = \frac{1}{\exp[(\epsilon - \mu)/(k_B T)] + 1}, \tag{2.13}$$

ϵ is the energy, μ is the chemical potential, k_B is Boltzmann's constant, and T is the temperature.

To solve for thermodynamic quantities we normalize the total occupation number to the total number of atoms. The total number of atoms in a system can be calculated by integrating the product of the density of states and Fermi occupation number over the range of energies available,

$$\frac{N}{2} = \int_0^\infty \frac{g(\epsilon)}{\exp[(\epsilon - \mu)/(k_B T)] + 1} d\epsilon. \tag{2.14}$$

In our experiment we trap the lowest two hyperfine states of ^{6}Li. According to the pauli exclusion principle it is perfectly acceptable for one atom from each states to occupy a single energy level. Therefore, there are twice as many atoms occupying all of the available energy levels. Taking this into account we have introduced a factor of 1/2 to the left hand side of equation (2.14).

For the zero temperature condition, the integral in equation (2.14) simplifies greatly. The Fermi occupation number becomes one for all energies less than or equal to the Fermi energy and zero for all energies greater than E_F. Combining equations (2.12), 2.13, and 2.14, the total atom number at zero temperature is,

$$N = \frac{1}{(\hbar\overline{\omega})^3}\int_0^{E_F} \epsilon^2 d\epsilon, \tag{2.15}$$

where E_F is the Fermi energy. E_F is the characteristic energy the system. From equation (2.15) we can solve for the Fermi energy in terms of the measurable quantities $\overline{\omega}$ and N,

$$E_F = \hbar\overline{\omega}(3N)^{1/3}. \tag{2.16}$$

Quantities that depend on trap totals such as $\overline{\omega}$ and N are termed global. In equation (2.14) the chemical potential μ is given implicitly as a function of temperature and atom number. For the zero temperature condition, the global chemical potential is equal to the Fermi energy,

$$\mu_G = \hbar\overline{\omega}(3N)^{1/3}, \tag{2.17}$$

For a complete description of our trapped gas, we would like to determine the local equation of state as well. Local thermodynamic variables like density $n(\mathbf{r})$ vary throughout the trap (i.e. the gas more dense in the center of the trap and less dense

at the edges). The discussion of local quantities needs to be set up carefully. We can make certain assumptions based on our experimental system. The semiclassical approximation, or Local Density Approximation (LDA) assumes that there is a large number of atoms contained in a small volume, and that the external potential varies slowly over this small volume. A complete discussion as to what constitutes these "small" and "large" values can be found in reference [73].

Assuming that the LDA holds we can calculate local quantities from the Hamiltonian of a single particle moving in the presence of an external potential V_{ext},

$$\mathcal{H}(\mathbf{r},\mathbf{p}) = \frac{1}{2m}(p_x^2 + p_y^2 + p_z^2) + V_{ext}(\mathbf{r}). \tag{2.18}$$

By integrating the Fermi occupation number, equation (2.13), as a function of the Hamiltonian over all momentum space we can calculate the density,

$$n(\mathbf{r}) = \frac{1}{(2\pi\hbar)^3}\int f(\mathcal{H}(\mathbf{r},\mathbf{p}))d^3p. \tag{2.19}$$

We can simplify this integral by using the properties of the delta function, $\delta(x)$,

$$F(x) = \int F(y)\delta(y-x)dy. \tag{2.20}$$

We use the above delta function condition to set,

$$f(\mathcal{H}(\mathbf{r},\mathbf{p})) = \int f(\epsilon)\delta(\epsilon - \mathcal{H}(\mathbf{r},\mathbf{p}))d\epsilon. \tag{2.21}$$

As a result, the equation for density becomes

$$n(\mathbf{r}) = \frac{1}{(2\pi\hbar)^3} \int \int f(\epsilon)\delta(\epsilon - \mathcal{H}(\mathbf{r}, \mathbf{p}))d^3p\, d\epsilon. \tag{2.22}$$

This integral with the Hamiltonian expressed in terms of the momentum and harmonic trapping potential is,

$$n(\mathbf{r}) = \frac{1}{(2\pi\hbar)^3} \int f(\epsilon) \int \delta\left(\epsilon - \frac{p_x^2 + p_y^2 + p_z^2}{2m} - V_{ext}(\mathbf{r})\right) d^3p d\epsilon \tag{2.23}$$

After we perform the momentum integral in spherical coordinates we find an equation for density in terms of an integral over energy,

$$n(\mathbf{r}) = \frac{\sqrt{2}(m)^{3/2}}{\pi^2\hbar^3} \int f(\epsilon) \int (\epsilon - V_{ext}(\mathbf{r}))^{1/2}\Theta\left(\epsilon - V_{ext}(\mathbf{r})\right) d^3p d\epsilon, \tag{2.24}$$

where Θ is the heavyside function which restricts the integration to energy values $V_{ext}(\mathbf{r}) < \epsilon$. As $V_{ext}(\mathbf{r})$ varies in space, this restriction translates into a spatial restriction on the density. In the zero temperature case the Fermi occupation number is one for all energies below the Fermi energy (which is equal to the global chemical potential μ_G) and zero elsewhere. This gives the integral

$$n(\mathbf{r}) = \frac{\sqrt{2}(m)^{3/2}}{\pi^2\hbar^3} \int_0^{\mu_G} f(\epsilon) \int (\epsilon - V_{ext}(\mathbf{r}))^{1/2}\Theta\left(\epsilon - V_{ext}(\mathbf{r})\right) d^3p d\epsilon. \tag{2.25}$$

By performing the integral we can solve for the density,

$$n(\mathbf{r}) = \frac{(2m)^{3/2}}{3\pi^2\hbar^3}(\mu_G - V_{ext}(\mathbf{r}))^{3/2}. \tag{2.26}$$

The equation for density above is valid for regions in space where $V_{ext}(\mathbf{r}) < \epsilon$, and

the density will be zero in all other regions. Solving for μ_G yields,

$$\mu_G = \frac{\hbar^2(3\pi^2)n(\mathbf{r})^{2/3}}{2m} + V_{ext}(\mathbf{r}). \tag{2.27}$$

The above equation is the main result of the LDA for an ideal Fermi system at zero temperature. In this form, we relate the overall chemical potential of the system, μ_G to the trap potential and $\epsilon_F = \frac{\hbar^2(3\pi^2)n(\mathbf{r})^{2/3}}{2m}$ the local Fermi energy. Thus our equation of state for an ideal Fermi gas is,

$$\mu_L(\mathbf{r}) = \frac{\hbar^2(3\pi^2)^{2/3}}{2m} n(\mathbf{r})^{2/3}, \tag{2.28}$$

where μ_L is the local chemical potential, which for a zero temperature gas is equal to the local Fermi energy. And the primary result of the LDA can be restated as,

$$\mu_G = \mu_L(\mathbf{r}) + V_{ext}(\mathbf{r}). \tag{2.29}$$

We can consider the equation (2.29) as a good starting point for calculating thermodynamic quantities in the BEC-BCS crossover region where the atomic interaction energy is non-zero. The local chemical potential relates the density of the gas to energy. It can be viewed as the mean field energy of the interparticle interaction at zero temperature. The local chemical potential at zero temperature is the equation of state of the gas from which we will determine the density profile in an external potential.

We show later that a general power law form of the equation of state,

$$\mu_L(\mathbf{r}) = \mathcal{C} n(\mathbf{r})^{\gamma}, \tag{2.30}$$

can be used to treat both Bose and Fermi gases. That means that for the ideal Fermi gas discussed above, $\mathcal{C} = \hbar^2(3\pi^2)^{2/3}$ and $\gamma = 2/3$. The global chemical potential for any gas trapped in an external potential that follows the power law equation of state can then be determined by normalizing the density to the total number of atoms in a trapping potential,

$$N = \int n(\mathbf{r}) d^3r, \tag{2.31}$$

$$N = \int \left(\frac{\mu_G}{\mathcal{C}}\right)^{1/\gamma} \left(1 - \frac{V_{ext}(\mathbf{r})}{\mu_G}\right)^{1/\gamma} d^3r. \tag{2.32}$$

2.3 Tunable interactions

We trap the two lowest hyperfine states of ^{6}Li in our experiment. As stated previously we use an applied magnetic field to tune the interactions between these two states. This section begins by describing the hyperfine splitting of the ground state of ^{6}Li. The interaction between the two lowest hyperfine states depends upon the scattering length. Therefore, we will continue our discussion with the derivation of the s-wave scattering length a_s and the atomic crosssection σ. Further, the presence and significance of a collisional (Feshbach) resonance between the two lowest hyperfine states will be explored.

2.3.1 Electronic states of ^{6}Li

The majority of atom trapping experiments utilize alkali metals atoms. Their relatively simple atomic structure and spectra make them prime candidates for optical trapping techniques. Many of the basic trapping and cooling techniques described in Chapter 4 take advantage of the hyperfine structure and Zeeman shifted energy levels

of our trapped atoms. Therefore, It is useful to present the hyperfine structure and Zeeman tuning of the ^{6}Li ground state.

The ^{6}Li atom is an isotope of lithium, a fermion composed of 3 protons, 3 neutrons, and 3 electrons. The ground state of ^{6}Li has a nuclear spin I = 1, and the unpaired valence electron is in the 2s orbital. This means that the total angular momentum quantum number is L = 0, and the spin is S = 1/2. The total angular momentum quantum number which depends on I, L, and S has two possible values in the ground state, F = 1/2 and F = 3/2. The degeneracy of the ground state is then six fold, arising from all possible spin projections of the total angular momentum quantum number. In the F = 1/2 manifold the spin projections are $m_F = \pm 1/2$ and in the F = 3/2 manifold the spin projections are $m_F = \pm 1/2$ and $m_F = \pm 3/2$. When an external magnetic field is applied the degenerate states split giving 6 distinct energy eigenstates.

We can solve for these eigenstates using the hyperfine and Zeeman Hamiltonian,

$$H_{int} = \frac{a_{hf}}{\hbar^2}\mathbf{S}\cdot\mathbf{I} + \frac{\mu_B}{\hbar}\left(g_J^{gnd}\mathbf{S} + g_I\mathbf{I}\right)\cdot\mathbf{B}, \tag{2.33}$$

which contains a term for the hyperfine splitting due to the magnetic dipole interaction between the nuclear and electronic spins as well as the interaction of the nuclear and electronic spins with an external magnetic field $\mathbf{B}$. In the above equation a_{hf}/h = 152.137 MHz is the magnetic dipole constant, g_J^{gnd}=2.002 is the total electronic g-factor for the ground state, g_I = -0.000448 is the total nuclear g-factor, and μ_B/h= 1.3996 MHz/gauss is the bohr magneton.

The eigenstates of equation (2.33) are [74].

$$|1\rangle = \sin\Theta_+|\frac{1}{2},0\rangle - \cos\Theta_+|-\frac{1}{2},1\rangle \tag{2.34}$$

$$|2\rangle = \sin\Theta_-|\frac{1}{2},-1\rangle - \cos\Theta_-|-\frac{1}{2},0\rangle \tag{2.35}$$

$$|3\rangle = |-\frac{1}{2},-1\rangle \tag{2.36}$$

$$|4\rangle = \cos\Theta_-|\frac{1}{2},-1\rangle + \sin\Theta_-|-\frac{1}{2},0\rangle \tag{2.37}$$

$$|5\rangle = \cos\Theta_+|\frac{1}{2},0\rangle + \sin\Theta_+|-\frac{1}{2},1\rangle \tag{2.38}$$

$$|6\rangle = |\frac{1}{2},1\rangle, \tag{2.39}$$

where the kets $|m_S, m_I\rangle$ give the electronic and nuclear spin projections, $m_S = \pm 1/2$ and $m_I = -1, 0, 1$. Further the coefficients $\sin\Theta_\pm$ and $\cos\Theta_\pm$ in the above equations are given by,

$$\sin\Theta_\pm = \frac{1}{\sqrt{1+(Z_\pm + R_\pm)^2/2}} \tag{2.40}$$

$$\cos\Theta_\pm = \sqrt{1-\sin^2\Theta_\pm} \tag{2.41}$$

$$Z_\pm = \frac{\mu_B B}{a_{hf}}(g_J^{gnd} - g_I) \pm \frac{1}{2} \tag{2.42}$$

$$R_\pm = \sqrt{Z_\pm^2 + 2}, \tag{2.43}$$

which depend upon terms in the internal hamiltonian and the external magnetic field.

The energy eigenvalues E_n associated with the eigenstates $|n\rangle$ are

$$E_1 = -\frac{1}{4}(a_{hf} - 2g_I\mu_B B + 2a_{hf}R_+) \quad (2.44)$$

$$E_2 = -\frac{1}{4}(a_{hf} + 2g_I\mu_B B + 2a_{hf}R_-) \quad (2.45)$$

$$E_3 = \frac{1}{2}(a_{hf} - 2g_I\mu_B B - g_J^{gnd}\mu_B B) \quad (2.46)$$

$$E_4 = \frac{1}{4}(-a_{hf} - 2g_I\mu_B B + 2a_{hf}R_-) \quad (2.47)$$

$$E_5 = \frac{1}{4}(-a_{hf} + 2g_I\mu_B B + 2a_{hf}R_+) \quad (2.48)$$

$$E_6 = \frac{1}{2}(a_{hf} + 2g_I\mu_B B + g_J^{gnd}\mu_B B). \quad (2.49)$$

The energy eigenvalues are dependent on the magnetic field. As shown in Figure 2.2 at zero field there are just degenerate two energy levels, F = 1/2 and F = 3/2 split by $3/2a_{hf}$. When the field is applied the degeneracy in the system is lifted and there are six energy levels. In our experiments we trap the two lowest hyperfine ground states, $|1\rangle$ and $|2\rangle$.

2.3.2 Atomic cross section and scattering length

Elementary quantum mechanics textbooks, [70,72], as well as previous theses [62,65], cover the scattering problem of two quantum particles. However, a basic review is called for as the scattering of two fermions in a trapped gas is an essential element in the production of degenerate Fermi gases. The s-wave scattering length and the atomic cross section provide a measure of the interaction strength between two lowest hyperfine states of ^{6}Li.

We can determine the atomic cross section and scattering length in light of the basic scattering problem. A quantum particle-particle interaction can be viewed from

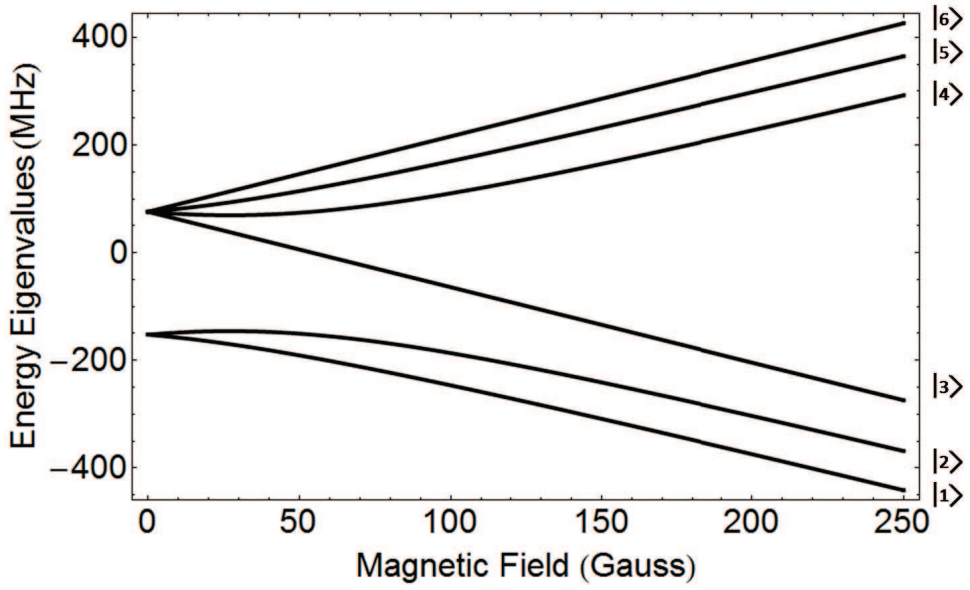

Figure 2.2: The hyperfine energy eigenvalues for the ^{6}Li ground state in frequency units versus magnetic field. In the experiment a 50/50 mixture of the lowest two energy eigenstates ($|1\rangle$ and $|2\rangle$) are trapped.

the vantage frame of one stationary particle, the target, with the second particle incident. We can view the incident particle as a stream of particles acting as a plane wave with a wave vector $\mathbf{k}$ before the scattering event and a spherical wave with a wave vector $\mathbf{k}'$ after the scattering event. The outgoing spherical wave amplitude is a function of the ingoing and outgoing wave vectors, $f(\mathbf{k}, \mathbf{k}')$ and can be related to the differential scattering cross section $d\sigma/d\Omega$ via the equation,

$$\frac{d\sigma}{d\Omega} = |f(\mathbf{k}, \mathbf{k}')|^2 d, \tag{2.50}$$

where the differential cross section is the probability of observing a scattered particle in units of the solid angle ($\Delta\Omega$) at a specific solid angle.

Our stream of particles is incident on another particle so we can assume a solid

sphere potential for the interaction. We can then express the outgoing spherical wave amplitude in terms of the angle θ between $\mathbf{k}$ and $\mathbf{k}'$,

$$f(\theta) = \sum_{l=0}^{\infty} (2l+1) f_l(k) P_l(\cos\theta), \tag{2.51}$$

where l is a non negative integer representing the angular momentum order, and $P_l(\cos\theta)$ are Legendre polynomials. At a specific angular momentum values the relationship between the outgoing wave amplitude and the scattering phase shift δ_l is

$$f_l(k) = \frac{e^{i\delta_l}\sin(\delta_l)}{k}. \tag{2.52}$$

Further, we can make the argument that for a cold gas the energy associated with the interaction between two particles very small such that $l = 0$ [64, 65]. This means that the collisions of interest are s-wave. When we combine equations (2.50) and (2.52) we find the result for the atomic cross section,

$$\sigma = \frac{4\pi \sin^2(\delta_0)}{k^2}. \tag{2.53}$$

The definition for the s-wave scattering length [71] is

$$a_s \equiv -\lim_{k\to 0} \frac{\tan(\delta_0)}{k}. \tag{2.54}$$

Therefore, the atomic cross section as a function of the s-wave scattering length and the wave vector, k, of an atom is,

$$\sigma = \frac{4\pi a_s^2}{1 + k^2 a_s^2}. \tag{2.55}$$

In the limit where the s-wave scattering length is small compared to the wave number this gives,

$$\lim_{ka_s \ll 1} \sigma = 4\pi a_s^2. \tag{2.56}$$

In the opposite limit where the s-wave scattering length is large compared to the wave number this gives,

$$\lim_{ka_s \gg 1} \sigma = \frac{4\pi}{k^2}. \tag{2.57}$$

The value of the s-wave scattering length depends upon the magnetic field and has been calculated for the interaction between all of the ground states of ^{6}Li [75]. For the rest of this dissertation I will simply refer to the s-wave scattering length as $a = a_s$.

2.3.3 Fano-Feshbach resonance

The utilization of collisional, or Feshbach, resonances in fermionic atom traps is essential to the production Fermi superfluids. The high rate of collisions allows for an increased cooling rate, making it possible to reduce the temperature of the gas below the superfluid critical temperature.

When two atoms collide, the s-wave scattering length depends upon the molecular potential. ^{6}Li atoms can approach each other along a triplet or singlet potential. The distinction between these two types of interaction is that for a triplet potential the valence electrons of the atoms combine to form a triplet spin state where the total spin $S_{Total} = S_1 + S_2$ is equal to one, ($S_{Total} = 1$), and for a singlet potential the valence electrons combine to form a singlet state where the total electronic spin is zero ($S_{Total} = 0$). According to the energy eigenstate equations that we worked out, equation (2.34), in a magnetic field a pair of atoms in the two lowest states, $|1\rangle$

and $|2\rangle$, is approximately in a triplet state, $m_S = 1$. The spins are parallel and the energy of the combined state varies with magnetic field approximately as $-2\mu_e B$. Conversely, the spins for the singlet state will be antiparallel and have a negligible magnetic moment.

The triplet state is an open channel for interactions and the singlet state is a closed channel, which is energetically inaccessible at long range. A Feshbach resonance occurs when the continuum energy of the open channel is degenerate with the energy of a bound molecular state in the closed channel. We access a Feshbach resonance in our experiment by tuning the triplet energy such that it is degenerate with a bound molecular state in the singlet potential. There are several resonances between states $|1\rangle$ and $|2\rangle$. The two most relevant are a narrow resonance that occurs near 550G and a much broader resonance that occurs near 834 G. The resonant scattering length near 834G is approximately,

$$a = a_{bg}\left(1 - \frac{\Delta_B}{B - B_0}\right), \tag{2.58}$$

where a_{bg} = -1405 a_0 (a_0 is the Bohr radius), B_0 = 834.149 G, and Δ_B = 300 G [76]. A plot of the scattering length versus magnetic field across this resonance is shown in Figure 2.3.

The large width of the resonance provides a wide range of magnetic fields in which strong interactions may occur. Below the Feshbach resonance the scattering length is positive so the interactions will be repulsive. A bound molecular state exists, and below the resonance it is accessible. During a collision event with more than two atoms it is energetically possible for two of the atoms involved in the collision to form a molecule. The molecule, comprised of two fermions, will be a boson. A gas

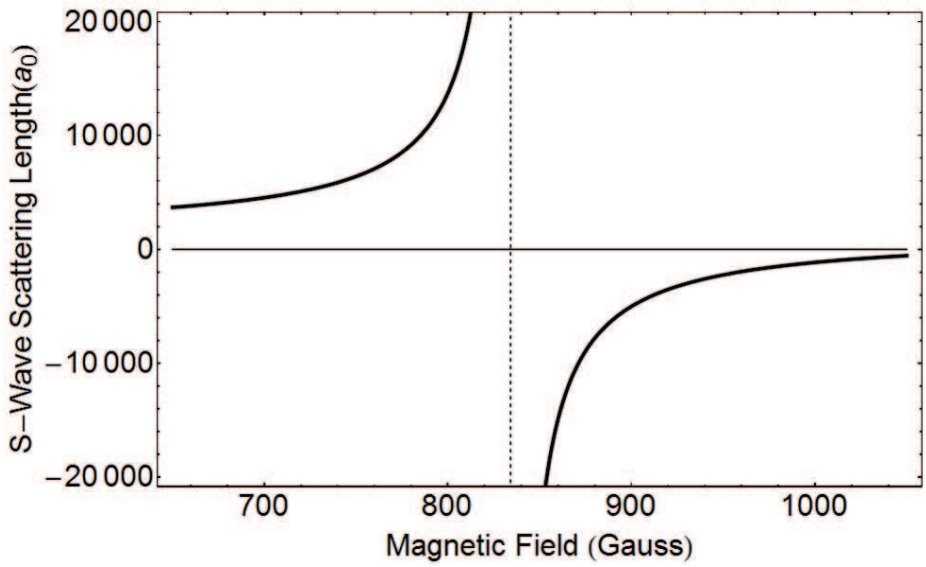

Figure 2.3: The s-wave scattering length a versus magnetic field across a broad Feshbach resonance at 834.149 Gauss. Below the resonance the scattering length is positive and the interactions are repulsive. Above the resonance the scattering length is negative and the interactions are attractive. The Feshbach Resonance is at 834 G. The inset shows the zero crossing at 528G

consisting entirely of bosonic molecules will form a Bose Einstein Condensate (BEC) at sufficiently low temperature. Above the resonance the scattering length is negative so the interactions will be attractive. At sufficiently cold temperatures the fermions interact much like cooper pairs according to Bardeen Cooper Schreifer (BCS) theory. Well below the resonance at 528G the scattering length is zero. In this case the gas is non interacting and behaves like an ideal Fermi system.

By tuning the magnetic field we can access four radically different types of gases, a BEC, a BCS system, a gas comprised of strongly interacting fermions, and an ideal Fermi system. It is because of this versatility that there is tremendous interest in studying cold Fermi gases in the presence of Feshbach resonances.

2.4 Zero temperature theory in the crossover region

In this section I will obtain the density profile and calculate the global chemical potential for the important limits near a Feshbach resonance. In Figure 2.3, there are regions where,

$$\begin{aligned} a_s \to 0^- &: \textit{Ideal Fermi Gas} \\ a_s \to \pm\infty &: \textit{Unitary Gas} \\ a_s \to 0^+ &: \textit{Bose Gas}. \end{aligned}$$

Using the main result of the local density approximation equation (2.29),

$$\mu_G = \mu_L(\mathbf{r}) + V_{ext}(\mathbf{r}). \tag{2.59}$$

the power law form of the equation of state equation (2.30),

$$\mu_L(\mathbf{r}) = \mathcal{C}n(\mathbf{r})^\gamma, \tag{2.60}$$

and an external harmonic oscillator trapping potential, $V_{ext}(\mathbf{r}) = V_{HO}(\mathbf{r})$ where,

$$V_{HO}(\mathbf{r}) = \frac{m\omega_x}{2}x^2 + \frac{m\omega_y}{2}y^2 + \frac{m\omega_z}{2}z^2, \tag{2.61}$$

we can solve for the density of the trapped gas, $n(\mathbf{r})$.

We can simplify our equations by assuming cylindrical symmetry where $\omega_\perp = \omega_x = \omega_y$ and $\rho = x^2 + y^2$. Further, we introduce natural radii $R_\perp$ and R_z such that $R_\perp^2 = \frac{2\mu_G}{m\omega_\perp^2}$ and $R_z^2 = \frac{2\mu_G}{m\omega_z^2}$. When we combine equations (2.59), (2.60), and (2.61) we find that the density of a harmonically trapped gas with a general equation of state is,

$$n(\rho, z) = \left(\frac{\mu_G}{\mathcal{C}}\right)^{1/\gamma}\left(1 - \frac{\rho^2}{R_\perp^2} - \frac{z^2}{R_z^2}\right)^{1/\gamma}. \tag{2.62}$$

When $a_s \to 0^-$ the atomic cloud is an ideal Fermi gas, where $\mathcal{C} = \hbar^2(3\pi^2)^{2/3}/2m$ and $\gamma = 2/3$. When we normalize to the total number of atoms by integrating the density (equation (2.62)) over all space where the density is not zero, $N = \int n(\mathbf{r})dV$. we can recover the above result for the global chemical potential of a zero temperature ideal gas trapped in a harmonic potential,

$$\mu_G = E_F, \tag{2.63}$$

where $E_F = \hbar\overline{\omega}(3N)^{1/3}$ is the ideal gas Fermi energy.

For a unitary Fermi gas, $a_s \to \pm\infty$. The s-wave scattering length diverges and

all length scales except for the interparticle spacing vanish at zero temperature. The characteristic length scale of a Fermi system is the inverse of Fermi wave vector,

$$k_F(\mathbf{r}) = (3\pi^2 n(\mathbf{r}))^{1/3}, \tag{2.64}$$

where $k_F(\mathbf{r})$ is a local quantity. When $|k_F a| \geq 1$, the scattering length is larger than the interparticle spacing, and the gas is strongly interacting. In the unitary limit the only length scale in the problem becomes the inverse of the Fermi wave vector, k_F. This is similar to the ideal Fermi gas case where k_F is the only relevant length due to the fact that the scattering length $a = 0$. At zero temperature this means that the local chemical potential in the unitary gas must still scale with density in the same way as it does in the ideal gas, (i.e. $\mu_L \propto n^{2/3}$). We can define a universal constant, β, such that the equation of state for a strongly interacting gas is,

$$\mu_L(\mathbf{r}) = (1+\beta)\frac{\hbar^2(3\pi^2)^{2/3}}{2m} n(\mathbf{r})^{2/3}. \tag{2.65}$$

Equation (2.65) is differs from the equation of state of an ideal Fermi gas only by a factor of $(1+\beta)$. We can therefore define an effective mass, $m* = m/(1+\beta)$ for the unitary gas atoms. As the geometric mean frequency $\overline{\omega} \propto \sqrt{1/m}$ and $E_F \propto \overline{\omega}$ we can then see that the global chemical potential will be,

$$\mu_G = (1+\beta)^{1/2} E_F \tag{2.66}$$

Therefore we can define the values $\mathcal{C} = (1+\beta)\hbar^2(3\pi^2)^{2/3}/2m$ and $\gamma = 2/3$ for the unitary gas equation of state. Again, we can integrate the density (equation (2.62)) over all space with the above strongly interacting values for our constants, $\mathcal{C}$ and

γ. It is easy to see that when we do this we will recover equation (2.66) for the global chemical potential of a zero temperature, strongly interacting gas trapped in a harmonic potential.

There are now many experiments that have measured β. In the sound velocity experiment, it was determined that [19],

$$\beta = -0.564(0.015). \tag{2.67}$$

which is consistent with recent quantum Monte Carlo calculations which put $\beta = -0.58$ [78], [30], [31], and $\beta = -0.56$ [61].

For the Bose limit $a_s \to 0^+$ and pairs of atoms in opposite spin states can fall into a molecular state. We can no longer use Fermi theory to describe the system, as the Pauli exclusion principle no longer applies. For a bosonic gas, we can define a mean-field interaction potential, which is equal to the local chemical potential. The mean-field interaction potential is [18].

$$\mu = \frac{4\pi\hbar^2 a_{mol}}{m_{mol}} n_{mol}, \tag{2.68}$$

where a_{mol} is the molecular-molecular scattering length, $m_{mol} = 2m$ is the molecular mass, and $n_{mol} = \frac{1}{2}n$ is the molecular density. The equation of state for a gas of Bose molecules in terms of atomic quantities is,

$$\mu_L(\mathbf{r}) = \frac{\pi\hbar^2 a_{mol}}{m} n(\mathbf{r}), \tag{2.69}$$

This means that for a Bose gas we can define $\mathcal{C} = \frac{\pi\hbar^2 a_m ol}{m}$, and $\gamma = 1$. If we use these values in the general from of the density we (equation (2.62)) we find,

$$n(\rho, z) = \frac{\mu_G}{\pi\hbar^2 \frac{a_{mol}}{m}} \left(1 - \frac{\rho^2}{R_\perp^2} - \frac{z^2}{R_z^2}\right) \tag{2.70}$$

In order to determine the global chemical potential we need to normalize to the total number of atoms,

$$N = \int n_0(\rho, z) d^2\rho \, dz. \tag{2.71}$$

We can express this integral as

$$N = 2\pi \int_0^{\rho_{max}} \int_{-z_{max}}^{z_{max}} \frac{\mu_G}{\pi\hbar^2 \frac{a_{mol}}{2m}} \left(1 - \frac{\rho^2}{R_\perp^2} - \frac{z^2}{R_z^2}\right) \rho \, dz \, d\rho \tag{2.72}$$

If we perform the variable substitution, $\rho' = \rho/R_\perp$ and $z' = z/R_z$ we get,

$$N = 2\pi R_\perp^2 R_z \frac{\mu_G}{\pi\hbar^2 \frac{a_{mol}}{2m}} \int_0^{\rho'_{max}} \int_{-z'_{max}}^{z'_{max}} \left(1 - \rho'^2 - z'^2\right) \rho' dz d\rho' \tag{2.73}$$

We want to integrate over all of space where the density not zero. Therefore we can determine our limits of integration from the equation, $(1 - \rho'^2 - z'^2) = 0$. If we are going to perform the z-integral first then the limits are,

$$z'_{max} = \sqrt{1 - \rho'^2} \tag{2.74}$$

$$\rho'_{max} = 1, \tag{2.75}$$

and the integral now becomes,

$$N = 2\pi R_\perp^2 R_z \frac{\mu_G}{\pi\hbar^2 \frac{a_{mol}}{2m}} \int_0^1 \int_{-\sqrt{1-\rho'^2}}^{\sqrt{1-\rho'^2}} \left(1 - \rho'^2 - z'^2\right) \rho' \, dz' \, d\rho'. \tag{2.76}$$

This integral can also be solved exactly:

$$\int_0^1 \int_{-\sqrt{1-\rho^2}}^{\sqrt{1-\rho^2}} \left(1-\rho^2-z^2\right) \rho \, dz \, d\rho = \frac{4}{15}. \tag{2.77}$$

Once we substitute in the appropriate values for $R_\perp$, and R_z, we find that the total number of atoms can be related to μ_G for a zero temperature Bose gas,

$$N = \frac{32\sqrt{2}}{15} \frac{\mu_G^{5/2}}{a_{mol}\hbar^2\sqrt{m}\,\omega_\perp^2\omega_z}. \tag{2.78}$$

After solving for μ_G we find that the global chemical potential depends upon experimental quantities N and $\overline{\omega}$ in addition to the molecule-molecule scattering length a_{mol}. If we relate μ_G for a BEC to the ideal gas value for E_F we find,

$$\mu_G = \frac{1}{4} E_F \left(5 a_{mol} \sqrt{\frac{E_F m}{2\hbar^2}}\right)^{2/5}. \tag{2.79}$$

To simplify the above equation we can define a global Fermi wave vector $E_F = \hbar^2 k_{F0}^2/2m$. When we make this substitution we find that for a zero temperature Bose gas confined in a harmonic potential the global chemical potential is,

$$\mu_G = \frac{1}{4} E_F \left(\frac{5}{2} k_{F0} a_{mol}\right)^{2/5}. \tag{2.80}$$

It is important to note that k_{F0} is a global quantity related to the global quantity $E_F = \hbar\overline{\omega}(3N)^{1/3}$.

In the above section we have determined thermodynamic quantities, μ_G and $n(\mathbf{r})$, in the three limits near the Feshbach resonance for a zero temperature gas trapped in a harmonic potential. In Chapter 3 we will use these quantities to calculate the

sound velocity for each limit.

Chapter 3

Hydrodynamic sound velocity

The ultimate goal of this chapter is to derive an equations for $c(0)/v_F$ in terms of thermodynamic values for an ideal gas, a unitary gas, and a weakly interacting BEC, where $c(0)$ is the sound velocity at the axial (z-direction) center of the trap and $v_F = \sqrt{2E_F/m}$ is the ideal gas Fermi velocity. The sound velocity can be determined from hydrodynamic theory. In Section 3.1, I will explore the time evolution of a density perturbation moving in a radially (x- and y- direction) trapped hydrodynamic gas. The hydrodynamic equations will be solved explicitly for sound velocity. The sound velocity will be determined in terms of two equilibrium quantities, the equilibrium density n_0 and the inverse of the derivative of the local chemical potential with respect the density $(\partial\mu_L/\partial n|_{n=n_0})^{-1}$. The effect of an axial (z-direction) confinement will be explored in Section 3.2. The dependence of sound velocity on position for harmonic axial confinement will be shown to be the same for all interaction strengths where the equation of state is in a power law form.

Furthermore, the local quantities $\mu_L(\mathbf{r})$ and $n(\mathbf{r})$, equation of state parameters $\mathcal{C}$ and γ and the global chemical potential μ_G derived in Section 2.4 for zero temperature theories in the limits of the crossover region, will be used to determine the sound velocity in the ideal Fermi gas, the unitary gas, and the weakly interacting BEC gas. Finally, I will introduce a simple model based upon mean field theory developed by

Cheng Chin, [28]. I will use this theory to predict the equation of state throughout the entire crossover region. Then, I will extend this model to calculate the sound velocity in a trapped gas.

3.1 Hydrodynamic sound velocity

Sound velocity can be defined as the speed at which a density perturbation will travel through a given medium. As such sound can be considered a moving perturbation in the density of our trapped gas. The dynamics of this movement is described by hydrodynamic equations, namely the continuity equation,

$$\partial_t n + \nabla \cdot (n\mathbf{v}) = 0 \tag{3.1}$$

and the Euler equation for irrotational flow where $\nabla \times \mathbf{v} = 0$,

$$m\partial_t \mathbf{v} + \nabla \left[\mu + V(\rho, z) + \frac{1}{2} m\mathbf{v}^2 \right] = 0. \tag{3.2}$$

The system in which sound velocity will be measured is a hydrodynamic gas trapped in a cigar shaped potential. The potential is strongly confining in two directions and weakly confining in one direction. Sound propagation will be modeled as a perturbation from the equilibrium condition. The total density is comprised of the equilibrium density, n_0, and a perturbation, Δn,

$$n = n_0 + \Delta n. \tag{3.3}$$

For the local chemical potential, one has similarly,

$$\mu_L = \mu_0 + \Delta\mu, \tag{3.4}$$

and for the stream velocity, since the equilibrium value $\mathbf{v_0} = 0$,

$$\mathbf{v} = \Delta\mathbf{v}. \tag{3.5}$$

In their paper on sound velocity, [58], Capuzzi et al. describe the dynamics of density fluctuations in a Quasi 1-Dimensional (Q1D) gas, that is a gas that is confined only in two directions by the potential,

$$V(\rho) = \frac{1}{2}m\omega_\perp^2\rho^2, \tag{3.6}$$

where, cylindrical symmetry dictates $x^2 + y^2 = \rho^2$, and the gas is infinitely long in the axial z-direction. At time t=0 a repulsive optical sheet potential is introduced at the center of the trapped gas and then removed. The repulsive potential causes a perturbation in the density. Hydrodynamics dictates that the perturbation will move axially outward in two directions away from the repulsive potential even after it has been removed. As stated above, the infinite axis of the trap (i.e. the direction of propagation) is defined as z-axis.

Thus, the equation for total density with a plane-wave perturbation propagating in the z-direction is,

$$n(\rho, z, t) = n_0(\rho) + \delta n(\rho)e^{i(\omega t - qz)}. \tag{3.7}$$

This then implies the form for the chemical potential, as at zero temperature the

chemical potential is a function only of density,

$$\mu_L(\rho, z, t) = \mu_0(\rho) + \frac{\partial \mu_L}{\partial n}|_{n=n_0} \delta n(\rho) e^{i(\omega t - qz)}. \tag{3.8}$$

And finally for plane wave propagation the stream velocity must have the form,

$$\mathbf{v}(z, t) = v_z e^{i(\omega t - qz)} \hat{z}. \tag{3.9}$$

Note that the stream velocity field $\mathbf{v}$ has no ρ dependance and only travels in the z-direction. This is a result of plane wave propagation. We will use the above equations in combination with the hydrodynamic equations of motion to solve for the velocity of a traveling plane wave, which is determined from the dispersion relation,

$$c = \frac{\omega}{q}. \tag{3.10}$$

First lets take a look at the continuity equation. Using equations (3.7) and (3.9) in equation (3.1) we obtain,

$$i\omega \delta n(\rho) e^{i(\omega t - qz)} - iq n_0(\rho) v_z e^{i(\omega t - qz)} - 2iq \delta n(\rho) v_z e^{2i(\omega t - qz)} = 0. \tag{3.11}$$

Note that n_0 is a zeroith order parameter and δn and v_z are first order parameters. Leaving out all terms higher than first order, the term $\delta_n(\rho) v_z$ is dropped as it is second order. The continuity equation becomes,

$$i\omega \delta n(\rho) = iq n_0(\rho) v_z. \tag{3.12}$$

Next, we will look at the Euler equation. Using equations (3.8) and (3.9) in

equation (3.2) we obtain,

$$\perp \;:\; \nabla_\perp \left(\mu_0 + \frac{\partial \mu_L}{\partial n}|_{n=n_0}\delta n(\rho)e^{i(\omega t - qz)}\right)\nabla_\perp V(r) = 0 \tag{3.13}$$

$$z \;:\; i\omega v_z e^{i(\omega t-qz)} - iq\frac{\partial \mu_L}{\partial n}|_{n=n_0}\delta n(\rho)e^{i(\omega t-qz)} - 2iqv_z^2 e^{2i(\omega t-qz)} = 0. \tag{3.14}$$

Applying the same restrictions as before and leaving out all terms of order higher than first, we find,

$$\perp \;:\; \nabla_\perp \left(\frac{\partial \mu_L}{\partial n}|_{n=n_0}\delta n(\rho)\right) = 0 \tag{3.15}$$

$$z \;:\; i\omega v_z - iq\frac{\partial \mu_L}{\partial n}|_{n=n_0}\delta n(\rho) = 0. \tag{3.16}$$

Consider the relevance of the $\perp$ direction part of the Euler equation. According to this $\frac{\partial \mu_L}{\partial n}\delta n(\rho) = \Delta\mu = \textit{Constant}$. This is a result of using a sheet beam, exciting a plane wave form for our perturbation. For a plane wave traveling in the z-direction the density perturbation varies radially in the trap, $\delta n(\rho)$. However, the energy of that perturbation, as expressed by chemical potential, does not vary radially. As the sheet beam excitation $\Delta\mu$ is constant. This means that the density perturbation will maintain its form as it propagates through the trap, leaving v_z without any ρ dependence. Also, we know from the equilibrium condition that $\partial_z\left[\mu_0(\rho,z) + V(\rho,z)\right] = 0$.

We can solve for v_z in equations (3.12) and (3.16). This gives,

$$\frac{\omega^2}{q^2}m\left(\frac{\partial \mu_L}{\partial n}|_{n=n_0}\delta n(\rho)\right)^{-1} = \frac{n_0(\rho)}{\delta n(\rho)}. \tag{3.17}$$

Substituting in the sound velocity $c^2 = \omega^2/q^2$ and simplifying gives us,

$$c^2 m \left(\frac{\partial \mu_L}{\partial n}|_{n=n_0} \right)^{-1} = n_0(\rho). \tag{3.18}$$

We integrate over the ρ dependence in equation (3.18), which yields

$$c = \left(\frac{1}{m} \frac{\int n_0 d^2\rho}{\int \left(\partial\mu/\partial n|_{n=n_0}\right)^{-1} d^2\rho} \right)^{1/2}. \tag{3.19}$$

Now that we have an equation for the speed of sound in terms of the density and the chemical potential it will be possible to solve for the ratio c_0/v_F. Once we add axial confinement, we can determine the sound velocity at the axial center (z=0) of the trap.

3.2 3-dimensional harmonic potential

The addition of a harmonic axial potential transforms the Q1D potential into a 3-dimensional harmonic potential. In our system, the axial confinement has contributions from magnetic and optical fields produced by electromagnetic coils and an a CO_2 laser, respectively. At high optical intensity, confinement is dominated by the optical field. However, at low CO_2 laser power, while radial confinement is still dominated by the optical field, the axial confinement is dominated by the magnetic field curvature. The magnetic field potential is harmonic. The combined optical and magnetic field potential has the form $V_z(z) = \frac{1}{2} m\omega_z^2 z^2$.

We will determine the values of our thermodynamic quantities using the main

result of the local density approximation equation (2.29),

$$\mu_G = \mu_L(\mathbf{r}) + V_{ext}(\mathbf{r}). \tag{3.20}$$

the power law form of the equation of state equation (2.30),

$$\mu_L(\mathbf{r}) = \mathcal{C} n(\mathbf{r})^{\gamma}, \tag{3.21}$$

and an external harmonic oscillator trapping potential, $V_{ext}(\mathbf{r}) = V_{HO}(\mathbf{r})$ where,

$$V_{HO}(\mathbf{r}) = \frac{m\omega_x}{2}x^2 + \frac{m\omega_y}{2}y^2 + \frac{m\omega_z}{2}z^2. \tag{3.22}$$

We can simplify our equations by assuming cylindrical symmetry where $\omega_\perp = \omega_x = \omega_y$ and $\rho = x^2 + y^2$. Further, we introduce natural radii $R_\perp$ and R_z such that $R_\perp^2 = \frac{2\mu_G}{m\omega_\perp^2}$ and $R_z^2 = \frac{2\mu_G}{m\omega_z^2}$. When we combine equations (3.20), (3.21), and (3.22) we find that the equilibrium density of a harmonically trapped gas with,

$$n_0(\rho, z) = \left(\frac{\mu_G}{\mathcal{C}}\right)^{1/\gamma} \left(1 - \frac{\rho^2}{R_\perp^2} - \frac{z^2}{R_z^2}\right)^{1/\gamma}. \tag{3.23}$$

In order to calculate the term $(\partial\mu_L/\partial n|_{n=n_0})^{-1}$, we must first know the relationship between the local chemical potential μ_L and the density n. From the power law equation of state (equation 3.21) $(\partial\mu_L/\partial n|_{n=n_0})^{-1}$ is

$$(\partial\mu_L/\partial n|_{n=n_0})^{-1} = (\gamma\mathcal{C})^{-1} n_0^{\frac{\gamma}{\gamma-1}}. \tag{3.24}$$

which in terms of spatial variable is,

$$\left(\frac{\partial \mu_L}{\partial n}|_{n=n_0}\right)^{-1} = \frac{1}{\gamma \mathcal{C}} \left(\frac{\mu_G}{\mathcal{C}}\right)^{-\frac{\gamma}{(\gamma-1)}} \left(1 - \frac{\rho^2}{R_\perp^2} - \frac{z^2}{R_z}\right)^{-\frac{\gamma}{(\gamma-1)}}. \tag{3.25}$$

Introducing a weak harmonic confinement along the z directions, $V_z(z) = m\omega_z^2 z^2/2$ creates a smooth and slow variation in the density along that direction. The power law relationship between the density and chemical potential still holds. Further, the radial derivative of a perturbation in density will be much greater than the derivative of the change in density in the z-direction. Therefore, we can consider the effect of the axial variation in density and chemical potential with respect to the hydrodynamic equations as negligible in comparison with the perturbation discussed in the previous section.

We would like to be able to determine the dependence of the sound velocity with respect to the axial (z-direction) coordinate, $c(z)$, in light of the addition of axial confinement. In equation (3.19) in order to determine the sound velocity we integrate only over the radial direction in both n_0 and $(\partial \mu_L/\partial n|_{n=n_0})^{-1}$. This leaves the a dependence on z. In order to obtain the z-dependent sound velocity we must evaluate the two integrals in equation (3.19),

$$c(z)^2 = \frac{1}{m} \frac{\int n_0 d^2\rho}{\int \left(\partial \mu/\partial n|_{n=n_0}\right)^{-1} d^2\rho}. \tag{3.26}$$

First, lets solve for the numerator in the 3-dimensional harmonic potential. The equilibrium density, equation (3.23), integrated over the radial direction is,

$$\int n_0 d^2\rho = 2\pi \int \left(\frac{\mu_G}{\mathcal{C}}\right)^{1/\gamma} \left(1 - \frac{\rho^2}{R_\perp^2} - \frac{z^2}{R_z^2}\right)^{1/\gamma} \rho \, d\rho. \tag{3.27}$$

Calculating the limit of the ρ integration is done by solving the equation $\left(1-\frac{\rho^2}{R_\perp^2}-\frac{z^2}{R_z^2}\right)=0$. The limits for ρ are,

$$\rho_{max} = R_\perp\sqrt{1-\frac{z^2}{R_z^2}} \tag{3.28}$$

$$\rho_{min} = 0. \tag{3.29}$$

We can replace our variables with dimensionless quantities, $\rho \to R_\perp\rho'$ and $z \to R_z z'$. Once we do this we find that the equation becomes

$$\int n_0 d^2\rho = 2\pi\left(\frac{\mu_G}{\mathcal{C}}\right)^{1/\gamma} R_\perp^2 \int_0^{\sqrt{1-z'^2}} \left(1-\rho'^2-z'^2\right)^{1/\gamma}\rho'\,d\rho'. \tag{3.30}$$

The integral can be solved as

$$\int_0^{\sqrt{1-z'^2}} \left(1-\rho'^2-z'^2\right)^{1/\gamma}\rho' d\rho' = \frac{\gamma}{2(1+\gamma)}\left(1-z'^2\right)^{1/\gamma+1}. \tag{3.31}$$

Therefore, in the general case for a power law equation of state the numerator in equation (3.19) is,

$$\int n_0 d^2\rho = 2\pi R_\perp^2\left(\frac{\mu_G}{\mathcal{C}}\right)^{1/\gamma}\frac{\gamma}{2(1+\gamma)}\left(1-z'^2\right)^{1/\gamma+1}. \tag{3.32}$$

Now lets do the same thing for the denominator in equation (3.19). Using equation (3.25) for the inverse of the derivative of the equilibrium local chemical with respect to density, $(\partial\mu_L/\partial n|_{n=n_0})^{-1}$, we obtain for the integral in the denominator of equation (3.19),

$$\int\left(\frac{\partial\mu_L}{\partial n}\right)^{-1} d^2\rho = 2\pi\int\frac{1}{\gamma\mathcal{C}}\left(\frac{\mu_G}{\mathcal{C}}\right)^{1/\gamma-1}\left(1-\frac{\rho^2}{R_\perp^2}-\frac{z^2}{R_z^2}\right)^{-(\gamma-1)/\gamma}\rho\,d\rho, \tag{3.33}$$

making the same replacement $\rho \to R_\perp \rho'$ and using the same limits of integration we find

$$\int \left(\frac{\partial \mu_L}{\partial n}\right)^{-1} d^2\rho = 2\pi R_\perp^2 \frac{1}{\gamma \mathcal{C}} \left(\frac{\mu_G}{\mathcal{C}}\right)^{-(\gamma-1)/\gamma} \int_0^{\sqrt{1-z'^2}} \left(1-\rho'^2-z'^2\right)^{1/\gamma-1} \rho'\, d\rho'. \quad (3.34)$$

The integral can be solved as,

$$\int_0^{\sqrt{1-z'^2}} \left(1-\rho'^2-z'^2\right)^{1/\gamma-1} \rho' d\rho' = \frac{\gamma}{2}\left(1-z'^2\right)^{1/\gamma}. \quad (3.35)$$

The denominator for equation (3.19) is then,

$$\int \left(\frac{\partial \mu_L}{\partial n}\right)^{-1} d^2\rho = 2\pi R_\perp^2 \frac{1}{\gamma \mathcal{C}} \left(\frac{\mu_G}{\mathcal{C}}\right)^{-(\gamma-1)/\gamma} \frac{\gamma}{2}\left(1-z'^2\right)^{1/\gamma}. \quad (3.36)$$

When we put equations, (3.32) and (3.36) together we find,

$$c(z)^2 = \gamma \mathcal{C} \frac{2\pi R_\perp^2 \left(\frac{\mu_G}{\mathcal{C}}\right)^{1/\gamma}}{2\pi R_\perp^2 \left(\frac{\mu_G}{\mathcal{C}}\right)^{-(\gamma-1)/\gamma}} \frac{2}{\gamma} \frac{\gamma}{2(1+\gamma)} \left(1-z'^2\right). \quad (3.37)$$

The above equation for the sound velocity can then be simplified greatly, producing the very nice and neat equation for z-dependent sound velocity,

$$c(z) = \sqrt{\frac{\gamma \mu_G}{m(1+\gamma)}} \left(1-z'^2\right)^{1/2}. \quad (3.38)$$

Using the hydrodynamic equations in addition to the most general thermodynamics of trapped gases we have produced a general sound velocity for any z-coordinate within the trap. Later we will use this equation to explore how the sound velocity varies within the trapped gas, and we will explore how the sound velocity varies as

we tune the interparticle interaction energy, which changes γ.

3.2.1 Position dependence of the sound velocity

In the beginning of this chapter we have assumed that a repulsive optical potential will generate a perturbation that travels axially outward from the point at which it is generated. Further we have calculated how the velocity of the perturbation will vary in the presence of a confining potential in the z-direction. Note that in equation (3.38) the z-dependant sound generally obeys $v_z(t) = c(0)[1 - z(t)^2/R_z^2]^{1/2}$. This means that as the sound wave approaches the edges of the cloud it will slow down. If we look at this equation in terms of position instead of velocity ($d\,z(t)/dt = v_z(t)$), we can set up a differential equation for the position, which looks like

$$\frac{d\,z(t)}{dt} = c(0)\left(1 - \frac{z(t)^2}{R_z^2}\right)^{1/2}. \tag{3.39}$$

We can then solve for $z(t)$. In our experiment we excite the sound pulse at the center of the trap. Therefore, assuming $z(0) = 0$ the position is,

$$z(t) = R_z \sin\left(\frac{c(0)t}{R_z}\right). \tag{3.40}$$

This, of course means that the velocity will be,

$$v_z(t) = c(0)\cos\left(\frac{c(0)t}{R_z}\right). \tag{3.41}$$

The position and velocity vary sinusoidally with time. At the center of the cloud the position dependence will be nearly linear in time, but as the sound wave nears the edges of the cloud we should see it slow down. This is an important feature of

the sound wave propagation, and one that we can use to check our theory. We should therefore use a sine wave to fit the position vs. time data. The details of this analysis is expanded upon in Chapter 7

3.2.2 Sound Velocity in the limits near a Feshbach resonance

In the previous section we included the effect of the harmonic potential in the equation for sound velocity. In this section I will calculate the sound velocity in the ideal gas, unitary, and BEC limits. We are only interested in the sound velocity along the axial center of the trap. Therefore, at z = 0 the general equation for sound velocity, equation (3.38), is,

$$c(0) = \sqrt{\frac{\gamma \mu_G}{m(1+\gamma)}}. \tag{3.42}$$

So far, all the equations used have been completely general for a gas trapped in a 3-dimensional harmonic potential with hydrodynamic properties. In order to obtain the ratio $c(0)/v_F$ for specific gases we will need the thermodynamic parameters γ and μ_G, the global chemical potential, that were found in Chapter 2 in each limit of the crossover region. Note that in Chapter 2 we expressed μ_G in terms of the ideal gas fermi Energy, E_F. In our experiment we measure the sound velocity in distance over time (i.e. velocity) units. The ideal gas Fermi velocity v_F defined from $E_F = \frac{1}{2}mv_F^2$ is the characteristic velocity.

We found that in the far BCS limit, the gas approaches an ideal Fermi system. It is important to point out that an Ideal Fermi system will not be hydrodynamic. However, the sound velocity should approach the ideal gas limit as we tune the interactions further towards the BCS limit. This will remain true for as long as the gas exhibits hydrodynamic properties. Once the gas is no longer hydrodynamic

we will no longer be able to observe the sound perturbation.

In accordance with equation (3.19) we have calculated the two integrals pertaining to the numerator and denominator of that equation for a general case. Further, we have calculated $\mu_G = E_F = \frac{1}{2}mv_F^2$ for the ideal Fermi gas, equation (2.63), and found that the equation of state for a unitary gas gives $\gamma = 2/3$. When we use equation (2.63) and the value of $\gamma = 2/3$ in equation (3.42) we find

$$c(0) = \sqrt{\frac{\frac{2}{3}\frac{1}{2}mv_F^2}{m(1+\frac{2}{3})}}, \tag{3.43}$$

which reduces to

$$c(0) = \frac{v_F}{\sqrt{5}}. \tag{3.44}$$

For a gas in the unitary limit, γ is still 2/3, and the value for $\mu_G = \sqrt{1+\beta}E_F = \sqrt{1+\beta}\frac{1}{2}mv_F^2$, from equation (2.66). When we use these values for μ_G and γ in equation (3.42) the sound velocity in a unitary gas at the axial center of the trap is

$$c(0) = \sqrt{\frac{\frac{2}{3}(1+\beta)^{1/2}\frac{1}{2}mv_F^2}{m(1+\frac{2}{3})}}, \tag{3.45}$$

which reduces to

$$c(0) = \frac{(1+\beta)^{1/4}v_F}{\sqrt{5}}. \tag{3.46}$$

We will use a similar method to calculate the sound velocity for a BEC. The value of the zero temperature global chemical potential in a Bose gas from equation (2.80) is $\mu_G = \frac{1}{8}mv_F^2\left(\frac{5}{2}k_{F0}a_{mol}\right)^{2/5}$ and the equation of state for a Bose gas gives $\gamma = 1$.

When we use equation (2.80) and the value of $\gamma = 2/3$ in equation (3.42) we find,

$$c(0) = \frac{1}{4}\left(\frac{5}{2}a_{mol}k_{F0}\right)^{1/5} v_F \tag{3.47}$$

These are the three equations for the sound velocity in units of the ideal gas Fermi velocity in the limits of the ideal gas, unitary gas, and weakly interacting BEC. In the next section we will use a simple mean field model in order to explore how the velocity might vary between these limits.

3.3 Mean field model for ultra cold gases

The general power law equation of state, equation (2.30) that can be used for both Bose and Fermi gases is,

$$\mu_L(\mathbf{r}) = \mathcal{C}n(\mathbf{r})^{\gamma}, \tag{3.48}$$

In this section I will examine a simple mean field model developed by Cheng Chin [28] to determine the equation of state of a constant density gas in the BEC-BCS crossover. Then, I will extend the theory to determine the sound velocity in a trapped gas.

The variation of the sound velocity in crossover region can be understood by examining the interparticle interactions. To begin with, consider the one dimensional scattering problem of a particle close to zero energy incident on the attractive square well potential.

Let the square well potential extend a distance R from the origin, at a depth of $|V_0| \gg$ the kinetic energy of the particle. This represents the interaction between two particles, the incident particle and the scatterer. The Schrödinger equation for this

situation would be,

$$\left[\frac{\hbar}{2M}\partial_r^2 + V(r)\right]\psi(r) = E_B\psi(r), \tag{3.49}$$

where $\psi(r)$ is the pair wave function, E_B is the binding energy between the two particles and M is the reduced mass. For the case of Fermi atoms pairing to form Boson molecules the reduced mass $M = \frac{1}{2}m$, where m is the mass of the Fermi atoms. For $r < R$ the pair wave function can be solved, $\psi(r) = A\sin(k_0 r)$, where k_0 is the relative wave vector between particles. When $V_0 \ll E_B$, $k_0 = \sqrt{\frac{m}{\hbar^2}V_0}$. For $r > R$ the solution for the pair wave function is $\psi(r) = B\exp(-\kappa r)$, where $\kappa = \sqrt{\frac{m}{\hbar^2}E_B}$. The boundary conditions for $\psi(R)$ and the derivative of the pair wave function with respect to r, $\partial_r\psi(r)|_{r=R}$ are,

$$\psi(R) = A\sin(k_0 R) = B\exp(-\kappa R) \tag{3.50}$$

$$\partial_r\psi(R) = Ak_0\cos(k_0 R) = -B\kappa\exp(-\kappa R). \tag{3.51}$$

If we take the ratio of the boundary conditions of the pair wave function and its first derivative we find

$$\frac{\psi(R)}{\partial_r\psi(R)} = \frac{1}{k_0}\tan(k_0 R) = -\frac{1}{\kappa}. \tag{3.52}$$

We recognize the term, $-\frac{1}{k_0}\tan(k_0 R)$, as the s-wave scattering length, a. which means $\kappa = 1/a$. In the limit where R tends towards zero this means that the normalized pair wave function is,

$$\psi_0(r) = \sqrt{\frac{2}{a}}\exp(-r/a) \tag{3.53}$$

and the boundary condition at $r = 0$ is,

$$\psi_0(0) = a\partial_r\psi_0(0)|_{r=0}. \tag{3.54}$$

Further, when we use this wave function in Schrödinger's equation (3.49), we find that the binding energy is, $E_B = \hbar^2/(ma^2)$.

3.3.1 A simple mean field model of μ_L in the BEC-BCS crossover

So far we've only considered the wave function for two particles. If we expand our view to a gas of atoms that interact according to this potential picture, ψ_0 can be considered as the wave function for internal relative atomic motion. Then, in terms of a gas of atoms, the total wave function would be $\Psi(\mathbf{R})\psi_0(r)$, where $\Psi(\mathbf{R})$ is the wave function for the center of mass motion of an atom relative to $\mathbf{R}$, its position. The interaction term $\psi_0(r)$ is then dependant on the relative position of the two atoms, r. The mean field equation for a system of particles is,

$$\left[-\frac{\hbar^2\nabla^2}{4m} - \frac{\hbar^2\partial_r^2}{2M} + \hat{U}\right]\Psi(\mathbf{R})\psi_0(r) = \mu\Psi(\mathbf{R})\psi_0(r), \tag{3.55}$$

where μ is the chemical potential for two atoms, $\hat{U} = g|\Psi(\mathbf{R})|^2$ is the mean field interaction and g is the interaction term. For a uniform gas at constant density $|\Psi(\mathbf{R})|^2 = n$ and $\nabla^2|\Psi(\mathbf{R})|^2 \to 0$. The mean field equation for a uniform gas at constant density is,

$$\left[-\frac{\hbar^2\partial_r^2}{m} + g(r)n\right]\psi_0(r) = \mu\psi_0(r). \tag{3.56}$$

If we consider the gas to be made up of pairs of atoms forming bosons, the expectation value for g should yield the molecular mean field shift,

$$\int_0^\infty \psi_0^* n g(r)\psi_0 dr = \frac{4\pi a_m n}{2m} \tag{3.57}$$

where a_m is the molecule-molecule scattering length. Using equation (3.53) for the

wave function ψ_0 we find that

$$g(r) = c_{BEC}\frac{\hbar^2}{m}r, \tag{3.58}$$

where.

$$c_{BEC} = 4\pi a_m/a. \tag{3.59}$$

Recent four body calculations have determined that $a_m = 0.6a$ [29]. This form of $\psi_0(r)$ and the equation for $g(r)$ is valid in the BEC limit. A pair wave function that is valid for the mean field equation (3.56) is,

$$\psi(r) = NAi[c_{BEC}^{1/3}n^{1/3}r - 2c_{BEC}^{-2/3}\mu/E_0], \tag{3.60}$$

where N is a normalization factor, Ai is the Airy special function that has the property that its second derivative $Ai''(x) = xAi(x)$, and $E_0 = \hbar^2 n^{2/3}/m$. Further, equation (3.54) the boundary condition, $\psi(0) = -a\partial_r\psi(r)|_{r=0}$ still holds.

Quickly, I will show that equation (3.60) satisfies the mean field equation (3.56). Take an Airy function dependant on r in the form $Ai[Ar + x]$. Remembering the properties of the Airy function we take the second derivative of this function in terms of r and find,

$$\partial_r^2 Ai[f(r) + x] = A^2(Ar - x)Ai[f(r) + x]. \tag{3.61}$$

For $\psi(r)$, $A = c_{BEC}^{1/3}n^{1/3}$ and $x = 2c_{BEC}^{-2/3}\mu/E_0$. When we use these terms in equation (3.61) we find,

$$\partial_r^2\psi(r) = \frac{m}{\hbar}(\mu - g(r)n)\psi(r), \tag{3.62}$$

which is equivalent to the mean field equation (3.56).

Next, as a second check of the model, I will show that $\psi(r) = NAi[c_{BEC}^{1/3} n^{1/3} r - 2c_{BEC}^{-2/3}\mu/E_0]$ (equation (3.60)) exactly reproduces $\psi_0(r) = \sqrt{\frac{2}{a}}\exp(-r/a)$ (equation (3.53)) in the dilute BEC limit for small scattering lengths where $a \to 0^+$, $2\mu \to E_B = \hbar^2/(ma^2)$, and $n^{1/3}r \ll 1$. In order to do this we must take the Taylor series expansion of $\psi(r)$ with respect to the small parameter $n^{1/3}r \to 0$. The first three terms of this series are,

$$\psi(r) = \psi(0) + \frac{1}{2}c_{BEC}^{1/3} n^{1/3} r\psi'(0) + \frac{1}{6}(c_{BEC}^{1/3} n^{1/3} r)^2(-c^{-2/3}\frac{\mu}{E_0})\psi(0) + (O)(n^{1/3}r)^2. \tag{3.63}$$

Using the boundary condition, $\psi(0) = -a\psi'(0)$, and the fact that $n^{2/3}E_B/E_0 = 1/a^2$ we find

$$\psi(r) = \psi(0) + \frac{r}{2a}\psi(0) + \frac{r^2}{6a}\psi(0) + (O)(n^{1/3}r)^2, \tag{3.64}$$

which is simply the series expansion of $\psi_0(r) \propto \exp(-r/a)$.

Right now $\psi(r)$ represents the pair wave function in the BEC limit. In order to find the pair wave function in the BCS limit we need a way to determine the mean field interaction from the properties of a Fermi gas. On the far BCS side as $na^3 \to 0^-$ the system approaches an ideal Fermi gas. The chemical potential for an ideal fermi gas at zero temperature is,

$$\lim_{na^3 \to 0^-} \frac{\mu}{2} = \epsilon_F = \frac{(3\pi^2 n)^{2/3}\hbar^2}{2m} \tag{3.65}$$

where ϵ_F is the density dependent Fermi energy and μ is the chemical potential of two atoms. We would like so solve for the pair wave function $\psi_0(r) = \sqrt{\frac{2}{a}}\exp(-r/a)$ (equation (3.53)) in the BCS limit. The boundary condition $\psi_0(0) = a\partial_r\psi_0(r)|_{r=0}$

(equation (3.54)) in the BCS limit is,

$$\lim_{na^3 \to 0^-} \partial_r \psi(0) = 0. \tag{3.66}$$

If we use the same form for the interaction term $g = c_{BCS}\frac{\hbar^2}{m}r$ and corresponding pair wave function $\psi(r) = NAi[c_{BCS}^{1/3} n^{1/3} r - 2c_{BCS}^{-2/3}\mu/E_0]$,we can solve for c_{BCS} in the BCS limit,

$$\lim_{na^3 \to 0^-} \partial_r \psi(0) \propto Ai'[2c_{BCS}^{-2/3}\mu/E_0] = 0. \tag{3.67}$$

Therefore $-2c_{BCS}^{2/3}\mu/E_0 = -\alpha$, where $\alpha \approx 2.338$ is the first zero of the Airy Function. This gives,

$$c_{BCS} = 3\pi^2 \alpha^{-3/2}. \tag{3.68}$$

The Fermi wave number is $k_F = (3\pi^2 n)^{1/3}$. We can now put the pair wave function and the boundary condition in a form valid in the BCS limit in terms of Fermi variables, k_F and ϵ_F.

$$\psi(r) = NAi[\alpha^{-1/2} k_F r - \alpha\frac{\mu}{\epsilon_F}] \tag{3.69}$$

The pair wave functions, equations (3.60) and (3.69) can be used to find the chemical potential for a particular value of $1/(k_F a)$. For example if we take the bounder condition, equation (3.54), $\psi_0(0) = a\partial_r \psi_0(r)|_{r=0}$ and apply it to the pair wave function in the BCS limit, equation (3.69) we find,

$$\frac{k_F a}{\alpha} = -\frac{Ai[-\alpha\mu/\epsilon_F]}{Ai'[-\alpha\mu/\epsilon_F]}. \tag{3.70}$$

Then, we can use mathematical software like Mathematica to numerically solve for the chemical potential. Figure 3.1 shows the result of this process for both the BEC

and BCS pair wave functions. The Mathematica code used to generate these curves and others in this section can be found in Appendix C.

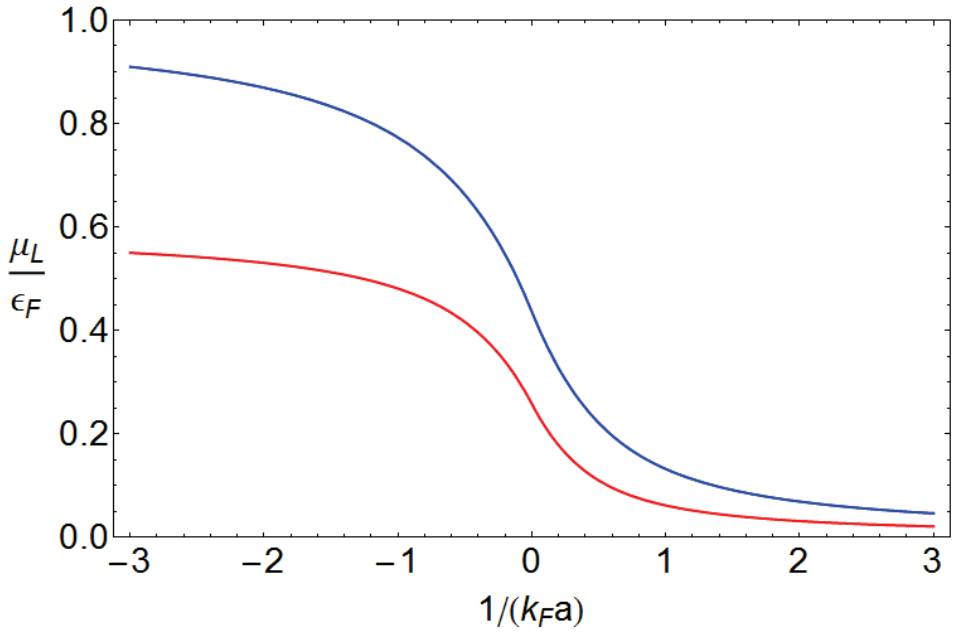

Figure 3.1: The simple mean field model provides a prediction of the local chemical potential in units of local Fermi energy (μ_L/ϵ_F) for a gas of uniform density (n) versus $1/(k_F a)$. The chemical potential was determined using a simple mean field model in the BCS limit (Blue) and the BEC limit (Red). For large negative values of $1/(k_F a)$ the chemical potential in the BCS limit is one. For large positive values of $1/(k_F a)$ the chemical potential in the BEC limit approaches the binding energy local chemical potential approaches zero.

The chemical potential, μ determined in the BCS approaches one for large negative values of $1/k_F a$. This is as it should be as μ for an ideal Fermi gas at zero temperature is equal to the Fermi energy. μ determined in both the BCS limit and the BEC limit approaches the binding energy for large positive values of $1/k_F a$. However, they to not approach the binding energy in the same manor. The difference between μ and E_b is smaller for the simple mean field model determined of μ in BEC limit. This distinction will become relevant when we extend the model to prediction the sound

velocity of a trapped gas.

One last limit needs to be explored. Using equation (3.70) we can determine the chemical potential on resonance where the scattering length diverges, $\alpha \to \pm\infty$. In this limit we find that the chemical potential can be determined from,

$$Ai'[-\alpha\mu/\epsilon_F] = 0, \tag{3.71}$$

or $-\alpha\mu/\epsilon_F = \alpha'$, where $\alpha' = 1.019$ is the fist zero of $Ai'[x]$. As discussed previously the relationship between the chemical potential of a unitary gas and the fermi energy of an ideal gas should go as

$$\frac{\mu}{2} = (1+\beta)\epsilon_F, \tag{3.72}$$

where again μ is the chemical potential for two atoms. This means that the simple mean field model provides, $\beta = -0.564$. This is exactly the value we get for β in the sound velocity experiment, equation (2.67.)

The simple mean field model can be used to provide insight into the equation of state over the entire crossover region. μ_{BCS} provides reasonable values for the chemical potential in the BCS, BEC and unitary limit.

Part of the chemical potential will be used in the formation of molecules, therefore total local chemical potential for a single atom is in fact,

$$\mu_L = 2\left(\frac{\mu}{2} + E_b\right) \tag{3.73}$$

We can determine the full equation of state in the crossover region, $\mu_L \propto n^\gamma$, from the equation,

$$\gamma = \frac{\partial \ln \mu_L}{\partial \ln n}. \tag{3.74}$$

Using the result for the chemical potential in the BCS limit, μ_{BCS}, this gives,

$$\gamma = \frac{2}{3}\left(1 + \frac{E_b}{\mu_{BCS}}\right)^{-1}\left(1 + 1/2\frac{\alpha^{-3/2}k_F a\epsilon_F^2/\mu_{BCS}^2}{k_F^2 a^2 + \epsilon_F/\mu_{BCS}}\right). \tag{3.75}$$

We have only calculated γ for the chemical potential determined in the BCS limit, see Figure 3.2.

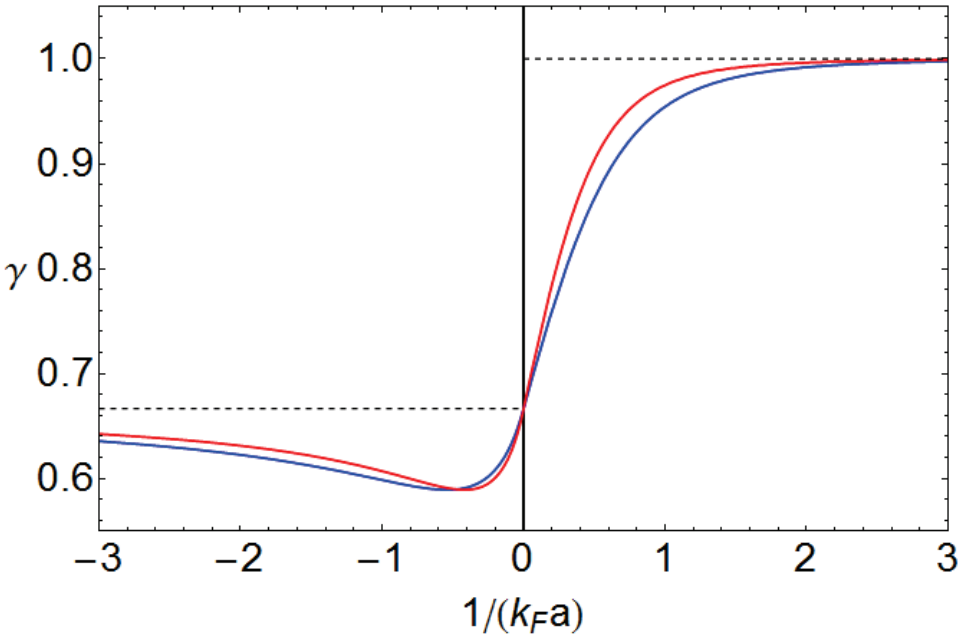

Figure 3.2: γ versus $1/k_F a$ as determined by the simple mean field model in the BCS limit(Blue) and the BEC limit (Red). The dashed lines are $\gamma = 1$ for positive values of $1/(k_F a)$ and $\gamma = 2/3$ for negative values of $1/(k_F a)$.

The γ calculated with the mean field model gives $\gamma = 2/3$ in the unitary ($1/(k_F a) = 0$) and ideal gas ($1/(k_F a) \to -\infty$) limit, and $\gamma = 1$ in the weakly interacting BEC ($1/(k_F a) \to +\infty$) limit.

3.3.2 A simple mean field model of c(0) in a harmonic trap

From the simple mean field model we are able to determine the local chemical potential μ_L as a function of a local $1/k_F a$,

$$\frac{\mu_L}{\epsilon_F} = f\left[\frac{1}{k_F a}\right], \tag{3.76}$$

as shown in Figure 3.1. However, as this model is for a uniform gas we must find a way to adjust the model so that it represents atoms confined in a trap. Further, in our experiments we normally express our measurements in terms of ideal Fermi gas values in an equivalent trap. Right now the chemical potential is expressed in terms of units of $\epsilon_F(n)$ and plotted against $1/(k_F(n)a)$, both of which are quantities that depend on the local density.

In order to determine the effect of density and normalize our chemical potential in the usual way we introduce $E_F = (3\pi^2 n_{0I})^{2/3}\hbar^2/2m$ and $\hbar^2 k_{F0}^2/2m = E_F$, where $E_F = \hbar\overline{\omega}(3N)^{1/3}$ is the Fermi energy of a trapped ideal gas, n_{0I} is the ideal gas density at the center of the trap, and k_{F0} is the ideal Fermi wave number. We can then rewrite the above equation as

$$\frac{\mu_L}{E_F} = \left(\frac{n}{n_{0I}}\right)^{2/3} f\left[\frac{1}{k_{F0}a}\left(\frac{n}{n_{0I}}\right)^{-1/3}\right]. \tag{3.77}$$

Once this is done, it is easy to invert this equation such that we have a density as a function of chemical potential at a particular value of $1/(k_{F0}a)$,

$$\frac{n}{n_{0I}} = F\left[\frac{\mu_L}{E_F}\right] \tag{3.78}$$

According to the local density approximation the global chemical potential μ_G and

the trapping potential $V(r) = V_0(1 - \exp(-\frac{m\bar{\omega}^2}{2V_0}r^2))$ can be expressed in terms of the local chemical potential, $\mu_L = \mu_G - V(r)$. In the limit of large V_0 the potential takes the form of a harmonic oscillator, $V(r) = \frac{m\bar{\omega}^2}{2}r^2$. Then, the spatial variation of density is,

$$\frac{n}{n_{0I}} = F\left(\frac{\mu_G}{E_F} - \frac{m\bar{\omega}^2}{2E_F}r^2\right). \tag{3.79}$$

In order to determine the global chemical potential we must normalize to the total number of atoms N,

$$N = n_{0I}\, 4\pi \int_0^{r_{max}} F\left(\frac{\mu_G}{E_F} - \frac{r^2}{\sigma^2}\right) r^2 dr, \tag{3.80}$$

where $\sigma = \sqrt{\frac{2E_F}{m\bar{\omega}^2}}$. In terms of dimensionless variables $\mu'_G = \mu_G/E_F$ and $\rho = r/\sigma$ this integral becomes,

$$N = n_{0I}\, \sigma^3 4\pi \int_0^{\sqrt{\mu'_G}} F\left(\mu'_G - \rho^2\right) \rho^2 d\rho, \tag{3.81}$$

where the limit of integration $r_{max} = \sqrt{\mu'_G}$ arises from the fact that the density goes to zero when the local chemical potential is zero. The above integral can be further simplified when we realize,

$$\frac{n_{0I}\sigma^3}{N} = \frac{1}{3\pi^2}\left(\frac{E_F 2m}{\hbar}^2\right)^{3/2}\left(\frac{2E_F}{m\bar{\omega}^2}\right)^{3/2} = \frac{8}{\pi^2} \tag{3.82}$$

We can then solve for the global chemical potential in units of the ideal fermi energy from the equation,

$$1 = \frac{32}{\pi}\int_0^{\sqrt{\mu'_G}} F\left(\mu'_G - \rho^2\right) \rho^2 d\rho. \tag{3.83}$$

Solving the above integral yields the global chemical potential μ'_G as a function of

$1/(k_{F0}a)$. In addition, the functions,

$$n' = F\left(\mu'_G - \rho^2\right) \tag{3.84}$$

$$\mu'_L = n'^{2/3} f\left(\frac{1}{k_{F0}a} n'^{-1/3}\right), \tag{3.85}$$

relate the density and chemical potential to spatial variables. In the above equations, $\mu'_L = \mu_L/E_F$ and $n' = n/n_{0I}$.

We can now relate the above quantities to the sound velocity. Factors of n_{0I} in the numerator and the denominator cancel and E_F is embedded in μ'_L. When we calculate the sound velocity as a function of the Fermi velocity a factor of 1/2 appears under the square root. The equation for the sound velocity, equation (3.19) in terms of the parameters derived from the simple mean field model is then,

$$\frac{c}{v_F} = \sqrt{\frac{1}{2} \frac{\int n' \rho d\rho}{\int \left(\frac{\partial \mu'_L}{\partial n'}\right)^{-1} \rho d\rho}}. \tag{3.86}$$

We now have all the equations needed to calculate the sound velocity in the BEC-BCS crossover. The sound velocity in units of the Fermi velocity as determined by the mean field model presented in this section is shown in Figure 3.3.

Regardless of whether we use c_{BEC} or c_{BCS} as our dimensionless parameter, the simple mean field model provides a prediction of the sound velocity through the entire crossover region. However, the theory will only be valid for one curve at a time. Therefore, this model does not provide a continuous prediction of the sound velocity. Instead, the simple mean field model provides two curves determined in the BEC and BCS limits that should be valid only on the BEC or BCS side of resonance $(1/(k_{F0}a = 0)$ respectively. However, The BCS curve agrees well with our data on

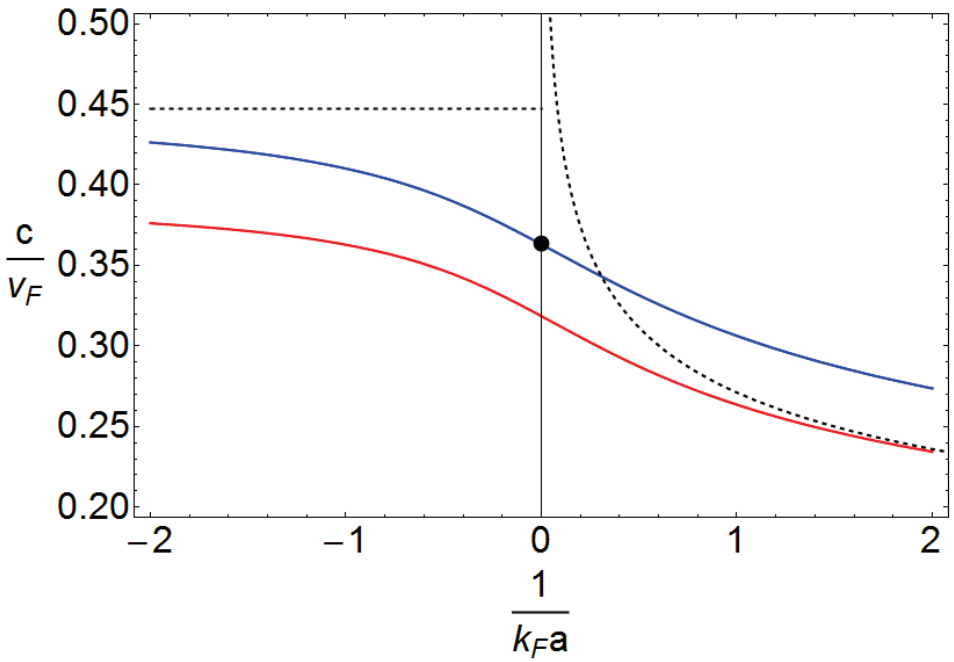

Figure 3.3: The sound velocity in units of the Fermi velocity (c/v_F) as determined by the mean field model plotted versus $1/(k_{F0}a)$. Using the dimensionless variable c_{BCS} in the model produces a sound velocity that is valid for large negative values of $1/(k_{F0}a)$ (Blue Line). Dashed lines show zero temperature theoretical curves in the BEC and BCS limits.

resonance. In Chapter 7 we will compare this model to the sound data taken in the BEC-BCS crossover. However, as seen in Figure 3.3, the model approaches the BEC theoretical curve for large positive values of $1/k_{F0}a$ when we use c_{BEC}. When we use c_{BCS} the model replicates the sound velocity for an ideal Fermi gas for large negative values of $1/k_{F0a}$ and produces a reasonable value for the dimensionless parameter $\beta = -0.564$ in the unitary limit.

Chapter 4

Trapping and cooling

The basic experimental system we use in the atom trapping and cooling lab has not changed for the past decade. Descriptions of the experimental apparatus and procedures can be found in previous dissertations produced by former members of the quantum optics group at Duke [62–67]. However, it important to place the sound velocity experiment in a broader framework. In this chapter I will provide an overview of the basic cooling and trapping techniques used in our experiment.

Most of the experimental system used in sound velocity experiment was up and running when I started working on the sound velocity experiment. However, in order to run the experiment an understanding of each individual component in necessary. Atom trapping and cooling experiments are often times very complex and have many different components. A concerted effort was taken to create the simplest experiment possible, and in relation to other atom trapping experiments this goal was achieved.

The system is still very complicated and contains many different components. As a working rule in the lab, each individual component works 95 % of the time, which means that when your working with 100 different components your only running 0.5 % of the time. In reality, the situation is not that dire. However, good working knowledge of the basic apparatus is necessary, especially when trouble shooting the system.

The experimental apparatus contains a locking region and a main system. Each of these is comprised of a vacuum system and an atom source or oven. In addition the main system makes use of various magnetic field generation subsystems. There are three independent laser beam sources and their associated beam conditioning components. A Coherent 899 Dye laser generates the laser beams with a wavelength of 671 nm, used in the MOT, Slower, and Camera systems. The photon source of the dye laser is the florescence of a liquid dye excited by an external pump laser. The dye used is LD688 dye dissolved in 2-phenoxyethanol. The external pump laser is a Coherent Verdi V-10 diode pumped solid state laser. The light from the Verdi is used in our sound velocity experiment. We generate the light used for the dipole trap with a Coherent CO_2 laser. We condition the laser beams using acusto-optic modulators (AOs).

In this section I will try to follow, as much as possible, the general sequence of events an atom goes through during the course of an experiment. I will not cover the construction of the vacuum and magnet systems other than to say here that the vacuum system, which is maintained by Ion pumps and sublimation pumps, produces an Ultra High Vacuum (UHV) environment that reaches the limit of our Ion gauge at 2×10^{-11} Torr. The magnets are two electro magnetic coils operated in either a Helmholtz (parallel) or anti-Helmholtz (opposing) current configurations.

During the experiment, solid ^{6}Li is melted and then boiled off in an oven. One oven expels atoms into our main vacuum system. Next, the atoms enter our Zeeman slower, where they are (as the name implies) slowed down. Once the atoms exit the slower they are trapped and cooled in a Magneto Optical Trap (MOT) down to a temperature of approximately 150 μK. The atoms are then loaded into an optical dipole trap, the physics of which was discussed in Section 2.1. The atoms are further cooled by

lowering the intensity of the dipole trap laser to a temperature of approximately 10 nK. Then, the magnets are used to select the various interaction strengths available across a broad Feshbach resonance (Section 2.3) centered at 834 G. Once the atoms are conditioned properly we perform our experiment. Data is extracted from the experiment in the form of two dimensional pictures taken via absorption imaging.

4.1 The oven

We work with a ultra cold gas consisting of ^{6}Li atoms. This begs the question, where do the atoms come from. The atoms in our experiment start in solid form. They are placed in an oven, which looks like a corn cob pipe (See Figure 4.1). The pipe is attached to the system such that the atoms, inserted into the bowl of the pipe in solid form are injected into the experiment via the stem. The oven is heated to the point where the atoms first liquify and then boil. Further, a mesh covers in internal surfaces of the oven in order to recirculate the off-axis, gaseous ^{6}Li atoms that hit the sides either the bowl or stem of the oven.

The oven is wound with nickel-chromium wire. The windings can be divided into 5 distinct regions. A power supply generates about 20 Amps which is sent into a current divider in order to supply each of these regions independently. In order to achieve good flux through the stem of the pipe as well as recirculation through the mesh, we must apply heat to the oven carefully. The temperature profile used in the main experiment is summarized in Table 4.1.

The temperature profile indicated in the above table is to be considered approximate. Region 3 is considered the source of the atoms. Regions 1 and 2 are kept above the boiling point of ^{6}Li to supply Region 3, and Regions 4 and 5 are kept at

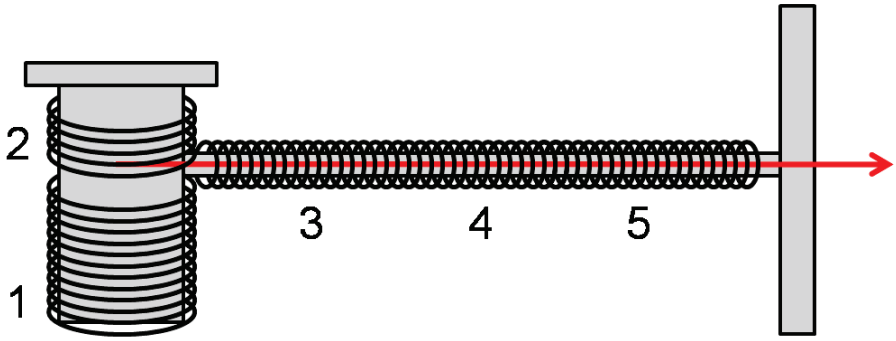

Figure 4.1: Our ovens look like a corn cob pipe. Nickel-chromium wire, wrapped around five distinct regions of the oven, is used to heat the entire assembly.

Region	Temperature (C)
1	320
2	340
3	410
4	310
5	240

Table 4.1: Temperature profile for a typical oven

temperatures lower than region 3. This causes atoms with off axis velocity that hit the mesh covering the inner surface of the oven to "wick" back to the source region. The oven attached to the locking region vacuum system is of similar design.

4.2 Locking region

The dye laser is able to produce a wide range of frequencies. In order to select the appropriate frequency for the trapping of ^{6}Li we must reference the laser beam frequency to the atomic resonance. We use the atomic resonance of atoms produced in the locking region oven for our reference frequency, and control electronics provide feed back loop to lock the frequency of our laser. The locking region consists of an oven and a vacuum tee with three window ports. The oven creates an atomic beam which is intersected by a beam from the dye laser (See Figure 4.2). The intersection is orthogonal, so there will be no overall Doppler shift due to off axis velocity. However, we do see evidence of Doppler broadening of the atomic peak. Through the third window port a photo-multiplier tube senses light from scatter on the atomic resonance.

As can be seen in Figure 4.2, a small amount of light is picked off from the main beam using a beam splitter that reflects a small amount of light on both the front and back surfaces. We use an acousto-optic modulator (AO) to shift the frequency of light from that produced in the dye laser. An AO uses a piezo-electric transducer to generate acoustical waves in a crystal. These waves create a periodic change in the index of refraction of the crystal, which acts as a grating. The laser light is then split into zeroith and first order modes each traveling outward from the AO at a different angle. The angle and frequency shift of the first order mode is determined by the drive frequency. Each mode corresponds to a different frequency shift.

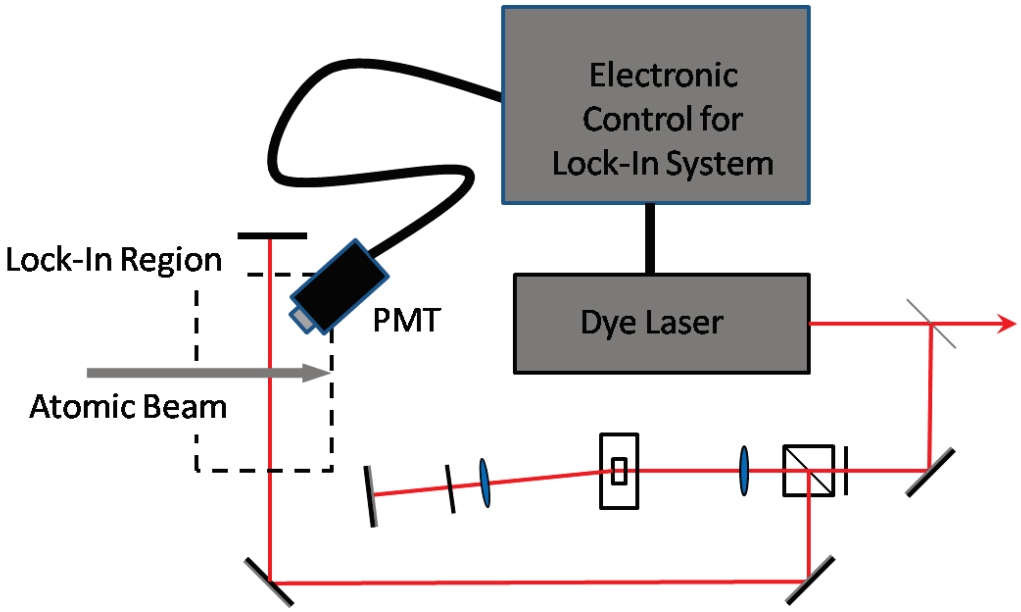

Figure 4.2: The dye laser produces light which is upshifted by a double pass AO arrangement. This light intersects atoms produced by the locking oven. The light scatter from the atomic resonance is detected by a photo-multiplier tube (PMT) and used to lock the dye laser to the atomic resonance.

The AO is set up in a double pass arrangement (See Figure 4.2), which is used several times in our experiment as it allows us to keep the direction of the beam fixed. The double pass AO arm consists of a polarizing beam splitting cube (PBS), two lenses, a $\lambda/4$ waveplate and a mirror. A linearly polarized beam passes through the PBS and is focused onto the AO. We optimize the AO for the first order with an efficiency of about 80%. The first order mode passes through the $\lambda/4$ waveplate and is reflected back on itself, passing through the $\lambda/4$ waveplate again. This results in a 90 degree rotation of the polarization (i.e. if we started with horizontal polarization we will end up with vertical polarization and vice versa). The light is then focused back onto the AO where its frequency is shifted again. After the light is recollimated, it is now reflected by the PBS as its polarization has been flipped. The AO is placed at the focus of the two lenses of the system so that any angle displacement of the first

order mode is

The total shift we produce in the double pass AO arm is about 200 MHz. In Section 2.3 we discussed the electronic ground state of ^{6}Li. Figure 4.3 shows the excited state transitions. The dye laser can be scanned in frequency through its control box. We tune the laser frequency such that the light intersecting the atoms is close to the D_2 transition. At this point we can resolve the hyperfine structure of the ground state. We choose to lock the laser to the $F = 1/2$ to $^2P_{3/2}$ transition. This is done by setting up a feedback loop to the laser control box. A photo-multiplier tube (PMT) collects the florescence signal generated by the atoms. Then we modulate the frequency shift produced by the locking AO. The modulated signal resonance signal detected by the PMT is sent into a lock-in amplifier along with the original sinusoidal modulation. The lock-in amplifier produces a signal that is the derivative of the atomic resonance with respect to the frequency of the light (zero if we are sitting on top of the peak, positive if we are below the peak, and negative if we are above the peak). The output of the locking amplifier is then sent to the frequency control of the dye laser, insuring that the dye-laser stays 'locked' to the atomic resonance.

4.3 Zeeman slower

The atoms leave the oven at speeds around $v_{atoms} = 1.4 \times 10^3 m/s$ and enter the slower. The atoms are hit by light tuned to the D_2 line shown in Figure 4.3 (minus the upshift from the locking AO). However, due to the speeds at which atoms are traveling, the resonance is Doppler shifted. The frequency of light that the atoms see,

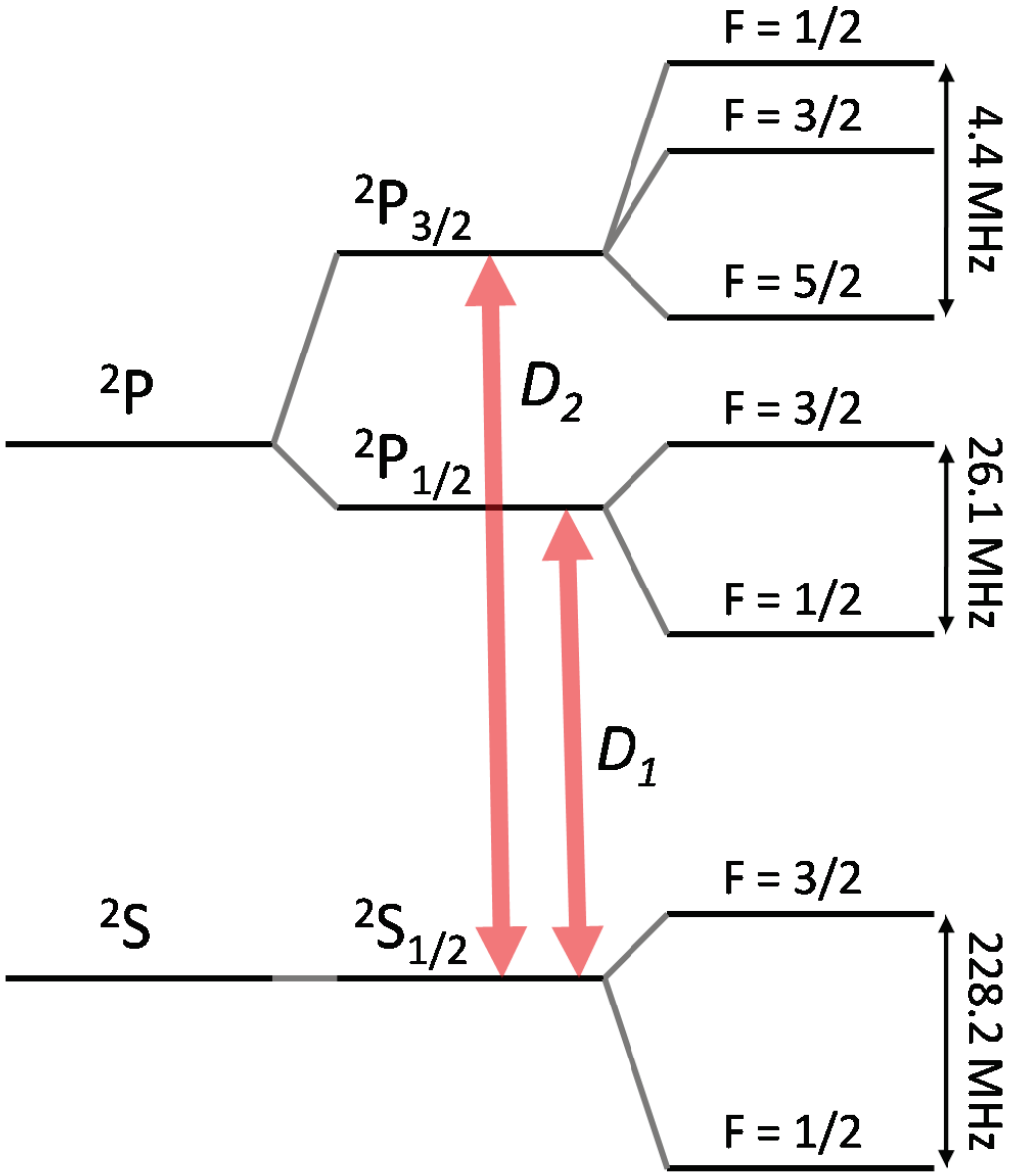

Figure 4.3: Energy level diagram of the ground and 2P states of ^{6}Li. The wavelength of light needed to excite from the ground state to either 2P states is approximately $\lambda = 671nm$. The frequency difference between the 2P excited state transitions is $D_2 - D_1 = 10.056GHz$. Each hyperfine consists of a number of degenerate states corresponding to F quantum number (i.e. $F = 3/2$ is four fold degenerate with $m_F = (-3/2, -1/2, 1/2, 3/2)$).

$\nu_{Doppler}$ is increased by the speed at which they are traveling,

$$\nu_{Doppler} = \nu_0(1 + \frac{v_{atoms}}{c}), \tag{4.1}$$

where ν_0 is the wavelength of the incident light, and c is the speed of light.

In order for the light to be absorbed by the atom, we must shift the atomic resonance. This is done by the Zeeman slower. As its name implies, the magnetic field supplied by the Zeeman slower shifts (a shift due to an applied magnetic field) the atomic resonance frequency. Comprised of 10 coils (see Figure 4.4) the slower provides a continuous magnetic field. The field is greatest near the oven, where $\nu_{Doppler}$ is largest.

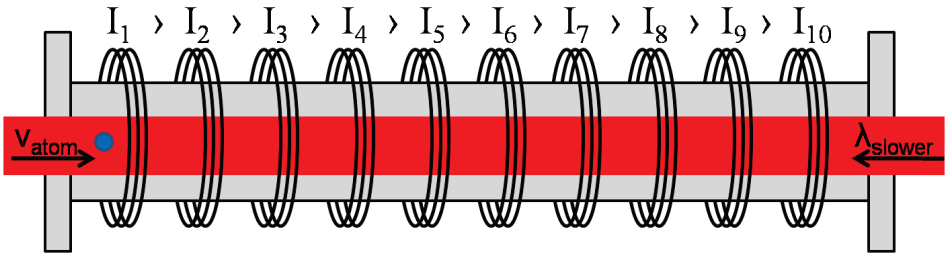

Figure 4.4: The Zeeman slower is comprised of ten electro-magnetic coils. The current in each coil decreases from the entrance (oven) to the exit (main chamber). The magnetic field Zeeman shifts the atomic energy levels to stay in resonance with the light as the atoms decelerates throughout the slower.

An atom absorbing one photon laser light receives a momentum kick equal to the momentum of the photon. The resultant change in velocity is,

$$\Delta \mathbf{v} = \frac{\hbar \mathbf{k}}{m} \tag{4.2}$$

where $\mathbf{k} = 2\pi/\lambda$ is the wave number for the incident light and m is the mass of ^{6}Li. The atom then emits the photon in a random direction. An atom must absorb

approximately 14 thousand photons in order to decelerate to zero velocity. Each time an atom absorbs a photon, the deceleration changes the magnitude of the Doppler shift. Therefore, the current in each of the coils is calibrated such that the atoms are constantly in resonance with the incident light [80].

Considering the fact that the atoms are nearly always on resonance with the light due to the magnetic field supplied by the slower, there is a constant decelerating force on the atoms. This is called a radiation pressure force and can be characterized by the wave number of the incoming light and the photon scattering rate, Γ_{sc}. The slower decelerates the atoms from 1.4 kilometers per second to around 30 meters per second over the course of the one meter length of the slower. The acceleration associated with the Zeeman slower is,

$$a_{rad} = \frac{F_{rad}}{m} = \Gamma_{sc}\hbar\mathbf{k} \approx 4 * 10^5 \, meters/second^2. \tag{4.3}$$

The frequency and polarization of light incident on the atoms is chosen carefully [64] to insure a two level system. We use laser light straight out of the head of the dye laser which is shifted about 200 MHz below the D_2 line of ^{6}Li. Further, we use σ^+ circularly polarized light.

4.4 Magneto-optical trap (MOT)

If the Zeeman slower does it job, the atoms will exit as a slow moving atomic beam with a velocity of approximately 30 meters per second, ready to be captured in the MOT. The MOT in turn builds up atomic density in the center of the vacuum chamber and cools the atoms so that they can be efficiently loaded into the dipole trap. The

standard MOT (shown in Figure 4.5) is comprised of three sets of counter-propagating laser beams aligned along orthogonal axis. In addition to the optical beams, there exists a magnetic field generated by two coaxial electromagnetic coils whose combined magnetic field is centered on the intersection point of the optical beams. The current in each coil is applied in opposing directions (anti-Helmholtz). As a result, they produce a spherical, quadrapole field with a zero field point centered at the intersection of the optical beams.

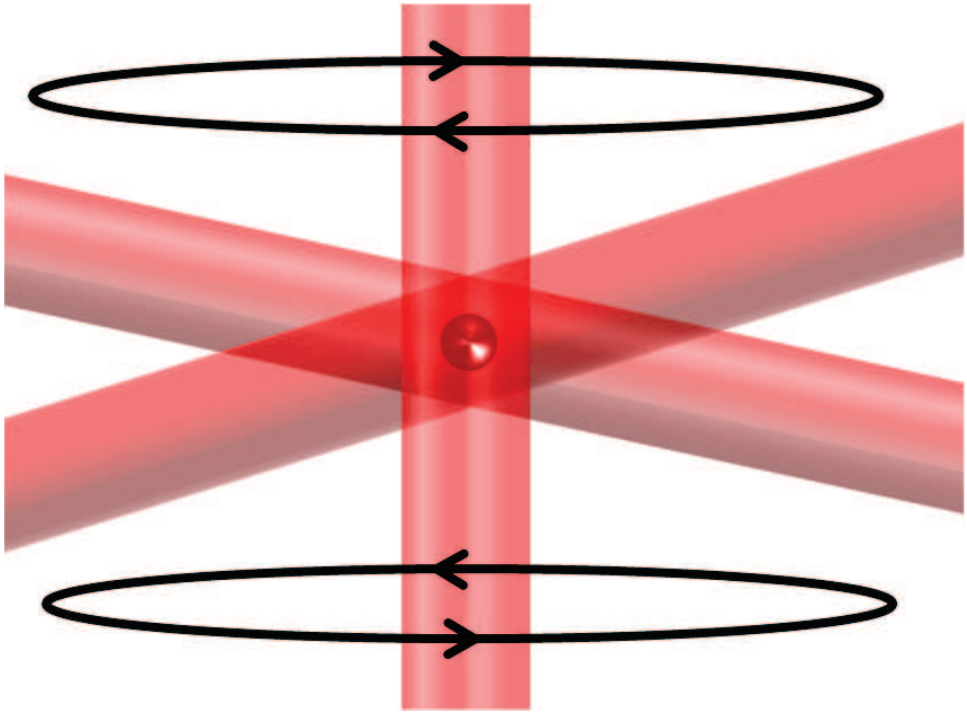

Figure 4.5: The MOT traps and cools atoms coming out the Zeeman Slower. 3 orthogonal, counter propagating beam pairs along with a magnetic field generated by two electromagnetic coils operating in an anti-Helmholtz configuration confines the atoms in both momentum and space.

4.4.1 Basic MOT physics

The MOT provides confinement in both space and momentum. First, consider the one-dimensional analogue to the three dimensional MOT wherein two counter propagating beams are incident on an atom with a velocity only along the direction of the propagating beams. As mentioned in the previous section, an atom moving in the presence of near resonant light will experience a radiation pressure force that depends upon the frequency of the laser light as well as the velocity of the atom, due to Doppler shift. By red shifting the two counter propagating beams (i.e. detuning the frequency of light below the atomic transition) we can use the Doppler shift to confine the velocity of the atom. This is known as optical molasses. If we tune below the atomic resonance then an atom moves towards one of the beams it becomes more in resonance, scatters more photons, and receives a larger force in the direction opposite to its velocity. Extend this analogue to three dimensions and the MOT effectively cools the atoms by damping their velocity.

The spatial confinement is a combined result of the magnetic and optical fields. The spherical, quadrapole field can again be viewed in a one-dimensional analogue wherein the gradient of the field varies linearly and is zero at the center $\frac{d\,\mathbf{B}}{d(\mathbf{x})} = x\hat{i}$ center. To further simplify the problem we will consider an atom whose ground state total angular momentum is $F_g = 0.$ and whose excited state total angular momentum is $F_e = 1$. The effect of a magnetic field on the excited state is to Zeeman tune the $m_F = 0, \pm 1$ sublevels of the excited state. The fact that the field varies linearly about a zero point means that the Zeeman tuning will shift the excited state energy differently on either side of the center of the field. Where the field is negative the $m_F = 1$ excited state sublevel energy will decrease. Where the field is positive the $m_F = -1$ excited state sublevel energy will decrease.

We use circularly polarized light to excite from the $m_F = 0$ ground state sublevel to the $m_F = \pm 1$ excited state sublevel (σ^+ circularly polarized light will excite the atom to the $m_F = 1$ sublevel, and σ^- circularly polarized light will excite to the $m_F = -1$ sublevel). Now consider two counter propagating beams with opposite circular polarizations. We have already stated that in order to form an optical molasses we red shift the light from resonance. Now all we have to do is assign the appropriate polarization to each beam. In the one dimensional analogue this means that the beam propagating in the positive direction must have σ^+ polarization. Therefore, any atom that wanders into the region of space where the magnetic field is negative (i.e. $x < 0$) will preferentially absorb a photon from the beam of light propagating in a positive direction and receive a momentum kick in back to the center of the trap. And vice versa for σ^- polarization in the counter propagating beam.

Indeed this is what we do. The combined effect of the optical and magnetic fields is to confine the atoms in both space and momentum. As the electronic structure of Li_6 is more complex than the simple model we constructed here, there are other considerations that need to be made.

4.4.2 The ^{6}Li MOT

The ground state and excited state energy levels are shown in Figure 4.3. Ideally, MOT beams would excite a two level transition without access to any other energy levels. In this scenario an atom would access the excited state by absorbing a photon and return to the original ground state once that photon had been emitted. This is not the case for ^{6}Li. The MOT beams are shifted in frequency to excite transitions on the D_2 line of ^6Li from the $F = 3/2$ ground state. This has the unfortunate consequence that once in the excited state the atoms can fall back into either ground

state. Therefore we must add an additional beam, called the "repumper" beam, that excites on the D_2 line from the $F = 1/2$ transition. The manner in which we create and combine the laser light is shown in Figure 4.6.

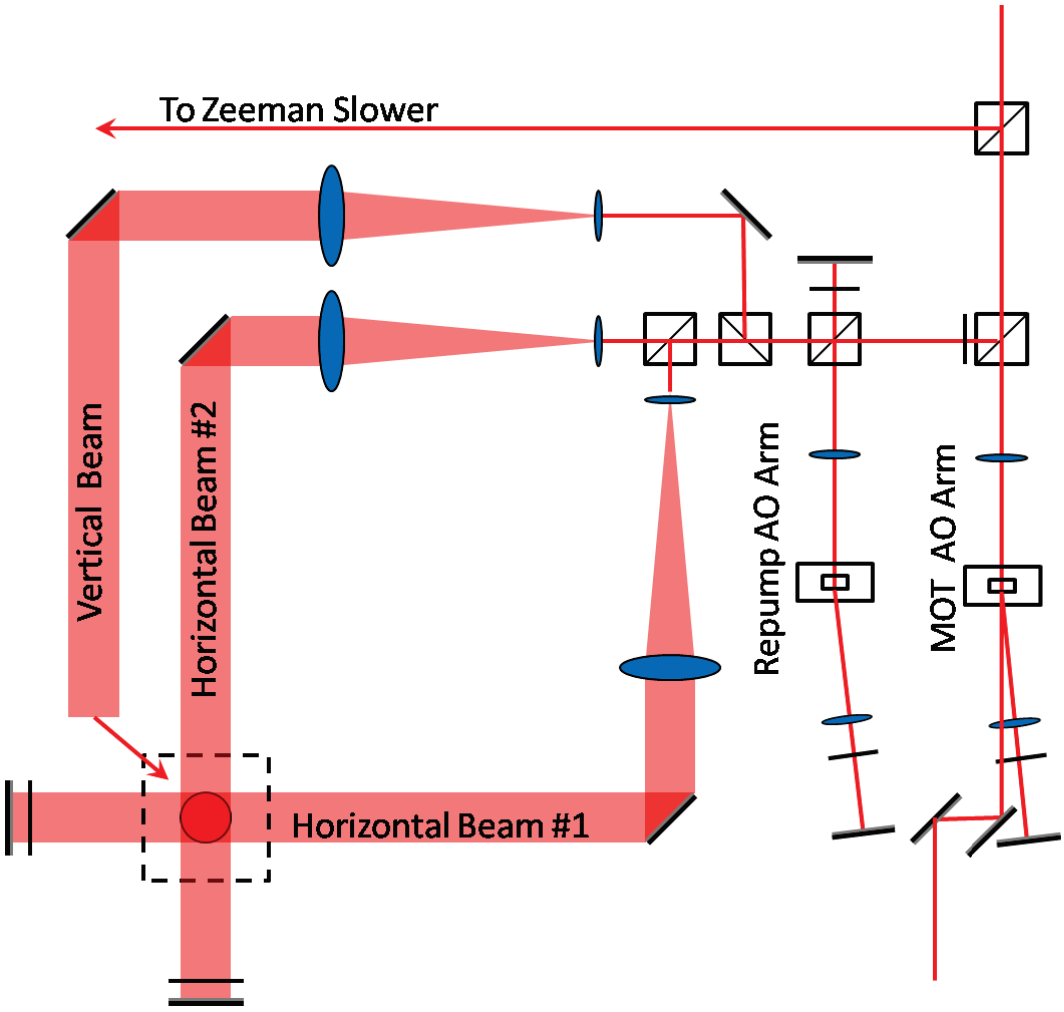

Figure 4.6: Assorted optical and electronic components used to generate the MOT beams. The MOT beams frequencies are selected by two double pass AO arms. Wave plates and polarizing beam splitting cubes are used to split the light. Telescopes are used to expand the beam.

In the locking region AO arm we down shift the light approximately 200 MHz and lock this to resonance. Therefore the light coming out of the laser is actually

200 MHz above the resonance from the $F = 3/2$ ground state to $^2P_{3/2}$ transition. In order for the MOT to work the light must be red-shifted (i.e. tuned below the resonance. Therefore we need to shift the light once more. This is done in the MOT AO arm. In this arm the frequency of the laser light is shifted to roughly 30 MHz below the $F = 3/2$ ground state to $^2P_{3/2}$ transition. Then a portion of laser light is split off from the MOT beam and sent into the repump AO arm. Here the light is down shifted roughly 230 MHz so that it is roughly 30 MHz red detuned from the $F = 1/2$ ground state to $^2P_{3/2}$ transition. The ratio of the MOT to repump beams is optimized on the MOT signal, and is about 3:1.

The MOT can only cool the atoms to the Doppler limit. For ^{6}Li the Doppler limit is 140 μK. The set up I described above does not actually cool to this limit. It is set up for fast loading of the MOT with a significant number of atoms. Furthermore, we are excited our atoms with bicromatic light and accessing both ground states. Therefore, two more phases of the MOT are required. We call these phases the "cooling phase" and the "optical pumping" phase.

In the cooling phase the MOT and repump beams are shifted closer to the atomic resonance and lowered in intensity. This causes and increase in the density of the MOT and a decrease in temperature near the Doppler limit. This phase lasts 200 ms. Next, we need to populate only the $F = 1/2$ ground state. We do this by turning off the repump beam. This then prohibits the excitation of the $F = 1/2$ ground state. Only the $F = 3/2$ atoms are excited, and after a few cycles this state is depopulated as the atoms can relax to either ground state. This phase lasts 200 μs. After the cooling and optical pumping phases the atoms are as cold and as dense as they will ever be in a MOT. They are ready to be loaded into the dipole trap.

4.5 Radio frequency antenna

There are many uses for the radio frequency (RF) antenna. At the beginning of each experiment we use it to equalize the population of states $|1\rangle$ and $2\rangle$ by applying a noisy pulse. If we were to simply broadcast the RF signal at a single resonant frequency the states would flip flop and it would be difficult to time the pulse to create an equal mixture. To equalize the spin states we first tune the high field magnets to approximately 8 Gauss. Then we broadcast an signal centered on the Zeeman shift between states $|1\rangle$ and $2\rangle$ at approximates 8 MHz. The signal contains a 2 MHz random noise bandwidth. The large bandwidth and small magnetic inhomogeneity insures that the populations will equalize to a 50:50 mixture of the lowest two spin states.

The RF antenna is comprised of two electronic feed-throughs that enter into the vacuum chamber. Attached to these cylindrical metal rods is a piece of wire bent into a rectangular loop. This is by no means an efficient antenna. Most of the power sent to the antenna is reflected back upon itself. However, we do not need much power to excite RF transitions.

The energy difference between states $|1\rangle$, $|2\rangle$, and $|3\rangle$ is well within the RF frequency range. In Section 2.3 I described the electronic ground state of ^{6}Li. After the optical pumping phase of the MOT we are left with atoms in the $F = 1/2$ ground state. When an external magnetic field is applied the degeneracy of the this state is lifted and we can resolve the lowest two spin states, $|1\rangle$ and $|2\rangle$. At high field the splitting between these states is approximately 80 MHz. Further, the splitting between states $|2\rangle$ and $|3\rangle$ at high field is also around 80 MHz (See Figure 2.2).

These transitions are experimentally accessible with our current setup. The RF

antenna is a powerful tool that can be used for a variety of experiments. We are already using RF transitions to precisely determine the magnetic field [84] and create a spin polarized gas [83]. Other uses include creating unequal spin mixtures [86] and exciting the $|2\rangle$ to $|3\rangle$ transition to measure molecular binding energy [85].

4.6 Far off resonance trap (FORT)

Once the atoms are trapped and cooled in the MOT, the MOT beams are turned off. Now the atoms are contained in the potential well generated by the CO_2 beam. The physics of a dipole trap was covered in Section 2.1. Further we discussed the various interactions accessible to the trapped atoms in Section 2.3. Experimentally there are few techniques we can use to cool the atoms further cool once they are confined in the potential well of the CO_2 laser.

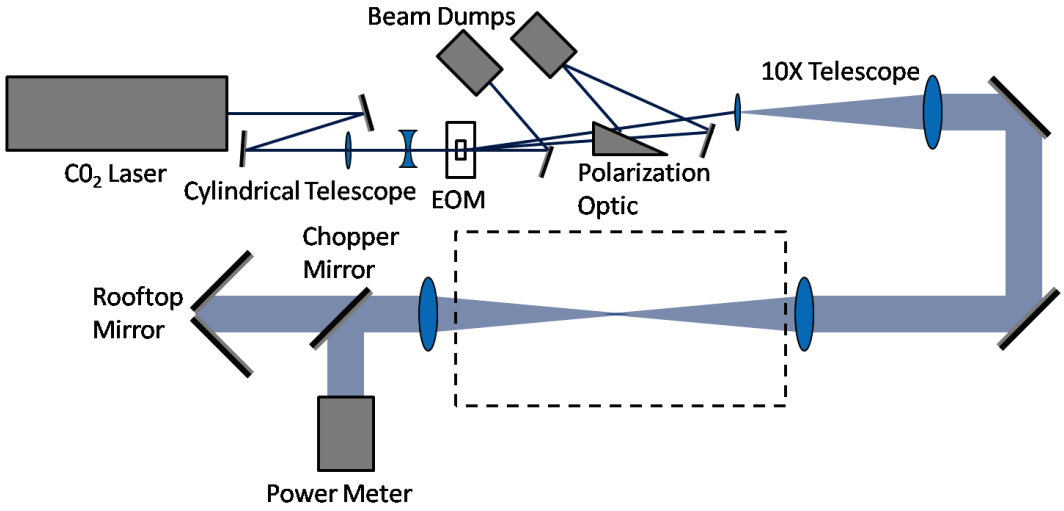

Figure 4.7: Proper conditioning and control of the CO_2 beam used for the dipole trap requires: a cylindrical telescope, a control AO, a polarization optic, a 10X expanding telescope, two focusing lenses, a rooftop mirror, a chopper mirror, two beam dumps, and a power meter.

Figure 4.7 shows the optical beam path traveled by the CO_2 laser beam in our experiment. First, the beam is conditioned by a set of cylindrical lenses. We use this cylindrical telescope to insure that the beam curvature matches in both the horizontal and vertical directions perpendicular to the direction of propagation. Meaning that when the curvatures are matched the position of beam focus along the axis of propagation (z-direction) will be identical for the two directions perpendicular to beam propagation. By adjusting of the last lens of the cylindrical telescope we can change the ratio of the trapping frequencies in all three directions. As noted in Section 2.1 the trapping frequencies depend on the spatial size of the trapping potential. Therefore, the elipticity of the beam is directly related to the ratio of the two radial trapping frequencies (x- and y- direction). However, it is not always in our best interest to match these two frequencies exactly. We must balance a matching of curvature with a zeroing of beam elipticity.

Next, the beam passes through an AO, which operates in the same manner as the AO discussed previously but needs 40 MHz. We send two frequencies into the AO at 32 MHz and 40 MHz. The AO is aligned for maximum power in the 1st order mode of the 40 MHz beam (around 70 %). We use two frequencies in order to maintain constant power to the AO so that the index of refraction remains constant. This avoids unwanted changes in the beam angle. During our forced evaporation procedure, which will be discussed in detail in Section 4.6.1, we lower the amplitude of the 40 MHz signal, thereby lowering the intensity in the 1st order mode of the 40MHz beam. Simultaneously, we increase the amplitude of the 32 MHz signal maintaining constant RF power into the AO. We do this in order to insure temperature stability in the AO. More information on limiting noise in the CO_2 beam can be found in Reference [14]. After the AO we have three beams with significant intensity. The zero order beam

and the 1st order mode of the 32 MHz beam are sent to beam dumps.

The beam then passes through a polarization optic, which passes horizontal polarization and reflects vertical polarization (The polarization coming out of the CO_2 laser is linear and horizontal). After the polarization optic the beam is expanded in a 10X telescope. The expanded beam is steered to the UHV system. Just before entering the vacuum, it passes through the front lens which has a focal length of 19.5 cm. The front focusing lens is the primary element that determines the FORT position. It is carefully aligned such that the focus of the lens is centered in the magnetic field generated by the high field coils. This alignment procedure is explained in detail in Section 4.6.4. Upon exiting the UHV system the beam is recollimated by the back focusing lens.

Depending upon the where in the timing sequence the experiment is, the beam will either be directed into a power meter that also serves as a beam dump, or it will reflected back upon itself by the rooftop mirror. The is done by an actuated mirror known as the "chopper" as shown in Figure 4.7. The rooftop mirror is comprised of two mirrors at a right angle to one another. The line which marks the intersection of the two mirrors is positioned at a 45 degree angle to the polarization of the beam. The rooftop mirror serves the dual purpose of reflecting the beam as well as flipping the polarization. Therefore, the polarization of the back-going beam will be at a 90 degree angle to the front going beam. This is done in order to insure that there are no interference effects when both beams are 'on'. Once the back reflected beam reaches the polarization optic it is reflected into a beam dump. This is done so that the beam does not reenter the CO_2 laser.

4.6.1 Evaporative cooling

Evaporative cooling, as its name implies, is a process wherein the temperature of the gas is reduced by allowing "hot" escape from the trap. A "hot" atom is characterized by its large kinetic energy. An atom can gain kinetic energy through collisions with other atoms. When these "hot" atoms leave the overall temperature of the gas decreases. We can cool through evaporation either passively or actively. The atoms will collide and exchange energy. Atoms that gain enough energy will exit the trap. We can increase the evaporation rate through two methods. We can increase the number of collisions by turning on strong interactions between the two trapped spin states, and we can lower the trapping potential making it easier for an atom to leave the trap.

There are three distinct evaporative processes during a typical experiment. First, we reduce by half the intensity of trapping light by lowering the chopper mirror and diverting the back reflected beam into a power meter, as discussed in the previous section. Second, we use the magnetic field to turn on interactions at 300 G and allow the gas to rest at this field at a fixed trap depth. This is free evaporation. Finally, we lower the intensity of the trapping beam in such a way as to minimize the final temperature of the gas. This is forced evaporation and is either done in the weakly interacting regime at 300 G, or more efficiently in the strongly interacting regime at 834G.

4.6.2 Forced evaporative cooling on resonance

The forced evaporation process performed at 834 G cools the strongly interacting gas to a temperature of 10 nK. After the beam intensity is lowered, it is held at

the low well value. During this low well interval a certain amount of free evaporation occurs. The lower the intensity of the beam the better able we are to achieve near zero temperature conditions. The most important factor in achieving the lowest possible well depth is the alignment of the FORT and the center of the high field coils which would otherwise distort the trap. The details of this alignment procedure will be discussed in Section 4.6.4. Next we use an exponential curve to re-raise the trap to our desired trapping potential. Typically, we perform our experiments on the gas at this stage of the lowering curve, which is know as the "high flat time". A typical lowering sequence is shown in Figure 4.8.

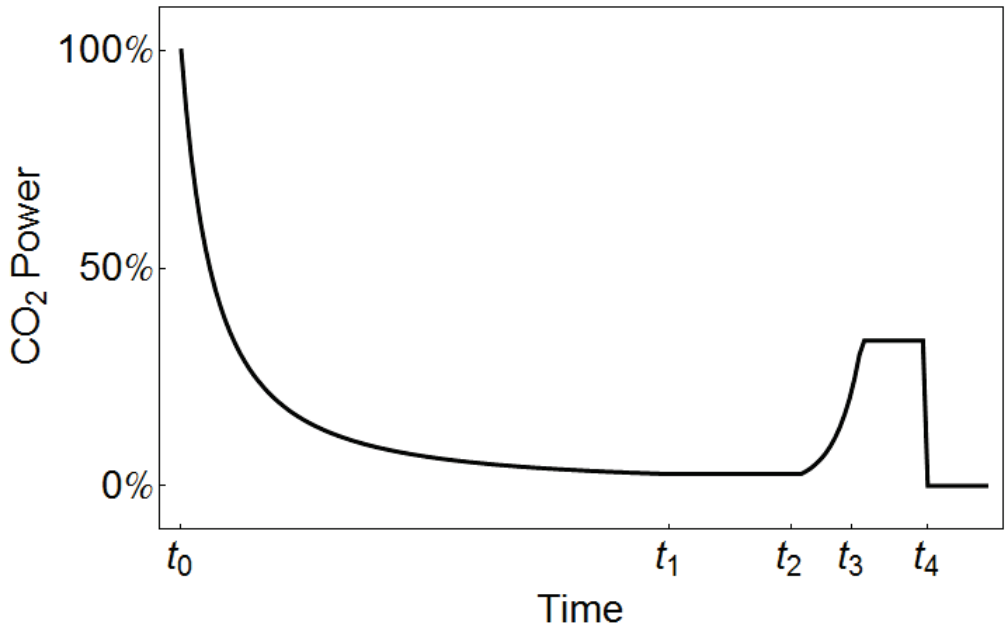

Figure 4.8: Typical lowering curve for cooling a Fermi gas in our experiment

Our goal is to maximize the temperature loss of the gas. For example, if we allow the system to sit indefinitely at the same trapping potential, eventually the probability of an atom acquiring escape velocity through collisions will become small. We can

increase the probability by tuning to a region of strong interactions where collisions will occur more frequently. However, eventually we need to lower the amplitude of the trapping potential to allow more atoms to escape. It is important that this is done is such a way as to maximize temperature loss. The lowering sequence shown in Figure 4.8 consists of four distinct stages. First, we lower the trap according to the equation,

$$U(t) = U_0 \left(1 + \frac{t}{\tau}\right)^{-1.44615} \tag{4.4}$$

The above equation was developed to take advantage of the natural scaling laws of the system [79]. As the trap is lowered the evaporation slows and the lowering rate is slowed to compensate.

For a typical experiment at 834 G the parameters of the lowering curve shown in Figure 4.8 are, with $\tau = 0.08\,s$ from in equation (4.4). This means that the low well

Time Point	Value (s)
t_0	0
t_1	4
t_2	4.5
t_3	4.7
t_4	5.2

Table 4.2: Time points for a typical lowering sequence at 834 Gauss

value of the trap will be about 0.34% of the maximum value. By carefully aligning the FORT on the magnetic field we can further decrease this value to 0.068%. This is done by adding an offset to the lowering curve. The offset value maintains a continues curve but adjusts the lowest value. For example, if the lowest value was originally 1% of total trap depth, a 25% offset would reduce the lowest value to 0.75%. The offset typically used for our forced evaporation at 834 G is 80%. In our experiment we use a 4 s lowering curve with a time constant of $\tau = 0.08\,s$. With an offset of 80% our

lowest trap depth is 0.068%.

4.6.3 Forced evaporative cooling of a BEC

The sound velocity experiment was the groups first attempt at measurements on zero-temperature systems through the entire crossover region. There were many issues to overcome. One such issue is the fact that while we cool most efficiently at 834 G, some of our measurements needed to be performed at other magnetic fields. The Pauli Exclusion principal dictates that no two fermions can occupy the same energy level of a system. Therefore, a zero temperature Fermi gas has more energy than a fully condensed Bose Einstein Condensate with the same number of atoms is the same trapping potential. When we tried to simply switch fields to the weakly interacting Bose region we found that the condensates we were producing had typical Boltzmann tails (i.e. the density of the outer gas scaled exponentially, while the inner gas formed a dense peak that scaled like a BEC). In order to cool the gas further we needed to add an additional lowering curve (Figure 4.9)

This lowering curve is concurrent with a magnetic field switch. The magnets take approximately 0.6 s to change fields. Most of the field change occurs in the first few tenths of a second. We begin the field switch just before the second lowering curve. This way the atoms are already forming into molecules and condensing into a BEC. As they do this they will lose internal energy. This energy needs some place to go and results in an increase in temperature. Therefore, just as the temperature increases, we are already providing additional forced evaporation. The result is a fully condensed BEC. Again we rest the atoms at a new low well value, and then re-raise the trap to some final well depth. Typical time points associated with this lower curve are, where the time constant associated with the first lowering curve remains $\tau_1 = 0.08s$.

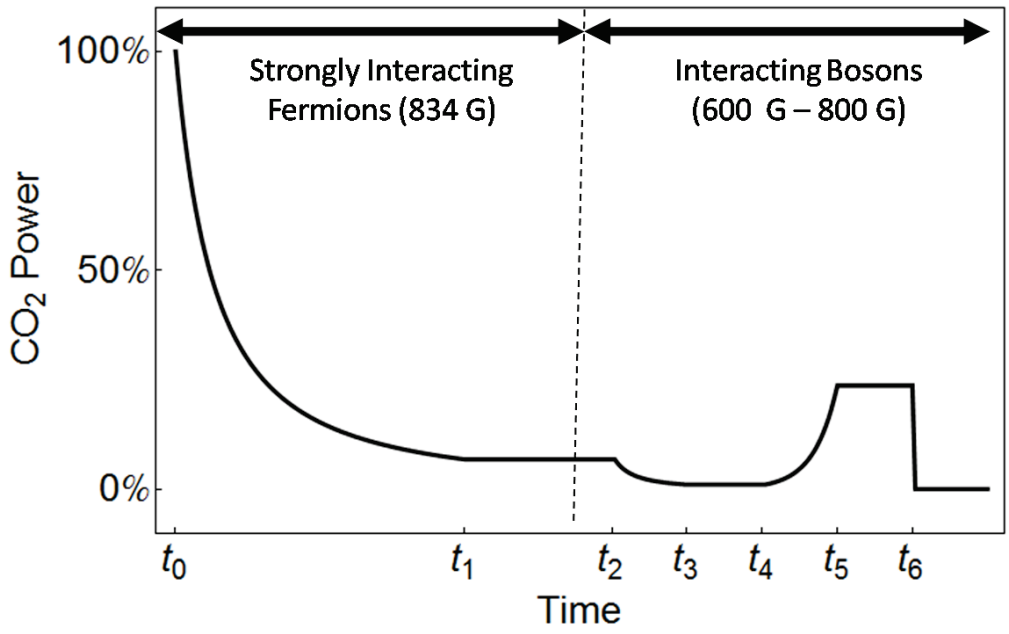

Figure 4.9: Lowering curve used to generate near zero temperature BECs. Initial lowering occurs at 834 G, then the trap is lowered further as the magnetic field is tuned into BEC side of resonance.

Time Point	Value (s)
t_0	0
t_1	4
t_2	4.4
t_3	4.5
t_4	4.7
t_5	4.9
t_6	5.4

Table 4.3: Time points for a the production of a BEC; Lowering begins at 834G, and additional lowering is accompanied by a field switch to the weakly interacting Bose region

The time constant associated with the second lowering curve is $\tau_2 = 1s$. There is also an additional offset value that depends upon the field we are switching to and controls the lowest trap depth achieved in the additional cooling process. Table 4.4 contains the appropriate values for the additional offset at a variety of fields as well as the lowest trap depth.

Field	Offset	Low Well Value
710 G	60% G	0.023%
735 G	60%	0.023%
775 G	30%	0.042%
815 G	15%	0.051%

Table 4.4: Experimental parameters for a the production of a zero temperature gas on the BEC side of resonance; Lowering begins at 834G, and additional lowering is accompanied by a field switch into the Bose region

4.6.4 Optical and magnetic bowl alignment procedure

During evaporative cooling the intensity of the CO_2 laser is lowered to a small fraction of its original value. When cooling in the strongly interacting region at 834G the trap is lowered to 0.068% of its maximum value. For the production of BECs this value is even smaller. With the optical potential so small, the axial confinement of the atoms is dominated by bias magnetic field curvature. Also, the radial confinement has small contributions from the magnetic field as well. We found that we could improve cooling by exactly centering the dipole trap on the magnetic field center. At high field the magnetic field is generated by two coaxial coils running parallel current. This generates a large field at the dipole trap. The potential generated by the field is due to the magnetic field curvature. It is attractive in the plane perpendicular to the magnet coils and is repulsive along the axis of the coils.

For the purposes of this experiment the camera beam propagates along the axis of the magnetic field coils (y-axis). The pictures taken of the atoms will then be in the plane perpendicular to the coils where the magnetic field potential is attractive (x- and z- axis). Therefore, the first alignment step is simple. We allow the gas to expand from the low well for a long period of time, and we track the center of mass movement of the atoms as the gas expands. When we are close to the center this can be as long as 5 ms. If the gas has any translational movement on the screen we follow up with a corresponding change in the position of the front focusing lens of the CO_2 beam. This change can be along the axial (z-direction) of the trap or the radial direction of the trap that is the plane of the pictures (x-direction). However, any change in the front focusing lens must be followed by the same change in the back focusing lens so as to maintain overlap when both beams are present. These first few changes (axial) of the trap as well as

Centering the focus of the CO_2 beam in the other direction (y-direction) is trickier. Any change in the FORT position in this direction will only show up as a change in the focus of the picture, not in any change of position. The solution comes from two experimental observations. First, we see a dramatic loss of atoms below a certain trap depth when we are off center. Second, the more aligned the dipole trap and magnetic field are, the shallower trapping depths we can achieve. Therefore, we can lower the trap depth to the point where we see dramatic atom loss. Then we adjust the front focusing lens of the CO_2 and either see either a further reduction in atom number or an increase in atom number. Again the back focusing lens must be adjusted by the same amount in the same direction.

Care must be taken when making any adjustment to the CO_2 lens system. A large change to the front or back focusing lens can direct the retro-reflected beam

to an unsafe place resulting in damage to the system (or the system's operators!). Therefore any change to the position of either lens must be done is small increments. I would recommend starting with a change of 5 microns or less on either lens and then increasing the adjustment once one knows the effect these adjustments have on the CO_2 beam location at every location along its beam path. Furthermore, there might be some coupling between the various axes of the front focusing lens due to the fact that the camera plane on the atoms is not exactly orthogonal to the corresponding two axis of the CO_2 beam focus. However, I found that making this adjustment greatly increases the cooling efficiency of the system and allows us to trap more significantly more atoms at near zero temperature. This is especially important when we run our secondary lowering curve to create fully condensed BECs, which require very shallow traps due to their small chemical potential.

4.7 Absorption imaging

At the end of each experimental sequence we take a picture of the atoms. This is the primary method of extracting information from the experiment. In our experiment we use a process called absorption imaging. We hit the atoms with on resonant light and then look at the shadow cast upon a charge coupled device (CCD) array. Therefore, we are imaging the shadow cast when light is absorbed by the atoms. We acquire images using an Andor Technology DV434-BV CCD camera. The camera has a 1024 $\times$ 1024 array of 13 μm square detectors.

The beam used for absorption imaging is produced in the red beam conditioning system (See Figure 4.10) and sent into a fiber optic cable.

The optical beam layout used to image the atoms is shown in Figure 4.11. Also

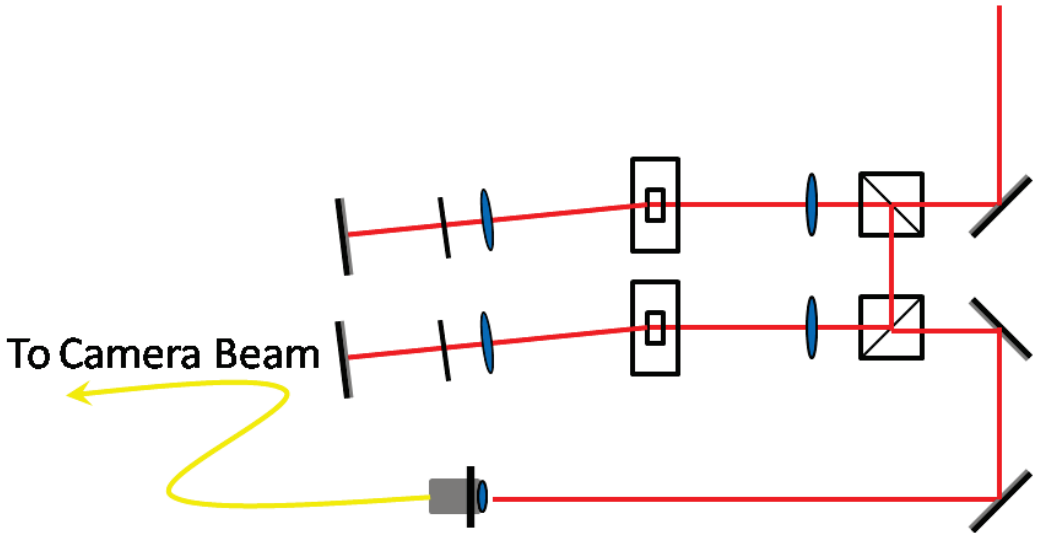

Figure 4.10: The camera beam goes through two double pass AO arms and enters into a fiber optic launch.

shown is the image path of the atoms. As the beam leaves the fiber optic cable it is expanding. We position a lens to collimate the beam. The focus of the collimated lens is selected to produce a large diameter beam (approximately 2.5 cm). The beam then passes into the UHV system and is incident on the atoms. Upon exiting the UHV system it passes through an imaging lens, gets partially blocked by a razor blade and then goes through a microscope objective before it reaches the CCD array.

The optical elements between the atoms and the CCD array a placed to transfer an image of the atoms to the CCD array. The first lens positions the image of the atoms in the plane of the razor blade. The purpose of the razor blade will be explained shortly. Then, the microscope objective places the image of the atoms on the CCD image array.

We utilize the fast kinetics function of our Andor camera. When a photon hits a pixel of the CCD camera a charge forms on that pixel. In a fast kinetics sequence the electrons associated with a row of pixels is shifted to the row below it. Once the

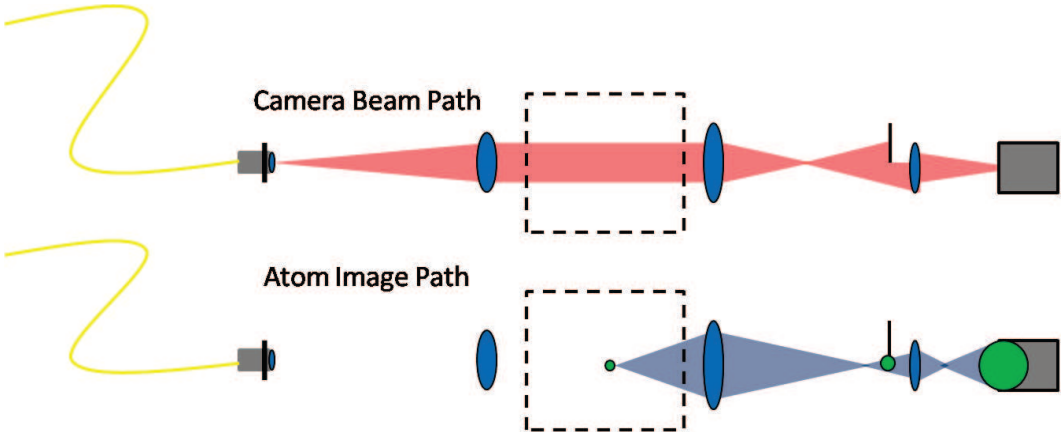

Figure 4.11: Some of the light in the camera beam is scattered off the trapped atoms. The lens system between the atoms and the camera beam is designed to place the image of the atoms in the plane of the CCD array.

electrons reach the last row they can be read out by Andor software. The reading time is much longer than the time it takes to shift a row. The razor blade shades 2 thirds of the CCD array. Immediately after a the image containing the atoms shadow is obtained one third of the CCD array is shifted down to the dark area of the array. Then we can take a reference shot on the cleared pixels and use the fast kinetics function to shift again. The information is then transmitted out of the camera. Taking a reference shot greatly reduces the noise in our signal.

A description of how this image is processed to determine atomic density can be found in Section 5.5. The spatial resolution of the images is about 2 pixels at the CCD array. Once we consider the magnification of the lens system this results in an image resolution of around 5 microns at the atoms.

Chapter 5

Sound velocity experiment

This Chapter highlights the experimental and analytic steps taken in order to obtain a measure of the sound velocity. The speed at which sound travels depends on the nature of the substance through which it travels. The sound velocity is a basic quantity that is intimately related to the equation of state. A sound wave is, in essence, a moving pressure gradient. The velocity of the pressure gradient tells us about the equation of state of the gas, therefore, something about the gas itself must be known. To this end we not only measure the sound velocity but the ideal gas Fermi energy, E_F which determines the ideal Fermi velocity $v_F = \sqrt{2E_F/m}$. We present our measurements in the form of the sound velocity at the center of the trap in units of the ideal gas Fermi velocity, i.e. $c(0)/v_F$.

In the previous chapter I described how ^{6}Li is trapped and cooled. In this chapter, I will discuss how we excite the sound wave (Section 5.1) and investigate the dynamics of the wave propagation (Section 5.2). In order to obtain a good measure of the sound velocity, the excitation of the sound wave must be gentle to remove nonlinear effects. It is shown in Section 5.2.2 that through our analysis of the nonlinear effects of sound propagation we are able to extrapolate the sound velocity to the zero perturbative case. Further, we must understand the geometry of the propagating feature in order to best determine the velocity from density profiles produced in the experiment (Section

5.3).

All of our measurements take the form $c(0)/v_F$. c(0) is, of course the speed of sound at the center of the trap in typical *length/time* units. v_F is the Fermi velocity of an equivalent ideal gas. In order to obtain one data point, we perform both a sound velocity experiment and a breathing mode experiment in order to evaluate c(0) and v_F, respectively. As discussed in Section 2.2, for an ideal gas at zero temperature $E_F = \hbar\overline{\omega}(3N)^{1/3}$ and $v_F = \sqrt{2E_F/m}$. This means that v_F depends on two measurable quantities, the atom number N and the average trap frequency $\overline{\omega}$. We use the breathing mode experiment in conjunction with a separate parametric experiment that measures the individual trap frequencies in order to determine $\overline{\omega}$ (Section 5.4). The atom number, N, is determined from the sound velocity data in order to insure the most reliable measure of v_F (Section 5.5).

5.1 Exciting a sound wave

We excite a sound wave using a blue detuned laser at 532 nm. The atoms are trapped in the potential well generated by our CO_2 laser. The atoms have a cigar shape, long in one cartesian coordinate (z-direction) and short and cylindrically symmetric in the other two (x- and y-directions). The blue detuned beam, when incident on the atoms is shaped by a cylindrical telescope and when focused on the atoms is a repulsive sheet potential. At the intersection between the repulsive optical potential and the atoms the optical intensity varies in one direction (z-direction) and from the point of view of the atoms extends out infinitely in the other two directions (x- and y-directions) While the atoms are sitting in the CO_2 trap the excitation potential is introduced at the axial center, perpendicular to the z-axis of the trap, and then removed. The

atoms at the center of the trap upon which the light is incident are repulsed from the region of highest intensity. A density perturbation forms and propagates outward from the center of the trap along the z-axis as a plane wave.

We can increase the repulsive force generated at the atoms by adjusting the intensity of the blue detuned beam. Our blue detuned beam originates from a Coherent Verdi^{TM} V-10 Diode-Pumped Laser which produces coherent light at 532 nm. We use the Verdi^{TM} as a pump for our dye laser. However, the dye laser only requires 5.5 Watts of power while the Verdi^{TM} can put out up to 10 Watts. With the use of two half-wave plates and a polarizing beam splitting cube we can pick off part of the 532 nm beam, Figure 5.1. By adjusting the total power out of the Verdi^{TM} and the

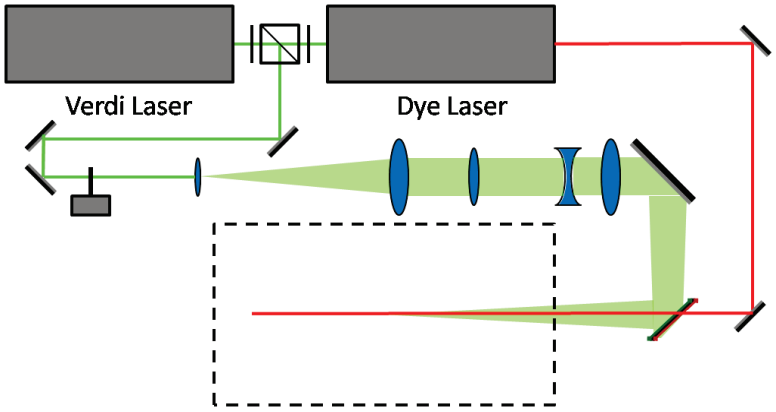

Figure 5.1: Beam path of the 532 nm laser light: the light is expanded and then shaped by a cylindrical lens telescope before it is focused on the trapped atoms.

two waveplates we can maintain constant power to the dye laser and vary the power in the beam used to excite the sound perturbation. The beam then passes through the pinhole and is expanded by a telescope. Then it is shaped by a set of cylindrical lenses that changes the elipticity of the beam. Next the beam passes through a lens that focuses it on the atoms. Before entering the UHV system the beam is reflected off a bichromatic beam splitter. As there is limited access into the UHV system, the

green beam is passed into the system through the same port as the slowing beam. These beams are combined at the bichromatic beam splitter which passes light at 671 nm and reflect light at 532 nm.

We apply the repulsive force for only a short amount of time, $\Delta t = \simeq 280\mu$s. This is done by passing the beam through a pinhole that is attached to a solenoid. The beam is positioned so that it is blocked initially, but then is allowed to pass as the pinhole moves through the beam, Figure 5.2. The pinhole mechanism was originally designed and constructed by Bason Clancy.

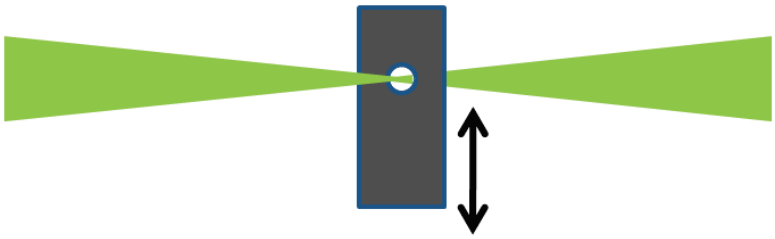

Figure 5.2: The green light is applied only for a short time as it passes through a pinhole.

The physics of the production of the density perturbation is relatively simple. The electric field of the blue detuned beam induces an out of phase dipole that is repelled from the high intensity region. The atoms then move according to the interaction of the induced dipole and the beam's electric field. The potential generated by the induced dipole is,

$$U_{dip} = -\frac{1}{2}\alpha\overline{\mathbf{E}^2}, \tag{5.1}$$

where the bar indicates that the electric field is averaged over many cycles. As we are working with optical fields we can assume a sinusoidal variation in the electric field such that $\mathbf{E}^2 = \mathcal{E}^2/2$. Then the potential can be written in terms of the field

intensity $I = \epsilon_0 c \mathcal{E}^2$,

$$U_{dip} = -\frac{1}{2\epsilon_0 c}\alpha I, \tag{5.2}$$

where ϵ_0 is the permittivity of free space and c is the speed of light. As I, ϵ_0, and c are all positive quantities in order to have a repulsive for the polarizability must be negative, which occurs for blue detuning.

Now that we know the potential our incident light generates, in order to determine the forces on the atoms we need to assess the geometry of the beam. As stated before the beam acts as a sheet potential incident on the axial center of the trapped atoms, as can be visualized in Figure 5.3. The intensity of light must therefore reflect this

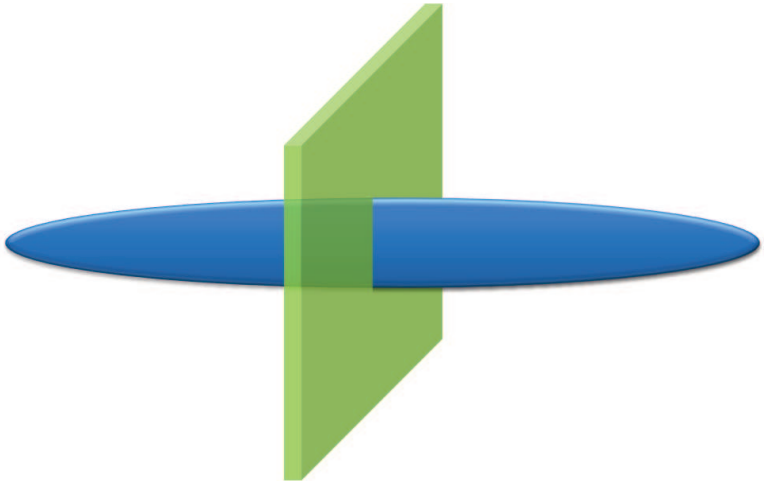

Figure 5.3: A sheet potential of green light incident on the axial center of the trapped atoms

geometry. For a gaussian beam propagating in the x-direction the intensity can be represented by

$$I(x, y, z) = \frac{I_0}{1 + \frac{x^2}{x_0^2}} \exp\left(-2\frac{z^2}{z_0^2} - 2\frac{y^2}{y_0^2}\right), \tag{5.3}$$

where I_0 is the maximum beam intensity and z_0, x_0, and y_0 represent the spatial size of the beam. The value of x_0 is the rayleigh length, which depends on the beam profile,

$x_0 = \pi z_0 y_0/\lambda$. Our beam is passed through a cylindrical telescope such that at the focus of the beam $z_0 \approx 10\,\mu m$ and $y_0 \approx 150\mu m$. This means that $x_0 \approx 9\,mm$. As the trapped atoms are only about 25 microns wide in the short direction of the trap (x- and y-directions) and 150 microns wide in the long direction (z-direction), the beam can be considered constant in x and y directions and the perturbation created will be small in comparison to the long axis of the atoms. The sheet potential produced is then,

$$U_{dip}(z) = -\frac{1}{2\epsilon_0 c}\alpha I_0 \exp\left(-2\frac{z^2}{z_0^2}\right). \tag{5.4}$$

The force applied is only in the axial direction of the trap or along the short spatial profile of the incident beam, z. This leads to a force on the atoms of $\mathbf{F} = -\nabla U$, or

$$\frac{\partial U}{\partial x} = -\frac{z}{z_0^2 \epsilon_0 c}\alpha I_0 \exp\left(-2\frac{z^2}{z_0^2}\right). \tag{5.5}$$

The polarizability for the ground state of ^{6}Li is [63]

$$\alpha = \frac{\alpha_0 \omega_0^2}{\omega_0^2 - \omega^2}, \tag{5.6}$$

where α_0 is the static polarizability for the ground state of ^{6}Li, ω_0 is the transition frequency for the ground state of ^{6}Li and ω is the frequency of the incident light. For our experiment, $\alpha_0 = 24.310^{-24} cm^3$ [68], $\omega_0 \approx 2\pi c/671$ nm and $\omega_0 \approx 2\pi c/532$ nm. This means that the polarizability of an optical field with a wavelength of $\lambda = 532$ nm incident on ^{6}Li atoms is

$$\alpha \approx -1.7\alpha_0. \tag{5.7}$$

The fact that our polarizability is negative indicates that our potential will indeed be repulsive. We now have a way of characterizing the force imbued by our 'sheet'

potential.

5.1.1 Green beam alignment procedure

Both the focus of the green beam and the gas of atoms trapped in the CO_2 beam potential are very small. Our job is made even more difficult by the fact that we are focusing our beam from so far away. We're trying to hit a very small object with an even smaller bullet from a great distance away. Fortunately, we have other means to align our lens system on the target atoms. Namely, light from the dye laser. We expend a lot of effort to make sure that we do not have any red light entering into the system during the evaporative cooling phase of our experiment. A few mW of power from a stray beam can deplete the FORT of atoms.

Therefore, we pick off a portion of the dye laser beam going into the locking region that we know is resonant with the atoms. Then we introduce a few mirrors to align this beam along the green beam path prior to the pinhole shutter. Next, we adjust the pinhole shutter to pass our test beam. Due to the fact that the light is on resonance there is a dramatic atom loss in the FORT when the beam is nears alignment. We use a florescence signal from the atoms right after they are loaded into the FORT at zero field. This is called the FORT probe experiment.

Initially, we concentrate on the two direction perpendicular to beam propagation. We make adjustments on the last mirror before the light enters the UHV system. Then we add a few optical density filters and re-peak atom loss. Once we reach the point where the signal can no longer be completely destroyed by this adjustment we can align in all three direction. The position of the focus of the green beam can be adjusted by moving the focusing lens on a translation stage along the propagation direction. An additional optical density filter may need to be added to maintain

signal from the atoms.

Once the position of the red beam is maximized we can repeat this procedure, now using the green beam and judging the focus position based upon absorption images. We know that the beam is aligned when the dip in density is at the center of the trap and maximized.

5.2 Dynamics of sound pulse propagation

Care was taken insure a precision measurement of the sound velocity. We claim that the data produced in this experiment is a test bed for theoretical prediction. In order to insure that our data is reliable we devoted ourselves to understanding the dynamics of sound propagation. In this section I will describe the evolution of the sound experiment, and the steps taken to insure a deep understanding of the details of sound propagation particular to our experiment.

Initially, we created a density perturbation and saw that it propagated through the trap. We recognized that the gas was exhibiting hydrodynamics and that the measurement of hydrodynamic sound propagation was possible. Next, we scrutinized the nature of the sound wave. In doing so, we found ways to eliminate all of the systematic errors we could identify. The systematic errors that will be reviewed in this section include residual movement of the released atoms and deviations due to nonlinearity in the propagation.

As the density perturbation travels through the cloud, successive pictures are taken. We can determine the velocity of the position of the perturbation as a function of time. As a first try, we excited a sound wave at one edge of the cloud. We tracked the position of the density perturbation as it moved across the entire cloud.

Inconsistencies in the data and led us to conclude that there was a some unaccounted velocity. In Section 5.2.1 I will describe our investigation into this matter and how it was resolved.

Moreover, we noticed that the density feature we were tracking was more complex than we originally assumed. Initially we expected to create an increase in density as the atoms were repulsed from the green beam and pushed into adjacent atoms. We would then track this density peak. Upon closer observation of the actual sound wave we discovered that not only did the density peak propagate, but the density depression or valley propagated as well. In Section 5.2.2 highlights the analysis and resolution of this nonlinear effect.

5.2.1 Measurement of sound in two directions

It was discovered that there were inconsistencies in the velocity measurements at identical trap depths. We took a close look at the data and soon discovered that the entire cloud of atoms had some initial velocity along the long axis of the trap. Moreover, the center of mass motion was not consistent for different re-raise times or final trap depths. It was concluded that we were exciting a "slosh" mode during the cooling procedure when the CO_2 beam intensity is lowered and then re-raised to a final trap value.

Competing against the optical confining potential was the magnetic field potential. If the two potentials are not perfectly overlapped the gas will migrate towards the magnetic potential center when the optical intensity is low. Then upon re-raise the combined center shifts again and the gas oscillates. This effect is seen most strongly along the long axis (z-direction) of the trap. The direction along which we track the sound perturbation. This effect was skewing the measurement, either adding to or

subtracting from the actual sound speed depending upon how the gas was moving. The period of the sloshing frequency in comparable to the speed of sound in the axial direction.

We tracked the center of mass of the atom cloud over a period of time and were able to see it oscillate. It may have been possible to correct for this additional velocity

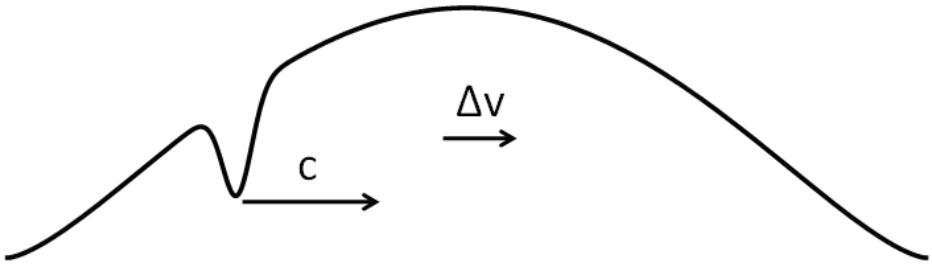

Figure 5.4: If the atoms have an initial velocity the speed of sound measurement will be skewed.

on a case by case basis. Instead we opted for a simpler solution. We decided to excite the sound wave in the center of the trap and track the two counter propagating waves.

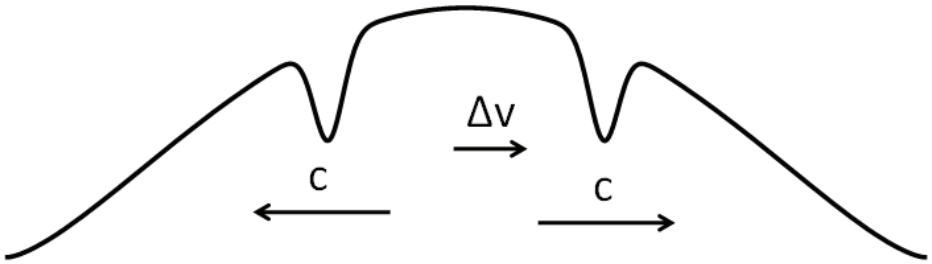

Figure 5.5: By tracking two sound waves traveling in opposite directions we are able to disregard any additional velocity the atoms may have.

While each perturbation might have an additional velocity component with respect to the trap center, the mean velocity of the waves with respect to each other will remain constant. A simple average of the two separate velocities will yield an

uncorrupted speed of sound,

$$c = \frac{c + \Delta v}{2} + \frac{c - \Delta v}{2}. \tag{5.8}$$

5.2.2 The peaks and the valleys

When we looked closely at the density perturbations we created we observed a non-trivial shape to the propagating features. Initially, the green beam creates a valley in the center of the trap bordered by two peaks. As the perturbation travels outward the valley splits in two. Each counter propagating wave contained a density peak and a density valley. Furthermore, we discovered that these two features propagated at different speeds (Figure 5.6). The fact that the sound wave is comprised of both

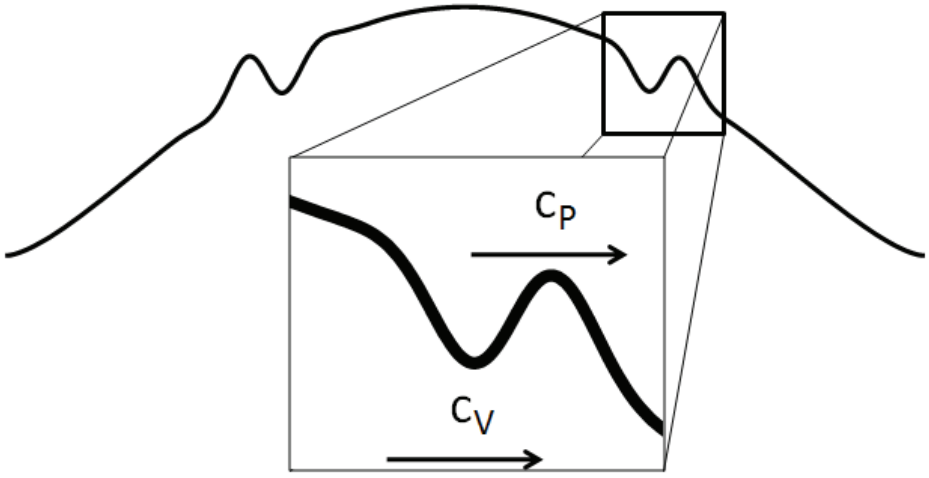

Figure 5.6: The propagating density perturbation is comprised of a region of increased density (peak) and decreased density (valley) which travel at different speeds.

an increase and a decrease in density begs the question, which feature represents the true sound velocity for the equilibrium density.

What we discovered when we started analyzing the data was that the peaks move

noticeably faster than the valleys. This makes sense as the peaks exist is regions of higher density. Further, it was found that for increasing green beam intensity the difference between the peaks and the valleys increased as the density in the peaks and valleys became more disparate. However, the average velocity remained the same, up to a point (see Figure 5.7). At very large green beam intensities the nonlinearity of

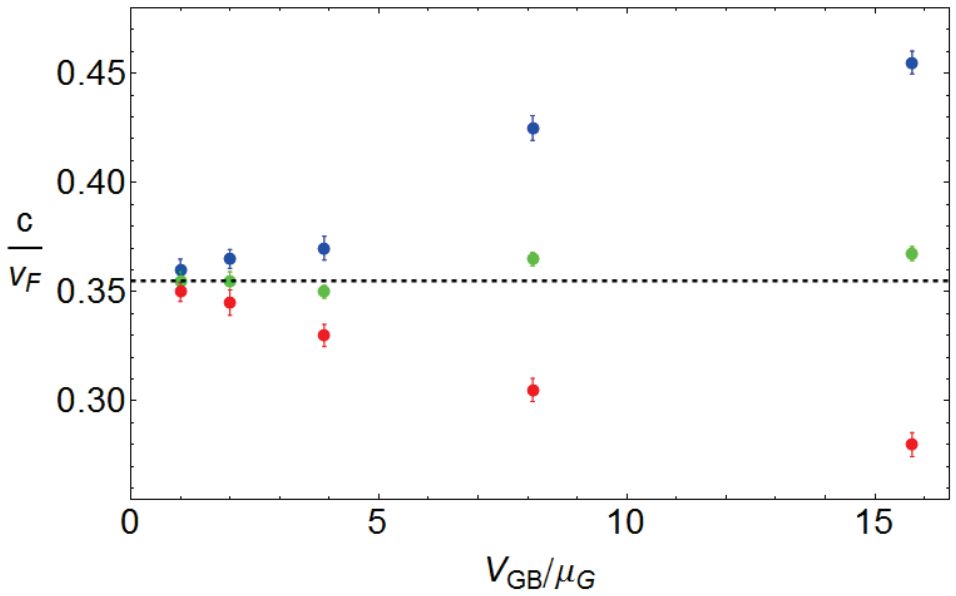

Figure 5.7: We measured the velocity of each feature of the propagating density perturbation, the peaks (blue/upper dots) and the valleys (red/lower dots) as well as the average velocity (green/open dots) as a function of the excitation potential intensity in units of the global chemical potential of the trapped gas.

the system becomes too great, and the average velocity no longer reflects the velocity at equilibrium density.

For each sound data point taken, an effort was made to optimize the sound excitation. We needed to balance the nonlinear response to the green beam intensity with our ability to identify the peaks and valleys above the noise in our signal as they traveled through the cloud. Thus we insured that for all our measurements the

green beam intensity was set below the point where nonlinear effects influence the average velocity. It is clear from Figure 5.7 that by measuring the velocity of both the peaks and the valleys we can extrapolate the zero perturbation result (i.e. the sound velocity with $U_{Dip} = 0$.

5.3 Sound velocity c(0)

Here I will go over the basic experimental procedure we used to track the sound pulse and the analysis techniques used to insure reliable data. The initial cooling and trapping of the gas, as well as imaging procedure is as described in Chapter 4. In addition to these procedures we excite the sound pulse and allow it to propagate through the gas. We use the signal received on a photodiode from the excitation light to mark the start of the sound pulse. When the sound pulse has traveled a predetermined amount of time we turn off the CO_2 laser trap, allow the gas to expand and then image.

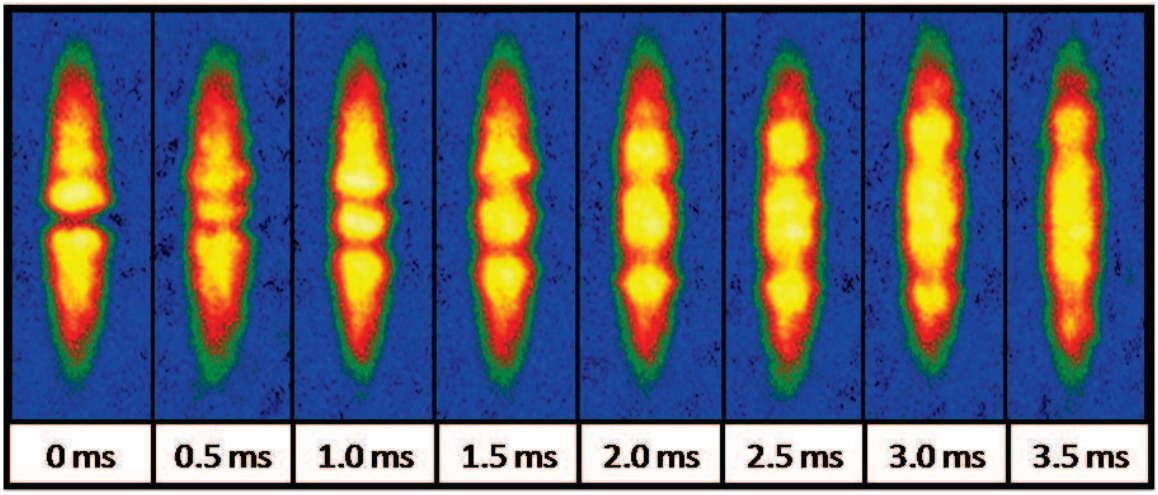

Figure 5.8: Absorption images acquired at different time points in a sound velocity experiment

The data acquired is a two dimensional absorption image as shown in Figure 5.8. This data is transformed into two-dimensional density (as explained in Section 5.5). We bin the data along radial (x- and y-direction) axis to obtain the one-dimensional density profiles for the long axis (z-direction). We also create an average binned axial distribution from all of the shots acquired in the data series, which we call the "Meta Average". The "Meta Average" includes all of the time points except for the time point of interest. We do this in order to create an average density profile with which to compare the density profiles at individual time points.

We take five shots for each time point. These shots are averaged together into a single "Signal" for each time point. In order to determine the peak and valley positions at each time point we take the difference between "Signal" profile and the "Meta Average" profile and termed this the "Difference" (i.e. "Signal" - "Meta Average" = "Difference"). We found that it facilitated analysis to only look at either the positive or negative deviation of the "Difference" profile. Values in the "Difference" profile greater than zero were set to zero in order to determine the position of the peaks, and vice versa for the valleys. Each feature was fit with a gaussian curve.

Figure 5.9 shows this process for one time step. Note that the valley "Difference" signal is made positive in order to see the feature more clearly. The position of the gaussian is recorded for each feature at each time point. We take approximately 11 time points and 5 trials at each time point for in for a single sound experiment. Each shot contains the position of four different features resulting in four data series in terms of position and time. We fit each of these data series, shown in Figure 5.10, with a sine function as discussed in Section 3.2.1.

The velocity at the center of the trap determined for each of the four features tracked in our experiment. The average velocity of the four features is taken as the

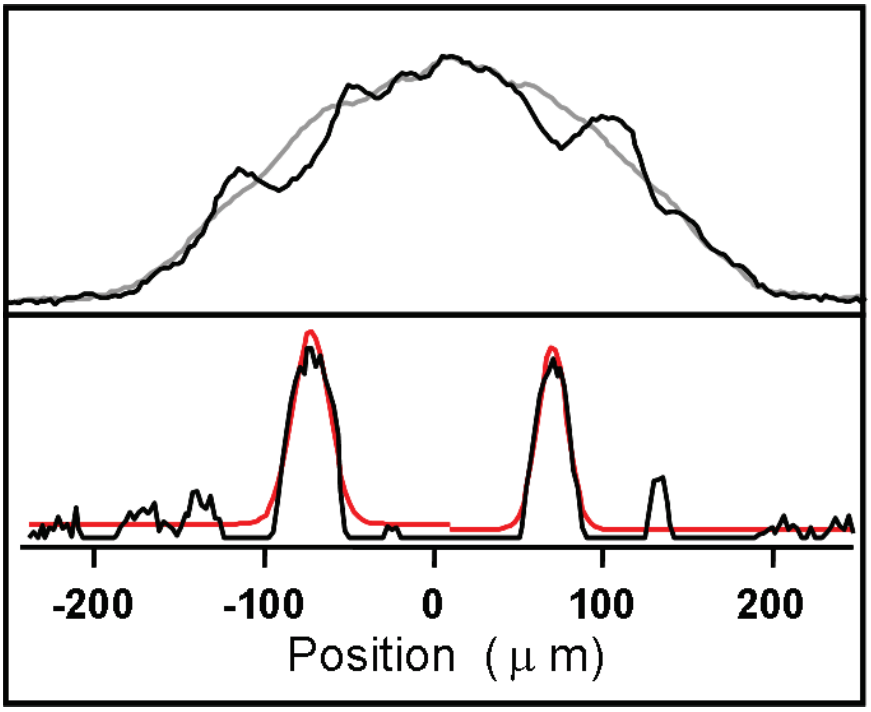

Figure 5.9: On top is a one-dimensional axial density profile of a single time point "Signal" (black curve) and the average profile "Meta Average" (grey curve). On the bottom is a profile generated by subtracting "Signal" profile from the "Meta Average" profile (black curve) and gaussian fits to the density valleys (red curve).

sound velocity for the experiment. By tracking both the peak and the valley in two directions we are able to eliminate systematic errors that arise from residual center of mass movement and nonlinear effects.

5.4 Trap frequency $\overline{\omega}$

The average trap frequency $\overline{\omega}$ is determined for each experiment using a breathing mode measurement. Before we perform the breathing mode measurement, however, we must measure the trap oscillation frequencies independently. Measuring the trap oscillation frequencies periodically provides a check on one of the most important factors determining the behavior of the trapped atom cloud, namely the confining potential. Once we have determined the relationship between all of our frequencies, we can then used our breathing mode measurement to calculate the average trap frequency $\overline{\omega}$.

5.4.1 Parametric resonance experiment

We use a technique called parametric resonance to measure the trap oscillation frequencies. This technique employs a small amplitude modulation of the optical trap at a particular driving frequency. If the driving frequency is at twice the trapping frequency the atoms will experience heating which can be seen experimentally as an increase in the size of the cloud. The resonant frequencies associated with the parametric resonance experiment are twice that of the trap oscillation frequencies, $2\,\omega_x$, $2\,\omega_y$, and $2\,\omega_z$.

The parametric resonance experimental procedure is as follows: First, we cool our atoms, comprised of the two lowest spin states, in the weakly interacting regime

(300 G) by lowering the power of the optical trapping potential. Then we reraise the power to the desired depth. At this point we apply the amplitude modulation which maximally heats the atoms at resonance. Next we ramp the magnetic field to the zero crossing (526 G) where the interaction between the two spin states is zero. Here we image the cloud and observe the mean size versus applied frequency.

We perform the parametric resonance experiment for a trap depth of 2% and find for the radial direction, the resonance frequencies are 1837(3) Hz and 1953(3) Hz (see Figure 5.11). At the same trap depth we find that the parametric resonance experiment gives an axial resonance frequency of 82.6(0.3) Hz (see Figure 5.12).

5.4.2 Breathing mode experiment

In order to confirm our parametric results we perform a breathing mode experiment in the non-interacting gas at 528G. A good discussion as to they dynamics of breathing mode oscillation can be found in Joe Kinast's thesis [65]. The basic procedure for the non-interacting gas breathing mode experiment begins the same way as the parametric resonance experiment. However, once we have re-raised our power to the desired depth we sweep immediately to 526 G. Then we turn the trap off for a short amount of time and then recapture the atoms. The time we choose is designed to allow the atoms expand for a short amount of time, while not imparting a significant amount of energy. The gas then oscillates in size around the equilibrium condition.

The breathing mode oscillation frequency depends on the atomic interaction energy and temperature. For a non-interacting, zero-temperature gas we can expect the oscillation frequency to be twice that of the oscillation frequency in the plane of the camera image. We performed this experiment at 526 G in a 2% trap. From Figure 5.13, we can see that the breathing mode oscillation frequency of 1947(6) agrees

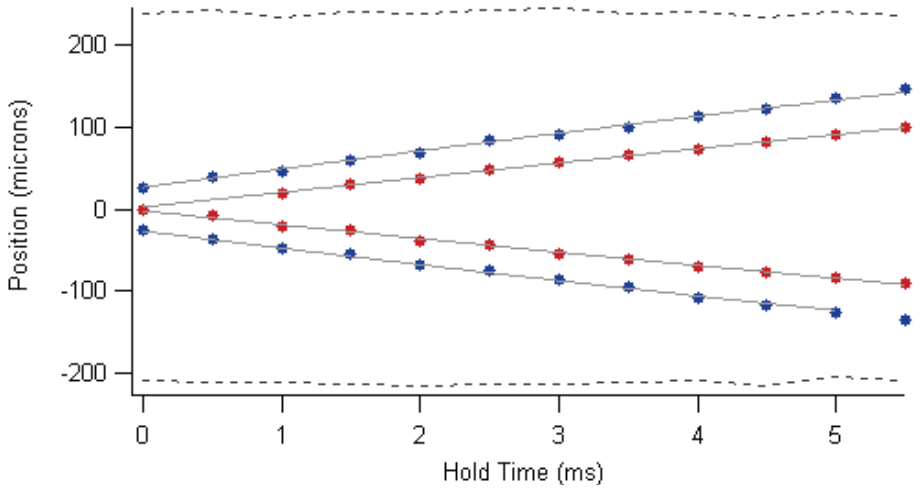

Figure 5.10: Displayed is the position versus time for each of the four sound features. The outer most data points (blue dots) are the peak position values, and the inner most data points (red dots) are the valley values. The grey dashed lines are the fits to the data using a sine function. The black dashed lines are the measured cloud border.

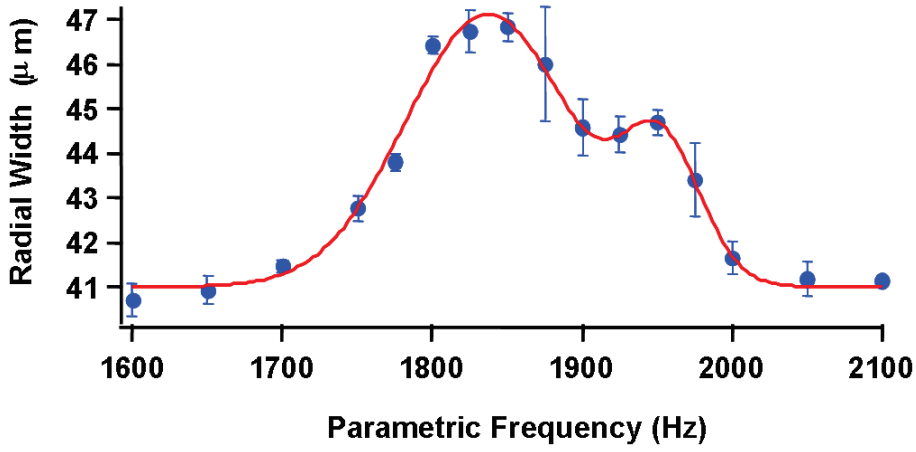

Figure 5.11: We performed the parametric resonance experiment at 300G in a 2% trap and imaged at 526G. Peaks were found at 1837(3) Hz and 1953(3) Hz.

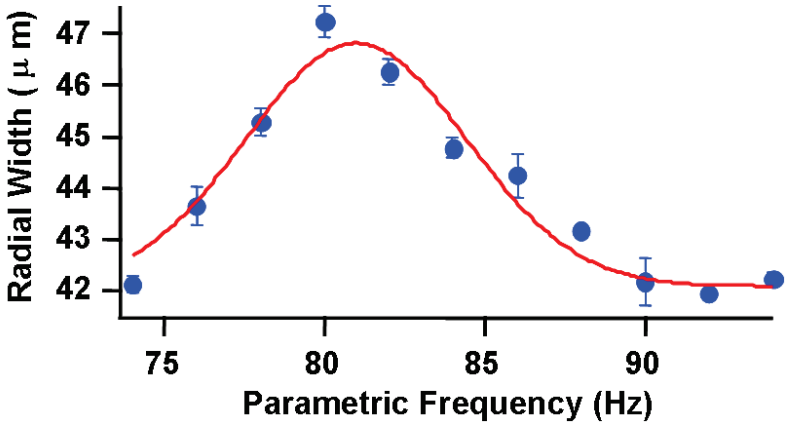

Figure 5.12: We performed the parametric resonance experiment at 300G in a 2% trap and imaged at 526G. A Peaks was found at 82.6(0.3) Hz.

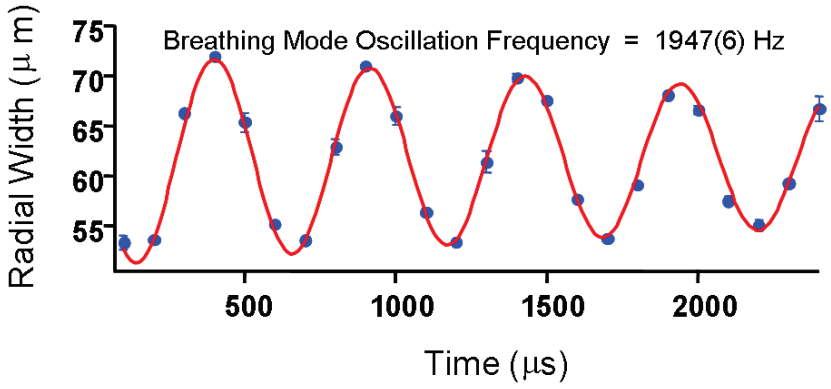

Figure 5.13: Breathing mode experiment at 526G for 2% trap depth. Oscillation frequency for fit is 1947(6) Hz

well with one of our parametric resonance frequencies, 1953(3). If we define the radial direction in the camera plane to be the x-direction we can now assign our trap frequencies.

$$\omega_x = 2\pi \times 977(3) Hz \tag{5.9}$$

$$\omega_y = 2\pi \times 919(2) Hz \tag{5.10}$$

$$\omega_z = 2\pi \times 41.3(0.2) Hz \tag{5.11}$$

5.4.3 Magnetic bowl frequency measurement

There is one more element of the trap oscillation frequencies to discuss. Not only are the atoms confined in an optical potential, but the are magnetic forces operating on the atoms as well. In general the radial optical trapping forces much larger than the radial magnetic trapping forces. However, in the long direction of the trap, the magnetic bowl forces become significant for shallow optical traps. Since the spring constants of the optical and magnetic potentials add, the total trapping frequency in the z-direction can be expressed as

$$\omega_z = \sqrt{\omega_{zOpt}^2 + \omega_{zMag}^2} \tag{5.12}$$

We can measure ω_{zMag} by releasing the gas at a very small optical potential that has been intentionally offset from the center of the magnetic bowl, and watching how the center of mass of the atomic cloud moves. In this experiment we cool at 834 G in order to reduce the optical potential by as much as possible. We stay at the extremely low optical potential and release the gas into the optical bowl. This way the gas expands slowly and we are able to observe the forces imparted to the atoms

by the magnetic field. Using a sine function fit to the position data the magnetic

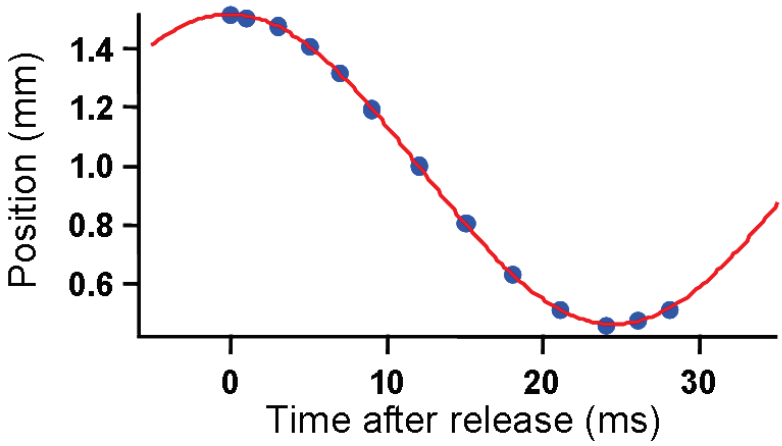

Figure 5.14: Magnetic bowl slosh frequency experiment at 834G. The optical trapping potential is turned off and position of the gas depends on the magnetic field gradient. Oscillation frequency for fit is 20.4(0.0) Hz

bowl oscillation frequency is 20.4(0.0) Hz at 834 G. The magnetic bowl frequency has a square root dependence on the total field strength, B, where

$$\omega_{zMag}(B) = 2\pi \times 20.4\sqrt{\frac{B}{834}}. \tag{5.13}$$

The parametric resonance experiments were conducted at 300 G. Therefore the axial optical frequency is,

$$\omega_{zOpt} = \sqrt{\omega_z^2 - \omega_{zMag}(300)^2} = 2\pi \times 39.4Hz \tag{5.14}$$

5.4.4 Average trap frequency $\overline{\omega}$

If we define $\omega_\perp = \sqrt{\omega_x \omega_y}$ as the geometric mean of the two radial trapping frequencies then we can express all of our trap oscillation frequencies as a product of $\omega_\perp$ and some

factor λ_i (i.e. $\omega_i = \omega_\perp \lambda_i$).

$$\omega_x = 1.03\,\omega_\perp \tag{5.15}$$

$$\omega_y = 0.97\,\omega_\perp \tag{5.16}$$

$$\omega_{zOpt} = 0.042\,\omega_\perp \tag{5.17}$$

Thus we can write the average frequency in terms of $\omega_\perp$ and the magnetic field as

$$\overline{\omega} = \left(\omega_\perp^2 \sqrt{(\lambda_z \omega_\perp)^2 + \omega_{zMag}(B)^2}\right)^{1/3} \tag{5.18}$$

where $\lambda_z = 0.042$.

When we perform the breathing mode measurement at 834 G the result is not twice the oscillation frequency in the camera plane because of the strong interaction between states the radial modes are hydrodynamically coupled. A good discussion of this effect can be found in Joe Kinast's dissertation [65]. The end result is that the breathing mode frequency measured is related to the optical trapping frequency through the equation

$$\omega_{BM} = \sqrt{\frac{3}{10}}\omega_\perp \tag{5.19}$$

We take a breathing mode measurement at 834 G at each trap depth where we perform a sound velocity experiment. With the above equations we can relate the breathing mode frequency to the average frequency $\overline{\omega}$ and thus have an accurate measure of the trapping potential for each sound velocity experiment.

$$\overline{\omega} = \left(\frac{3}{10}\omega_{BM}^2 \sqrt{\frac{3}{10}(\lambda_z \omega_{BM})^2 + \omega_{zMag(B)}^2}\right)^{1/3} \tag{5.20}$$

where B is the field at which the sound velocity experiment was performed and ω_{BM} is the breathing mode frequency measured at 834 G at the trap depth at which the sound velocity experiment was performed.

5.5 Atom number N

In Chapter 4 I discussed the basic procedure involved in acquiring an image on our CCD camera. In this section I will briefly review the physics behind how we turn this information into a measure of density. This is a typical procedure in quantum optics and atomic experiments and has been reviewed numerous times in many different sources. The basic procedure determines what the effect of a cloud of atoms of density $n(x, y, z)$ is on the intensity of a beam of resonant light.

$$\frac{dI}{dy} = -n(x, y, z)\sigma(I)I, \tag{5.21}$$

where I is the intensity of the light and $\sigma(I)$ is the intensity dependent cross section. The change in the intensity of light, I, as it travels through the atoms in the y direction is proportional to the intensity of the light, the polarizability of the interaction α and the density. For a two level system with near resonant light

$$\sigma(I) = \frac{\sigma_R}{1 + I/I_{sat} + \delta^2} \tag{5.22}$$

where $\sigma_R = 3\lambda^2/(2\pi)$ is the resonant optical cross section for a two level quantum transition at wavelength λ, $\delta = (\omega - \omega_0)/(\Gamma_s/2)$ is the detuning of the probe beam from resonance in half-linewidths, and I_{sat} is a the saturation intensity.

Assuming we have a measure of the intensity of light incident on the atoms in the

image plane of the camera $I(x,z)$ and a measure of the intensity of light before it hits the atoms $I_0(x,z)$, we can now use equation 5.21 to find the column density

$$n(x,z) = \int_{-\infty}^{\infty} n(x,y,z)dy \tag{5.23}$$

in terms of the detuning and our intensity profiles

$$n(x,z) = -\frac{1}{\sigma_R}\left((1+\delta^2)\ln\left[\frac{I(x,z)}{I_0(x,z)}\right] + \frac{I(x,z)-I_0(x,z)}{I_{sat}}\right) \tag{5.24}$$

There are further considerations when calculating the atom number. We need to know what the camera parameters are, the effect of the polarization of the imaging beam, and what the effect of the image lens system is in terms of attenuation and magnification. A good discussion of all of these issues and more can be found in Joe Kinast's dissertation [65].

The final result for column density is

$$n(x,z) = -\frac{mag^2}{\sigma_R}\left((1+\delta^2)\ln\left[\frac{I(x,z)+(\phi-1)I_0(x,z)}{\phi I_0(x,z)}\right] + \frac{I(x,z)-I_0(x,z)}{g_{cam}\eta_{cam}I_{sat}}\right) \tag{5.25}$$

where $\phi = 0.97$ is the fraction of the input probe beam which can be absorbed by the atoms do to beam depolarization, $g_{cam} = 0.71$ is the camera gain, $\eta_{cam} = 0.5$ is the camera efficiency, and $I_{sat} = 2660$ photons/pixel. In our measurements the camera gives us $I(x,z)$ and $I_0(x,z)$ in photons/pixel.

The actual size of our camera pixel is $13\mu m$ per side. Due to the image lens system this translates to $mag = 2.49\mu m$ at the location of the atoms. If our intensities are in units of photons/pixel we need an extra factor of 2.49^2 to account for the magnification and pixel size.

The final result for the total number of atoms is then

$$N = \int\int n(x,z)dxdz. \tag{5.26}$$

I have described how we produce and measure the velocity of a propagating density perturbation in our trapped gas. Further, I have described how we eliminate sources of systematic error and shown that we can account for nonlinear effects. The dynamics of the propagating feature are discussed as well. The trapping conditions are measured as well in terms of the trapping frequency and the number of atoms. In Chapter 6 I will demonstrate how we take into account the error in our measurements and correct the data for additional systematic effects including the anharmonic correction and a correction to the atom number measurement.

Chapter 6

Systematic and statistical error

In our experiment on the sound velocity near a Feshbach resonance, we collected large amount of data over a wide range of experimental condition. In addition to our measurement of the sound velocity conducted measurements of the trap frequencies and atom number in order to determine the characteristic energy of the trap, E_F. In Chapter 5 I presented a detailed account of each of these measurements. For each data point in the sound experiment we obtain a direct measurement of:

$$\begin{aligned} c(0) &: Sound\,Velocity \\ \omega_{BM} &: Breathing\,Mode\,Frequency \\ N &: Number\,of\,Atoms. \end{aligned}$$

Here I will review the process that takes us from our three measured quantities to the reported value of $c(0)/v_F$ vs $1/(k_F a)$ and their associated errors. In Section 6.1 I will review basic error analysis and show how error propagates from our measured quantities to our reported values.

There are both statistical and systematic errors associated with each measurement. For some systematic errors we have found a way to procedurally eliminate the source of error (see Chapter 5). For others we will need to determine a correction

factor to account for the bias in the measurement.

All of analysis thus far has considered a gas trapped in a harmonic potential. However, our optical trapping potential is Gaussian the radial direction (x- and y-directions) and Lorentzian in the axial direction (z-direction). Anharmonic effects are most significant at lower trapping potentials where the potential produced by the magnetic field curvature (which is harmonic) dominates in the axial direction. In Section 6.2 I will develop a correction factor that takes into account the systematic deviation due to anharmonicity.

There is also a bias in our number measurement. From shot to shot one expects some variation in the atom number. This may be caused by a number of factors in the trapping and cooling process. This should produce a normal distribution in the atom number. However, we end up with a skewed distribution due to the fact that any variation in the camera beam frequency results in apparent number loss. In Section 6.3 I analyze the skew distribution and determine a correction factor for the atom number.

6.1 Error analysis

A good example of both how we eliminate systematic error and propagate statistical error can be seen in the averaging of the four features we track in the sound velocity experiment. Recall that we create a density perturbation in the axial (z-direction) center of our cigar shaped trap and that two sound waves counter-propagate towards the edge of the trap along the z-axis. The sound wave is comprised of regions on increased density (peaks) and decreased density (valleys). Table 6.1 contains data from a typical sound experiment. The sound velocities come from a sine function fit

Sound Feature	**c(0)**	**Δc(0)**
Right Peak	22.28	0.21
Right Valley	17.87	0.12
Left Valley	-17.13	0.18
Left Peak	-21.40	0.15
Average	**19.67**	**0.09**

Table 6.1: Sound velocity of the four propagating features

to the position versus time data, and the error associated with each fit is the result of a χ-squared analysis run automatically in our curve fitting program, Igor.

As we discussed earlier, the peaks travel faster than the valleys. Further, it can be seen that in this experiment the right going features are traveling faster than the left going features. This is due to residual motion of the center of mass of the atomic cloud. By taking a simple average of speed at which the each feature is traveling we can eliminate one source of systematic error and extrapolate back to the infinitesimal perturbative case (see Chapter 5):

$$c(0) = \sum_{i=1}^{4} |c_i(0)|/4, \tag{6.1}$$

where $c_i(0)$ is the velocity associate with a particular feature (i.e. i = "Right Peak").

Each velocity of each feature is an independent measurement with its own associated error. When we propagate the error into the average velocity, $c(0)$ we must do so appropriately [87]. When a the quantity of interest is the result of several independent measurements then sometimes the error in one measurement will happen to cancel out some of the error in the other. On average, the error in our quantity of interest will be less than the sum of the errors in its parts.

A reasonable way to propagate errors is to treat them as "perpendicular" and combine them according to the pythagorean theorem. This idea can be used to derive

a general rule. Suppose there are two measurements, A and B, and the quantity of interest is C = f(A, B) for some function f. If A is perturbed by ΔA then C will be perturbed by the derivative of the function f with respect to A with B held constant, $\frac{\partial f}{\partial A}|_B \Delta A$. Similarly, the perturbation in C due to a perturbation in B is, $\frac{\partial f}{\partial B}|_A \Delta B$. And the total error will be the square root of the sum of the squares of each error as it impacts on the quantity of interest,

$$\Delta C = \sqrt{\left(\frac{\partial f}{\partial A}|_B \Delta A\right)^2 + \left(\frac{\partial f}{\partial B}|_A \Delta B\right)^2}. \tag{6.2}$$

For our measurement of the sound velocity we took the average of the sound speed of the four propagating features. The function used to combine our independent measurement is, $f(c_i) = \sum_{i=1}^{4} c_i/4$. and the partial derivative of the average with respect to its constituent parts is $\partial f(c_i)/\partial c_i = 1/4$. Therefore the total error in the average is,

$$\Delta c(0) = \sqrt{\sum_{i=1}^{4} \left(\Delta c_i(0)\right)^2}/4. \tag{6.3}$$

This is a simple example of how error may be propagated for independent measurement. In Section 6.4 I will show how this is done to produce the errors associated with our reported values of $c(0)/v_F$ and $1/(k_F a)$

6.2 Anharmonic correction

In our experiment, every effort was made to reduce the systematic errors in our measurement. We can use our knowledge of the exact experimental conditions in order to make corrections to the data. All of the theory discussed thus far has been for a harmonic trapping potential. Actually, the confining potential of the CO_2

beam is gaussian along the short (x- and y- direction) axis of the cigar shaped trap. This causes an anharmonic effect. In this section we will calculate an anharmonic correction factor to the speed of sound. At the end of this section, I will discuss how we apply the anharmonic correction factor to our data throughout the entire BEC-BCS crossover.

There is also a correction factor for the breathing mode frequency due to trap anharmonicity. This correction factor was worked out as part of the heat capacity measurement and is documented in Joe Kinast's Thesis, the actual breathing mode is,

$$\omega_{BM} = \omega_{BM\,Meas}\left(1 - \frac{16m\omega_\perp^2\langle x^2\rangle}{25V_0}\right)^{-1/2}, \tag{6.4}$$

where $\langle x^2\rangle$ is the mean square size of the trap, and V_0 is the amplitude of the trapping potential. So the correction factor $f_{BM} = \omega_{BM}/\omega_{BM\,Meas}$, is

$$f_{BM} = \left(1 - \frac{16m\omega_\perp^2\langle x^2\rangle}{25V_0}\right)^{-1/2}, \tag{6.5}$$

Recall that in Chapter 3 we used hydrodynamic equations to calculate the sound velocity in a trapped gas,

$$c = \left(\frac{1}{m}\frac{\int n_0\, d^2\rho}{\int \left(\partial\mu/\partial n|_{n=n_0}\right)^{-1} d^2\rho}\right)^{1/2}. \tag{6.6}$$

The above equation depends upon the equilibrium density as well as the derivative of the chemical potential with respect to density. In Chapter 2, both of these quantities were calculated for a gas trapped in a harmonic potential. The calculations

were done in the general case for a power law equation of state, equation (2.30),

$$\mu_L(\mathbf{r}) = \mathcal{C}n(\mathbf{r})^\gamma, \tag{6.7}$$

using the local density approximation equation (2.29),

$$\mu_G = \mu_L(\mathbf{r}) + V_{ext}(\mathbf{r}). \tag{6.8}$$

Further, in Section 2.1 I gave the trapping potential of cigar shaped dipole trap that provides harmonic confinement in the long axis (z-direction) of the trap and gaussian confinement in the short axis (x- and y-direction) of the trap,

$$V_{GA}(r,z) = V_0\left(1 - e^{-\frac{m\omega_x^2}{2V_0}x^2 - \frac{m\omega_y^2}{2V_0}y^2}\right) + \frac{1}{2}m\omega_z^2 z^2, \tag{6.9}$$

We need to determine a correction factor each time we performed a spatial integral in our previous calculations for a harmonic trap.

The speed of sound at the center of the trap (z = 0)for a power law equation of state when conditions for the LDA were met, equation (3.42) is,

$$c(0) = \sqrt{\frac{\gamma\mu_G}{m(1+\gamma)}}. \tag{6.10}$$

Therefore, the total anharmonic correction to the speed of sound will depend upon three parameters, the global chemical potential μ_G, the integral in the numerator $\int n_0 d^2\rho$, and the integral in the denominator $\int \left(\partial\mu/\partial n|_{n=n_0}\right)^{-1} d^2\rho$. The goal of this section is to develop a correction factor that we can apply to our measured value of the sound velocity and obtain the corresponding sound velocity in a harmonic trap

(i.e. $c(0) = f_{total}c(0)_{meas}$) First, we must develop the individual correction factors f_i that will be combined for a total correction,

$$f_{total} = \sqrt{f_{\mu_G}\frac{f_{numerator}}{f_{denominator}}}. \tag{6.11}$$

We have already worked out what the theoretical sound velocity should be for a gas trapped in a harmonic trapping potential at different interaction strengths Section 3.2. Now we will follow a similar procedure proscribed in that section, but substitute the gaussian trapping potential. In order to simplify the calculation we will start with a cylindrical coordinate system where $\rho^2 = x^2 + y^2$ and $\omega_x = \omega_y = \omega_\perp$.

Next, in order to determine the equilibrium density, we combine the LDA equation (2.29) and a power law equation of state equation (2.30). When we do this we discover that the equation for density of a gas trapped in the confining potential, $V_{GA}(r, z)$ is,

$$n_0(\rho, 0) = \left(\frac{\mu_G}{\mathcal{C}}\right)^{1/\gamma}\left(1 - \frac{V_0}{\mu_G}\left(1 - e^{-\frac{\rho^2}{2\rho_0^2}}\right) - \frac{z^2}{R_z^2}\right)^{1/\gamma} \tag{6.12}$$

where $\rho_0^2 = \frac{V_0}{m\omega_\perp^2}$. The other equilibrium quantity we need to know in order to calculate the sound velocity, is the derivative of the local chemical potential with respect to the density, $\left(\frac{\partial\mu_L}{\partial n}|_{n=n_0}\right)^{-1}$. Using a gaussian potential this is,

$$\left(\frac{\partial\mu_L}{\partial n}|_{n=n_0}\right)^{-1} = \frac{1}{\gamma\mathcal{C}}\left(\frac{\mu_G}{\mathcal{C}}\right)^{-\frac{\gamma}{(\gamma-1)}}\left(1 - \frac{V_0}{\mu}\left(1 - e^{-\frac{\rho^2}{2\rho_0^2}}\right) - \frac{z^2}{R_z^2}\right)^{-\frac{\gamma}{(\gamma-1)}}. \tag{6.13}$$

What follows in the next three subsections are calculations determining the correction factor f_{μ_G}, $f_{numerator}$, and$f_{denominator}$.

6.2.1 Correction to μ_G

Previously, we calculated μ_G by normalizing to the total atom number, (i.e. integrating the equilibrium density n_0 over all of space). We will do this again this time substituting in V_{GA} for our trapping potential and using the corresponding form of the density n_0. The object is to solve for μ_G in terms of experimental quantities. For the harmonic case we solve for μ_G for the interaction limits of our system. Namely in the ideal Fermi gas, strongly interacting Fermi gas, and a BEC limits. As the ideal Fermi gas and strongly interacting fermi gas equilibrium quantities only differ by a scale factor, there is no need to calculate the correction factor twice.

Therefore, starting with the strongly interacting (SI) case:

The equation for the total number of atoms N is,

$$N = \int n_0(\rho, z) dV. \tag{6.14}$$

Using the form of the equilibrium density for an gaussian potential we find

$$N = 2\pi \int_{\rho_{min}}^{\rho_{max}} \int_{z_{min}}^{z_{max}} \left(\frac{\mu_G}{(1+\beta)\frac{\hbar^2}{2m}(3\pi^2)^{2/3}} \right)^{3/2} \left(1 - \frac{V_0}{\mu_G} \left(1 - e^{-\frac{\rho^2}{2\rho_0^2}} \right) - \frac{z^2}{R_z^2} \right)^{3/2} \rho d\rho dz, \tag{6.15}$$

where $\rho_0^2 = \frac{V_0}{m\omega_\perp^2}$.

We will start with a change in variables that will simplify the integrals we need to solve. First, let $\xi \to \frac{\rho^2}{2\rho_0^2}$. Then $\rho d\rho = \rho_0^2 d\xi$, and we again let $z \to R_z z'$,

$$N = \left(\frac{\mu_G}{(1+\beta)\frac{\hbar^2}{2m}(3\pi^2)^{2/3}} \right)^{3/2} \rho_0^2 R_z 2\pi \int_{\xi_{min}}^{\xi_{max}} \int_{z'_{min}}^{z'_{max}} \left(1 - \frac{V_0}{\mu} \left(1 - e^{-\xi} \right) - z'^2 \right)^{3/2} d\xi dz'. \tag{6.16}$$

Further, the limits of integration will be determined from the equation $\left(1 - \frac{V_0}{\mu} \left(1 - e^{-\xi} \right) - z'^2 \right) =$

0. The solution to this equation provides the limits

$$z'_{max/min} = \pm\sqrt{1 - \frac{V_0}{\mu_G}\left(1 - e^{-\xi}\right)} \tag{6.17}$$

$$\xi_{max} = -\ln\left(1 - \frac{\mu_G}{V_0}\right) \tag{6.18}$$

$$\xi_{min} = 0. \tag{6.19}$$

After integrating in the z-direction we find

$$N = \frac{3\pi}{8} 2\pi\rho_0^2 R_z \left(\frac{\mu_G}{(1+\beta)\frac{\hbar^2}{2m}(3\pi^2)^{2/3}}\right)^{3/2} \int_0^{-\ln\left(1-\frac{\mu_G}{V_0}\right)} \left(1 - \frac{V_0}{\mu_G}\left(1 - e^{-\xi}\right)\right)^2 d\xi \tag{6.20}$$

Therefor the integral of interest then becomes

$$I_2 = \int_0^{-\ln\left(1-\frac{\mu_G}{V_0}\right)} \left(1 - \frac{V_0}{\mu_G}\left(1 - e^{-\xi}\right)\right)^2 \tag{6.21}$$

where the subscript '2' denotes exponent of the term $\left(1 - \frac{V_0}{\mu_G}\left(1 - e^{-\xi}\right)\right)$. We make this distinction as we will be coming back to similar integrals with the only difference being the power to which this term is raised.

A correction should be only a small fraction of the over all quantity. While equation (6.21) can be solved directly I will also give the results in the form of a Taylor Series expansion of $b = \frac{\mu_G}{V_0}$. Thus we can solve equation (6.21):

$$I_2(b) = \int_0^{-\ln(1-b)} \left(1 - \frac{1}{b}\left(1 - e^{-\xi}\right)\right)^2, \tag{6.22}$$

exactly,

$$I_2(b) = \frac{3}{2} - \frac{1}{b} - \left(\frac{1}{b} - 1\right)^2 \ln(1-b), \tag{6.23}$$

and in series form

$$I_2(b) = \frac{1}{3}b + \frac{1}{12}b^2 + \mathcal{O}\left(b^3\right). \tag{6.24}$$

Returning to the calculation for the total number of atoms we find that we have an equation for N in terms of trap quantities and the small parameter $b = \frac{\mu_G}{V_0}$. We can make the replacement $\rho_0^2 \rightarrow \frac{V_0}{m\omega_\perp^2} \rightarrow \frac{1}{2b}R_\perp^2$,

$$N = \frac{3\pi}{8}2\pi\frac{1}{b}R_\perp^2 R_z \left(\frac{\mu_G}{(1+\beta)\frac{\hbar^2}{2m}(3\pi^2)^{2/3}}\right)^{3/2} I_2(b). \tag{6.25}$$

After some algebra we can eventually solve for μ_G for a strongly interacting Fermi gas in a gaussian trap. It is useful to use a form that reflects the solution for μ_G for a 3-dimensional harmonic trap multiplied by an anharmonic correction. In this form μ_G is,

$$\mu_G = (1+\beta)^{1/2} E_F \left(\frac{I_2(b)}{b/3}\right)^{-1/3}. \tag{6.26}$$

and the correction is

$$f_{\mu_G} = \left(\frac{I_2(b)}{b/3}\right)^{-1/3}. \tag{6.27}$$

Now we will determine the effect of anharmonicity on the calculation for the global chemical potential in the BEC limit. Again, we must determine μ_G by integrating over the equilibrium density n_0 in all three spatial directions. The anharmonic correction to μ_G, f_{μ_G}, for a BEC is calculated in the same manner as above.

The equation for the total number of atoms N in a BEC trapped in a gaussian potential is,

$$N = 2\pi \int_{\rho_{min}}^{\rho_{max}} \int_{z_{min}}^{z_{max}} \frac{\mu_G}{\pi\hbar^2\frac{a_{mol}}{2m}} \left(1 - \frac{V_0}{\mu_G}\left(1 - e^{-\frac{\rho^2}{2\rho_0^2}}\right) - \frac{z^2}{R_z^2}\right) \rho d\rho dz. \tag{6.28}$$

We perform the same change in variables as before, $\xi \rightarrow \frac{\rho^2}{2\rho_0^2}$ and $z \rightarrow R_z z'$, and find

$$N = \frac{\mu_G}{\pi\hbar^2 \frac{a_{mol}}{2m}} \rho_0^2 R_z 2\pi \int_{\xi_{min}}^{\xi_{max}} \int_{z'_{min}}^{z'_{max}} \left(1 - \frac{V_0}{\mu}\left(1 - e^{-\xi}\right) - z'^2\right) d\xi dz'. \tag{6.29}$$

The limits of integration will also be the same, equation (6.17).

After integrating in the z-direction we find

$$N = \frac{4\pi}{3} \frac{\mu_G}{\pi\hbar^2 \frac{a_{mol}}{2m}} \rho_0^2 R_z \int_0^{-\ln\left(1-\frac{\mu_G}{V_0}\right)} \left(1 - \frac{V_0}{\mu_G}\left(1 - e^{-\xi}\right)\right)^{3/2} d\xi \tag{6.30}$$

Therefor the integral of interest then becomes,

$$I_{3/2} = \int_0^{-\ln\left(1-\frac{\mu_G}{V_0}\right)} \left(1 - \frac{V_0}{\mu_G}\left(1 - e^{-\xi}\right)\right)^{3/2}. \tag{6.31}$$

This integral can be solved exactly,

$$I_{3/2}(b) = \frac{8}{3} - \frac{2}{b} - \frac{2(1-b)^2\left(\frac{\pi}{2} - \arcsin\sqrt{1-b}\right)}{b\sqrt{b(1-b)}}, \tag{6.32}$$

and the Taylor series form,

$$I_{3/2}(b) = \frac{2}{5}b + \frac{4}{34}b^2 + \mathcal{O}\left(b^3\right). \tag{6.33}$$

Returning to the calculation for the total number of atoms we find that we have an equation for N in terms of trap quantities and the small parameter $b = \frac{\mu_G}{V_0}$. We can make the replacement $\rho_0^2 \rightarrow \frac{V_0}{m\omega_\perp^2} \rightarrow \frac{1}{2b}R_\perp^2$

$$N = \frac{4\pi}{3}\frac{\mu_G}{\pi\hbar^2\frac{a_{mol}}{2m}}\frac{1}{2b}R_\perp^2 R_z I_{3/2}(b) \tag{6.34}$$

After some algebra we can eventually solve for μ_G for a Bose gas in an anharmonic trap. It is useful to use a form that reflects the solution for μ_G for a 3-dimensional harmonic trap multiplied by an anharmonic correction. In this form μ_G is,

$$\mu_G = \frac{1}{4}E_F\left(\frac{5}{2}k_F a_{mol}\right)^{2/5}\left(\frac{I_{3/2}(b)}{2b/5}\right)^{-2/5}, \tag{6.35}$$

and the correction factor is,

$$f_{\mu_G} = \left(\frac{I_{3/2}(b)}{2b/5}\right)^{-2/5}. \tag{6.36}$$

6.2.2 Anharmonic correction to the numerator

The rest of the anharmonic correction is divided into two parts. When we calculated the sound velocity in a harmonic trap we calculated two integrals for the equilibrium quantities $\int n_0 d^2\rho$ and $\int \left(\frac{\partial\mu_L}{\partial n}|_{n=n_0}\right)^{-1} d^2\rho$ which appeared in the numerator and the denominator of the equation for sound velocity respectively. In order to calculate the anharmonic correction we must again perform these integrals, but we will use the use the gaussian form of the equilibrium quantities. Other than this, the method is the same as the 3-dimensional harmonic case. For simplicity we will set $z = 0$ as we are only interested in the velocity at the center of the trap. The integral of the density over the radial direction in its general form is,

$$\int n_0 d^2\rho = 2\pi\int\left(\frac{\mu_G}{\mathcal{C}}\right)^{1/\gamma}\left(1 - \frac{V_0}{\mu_G}\left(1 - e^{-\frac{\rho^2}{2\rho_0^2}}\right)\right)^{1/\gamma}\rho d\rho \tag{6.37}$$

Once we introduce our small quantity $b = \frac{V_0}{\mu_G}$, make the substitutions $\xi \to \frac{\rho^2}{2\rho_0^2}$ and $\rho_0^2 \to \frac{V_0}{m\omega_\perp^2} \to \frac{1}{2b}R_\perp^2$, and use the previously defined limits of integration, we find this equation becomes

$$\int n_0 d^2\rho = 2\pi \left(\frac{\mu_G}{\mathcal{C}}\right)^{1/\gamma} R_\perp^2 \frac{1}{2b} \int_0^{-\ln(1-b)} \left(1 - b\left(1 - e^{-\xi}\right)\right)^{1/\gamma} d\xi. \tag{6.38}$$

This differs from the 3-dimensional gas result for the numerator by the quantity

$$f_{numerator} = \frac{1}{b}\frac{(1+\gamma)}{\gamma} I_{1/\gamma}. \tag{6.39}$$

For the unitary gas, $\gamma = 2/3$. This means

$$f_{numerator} = \frac{1}{b}\frac{5}{2} I_{3/2}. \tag{6.40}$$

The integral of interest here is,

$$I_{3/2}(b) = \int_0^{-\ln(1-b)} \left(1 - \frac{1}{b}\left(1 - e^{-\xi}\right)\right)^{3/2}. \tag{6.41}$$

We can find the exact solution,

$$I_{3/2}(b) = \frac{8}{3} - \frac{2}{b} - \frac{2(1-b)^2\left(\frac{\pi}{2} - \arcsin\sqrt{1-b}\right)}{b\sqrt{b(1-b)}}. \tag{6.42}$$

and the Taylor series form,

$$I_{3/2}(b) = \frac{2}{5}b + \frac{4}{34}b^2 + \mathcal{O}\left(b^3\right). \tag{6.43}$$

In the BEC limit $\gamma = 1$. This means

$$f_{numerator} = \frac{2}{b} I_1. \tag{6.44}$$

Here the integral of interest is,

$$I_1(b) = \int_0^{-\ln(1-b)} \left(1 - \frac{1}{b}\left(1 - e^{-\xi}\right)\right). \tag{6.45}$$

We can find the exact solution

$$I_1(b) = 1 - (1 - \frac{1}{b})\ln(1-b) \tag{6.46}$$

and the Taylor Series expansion

$$I_1(b) = \frac{1}{2}b + \frac{1}{6}b^2 + \mathcal{O}\left(b^3\right). \tag{6.47}$$

6.2.3 Anharmonic correction to the denominator

Further, for a gaussian potential the general form of the denominator is

$$\int \left(\frac{\partial \mu_L}{\partial n}|_{n=n_0}\right)^{-1} d^2\rho = 2\pi \int \frac{1}{\gamma \mathcal{C}} \left(\frac{\mu_G}{\mathcal{C}}\right)^{-\frac{\gamma}{(\gamma-1)}} \left(1 - \frac{V_0}{\mu}\left(1 - e^{-\frac{\rho^2}{2\rho_0^2}}\right) - \frac{z^2}{R_z}\right)^{-\frac{\gamma}{(\gamma-1)}}. \tag{6.48}$$

Once we introduce our small quantity $b = \frac{V_0}{\mu_G}$ and make the substitutions $\xi \to \frac{\rho^2}{2\rho_0^2}$ and $\rho_0^2 \to \frac{V_0}{m\omega_\perp^2} \to \frac{1}{2b}R_\perp^2$ and use the limits as previously defined we find the equation

becomes

$$\int \left(\frac{\partial \mu_L}{\partial n}|_{n=n_0}\right)^{-1} d^2\rho = 2\pi \left(\frac{\mu_G}{\mathcal{C}}\right)^{-\frac{\gamma}{(\gamma-1)}} \frac{1}{2b} R_\perp^2 \int_0^{-\ln(1-b)} \left(1-b\left(1-e^{-\xi}\right)\right)^{-\frac{\gamma}{(\gamma-1)}} d\xi. \tag{6.49}$$

This differs from 3-dimensional gas result for the numerator, equation (3.36) by the quantity

$$f_{denominator} = \frac{1}{b}\frac{1}{\gamma} I_{\frac{(\gamma-1)}{\gamma}}. \tag{6.50}$$

For the unitary gas, $\gamma = 2/3$. This means

$$f_{denominator} = \frac{1}{b}\frac{1}{2} I_{1/2}. \tag{6.51}$$

For this integral

$$I_{1/2}(b) = \int_0^{-\ln(1-b)} \left(1-\frac{1}{b}\left(1-e^{-\xi}\right)\right)^{1/2} \tag{6.52}$$

we can find the exact solution,

$$I_{1/2}(b) = 2 - 2\sqrt{\frac{1}{b}-1}\arcsin\sqrt{b} \tag{6.53}$$

and the Taylor series form

$$I_{1/2}(b) = \frac{2}{3}b + \frac{4}{15}b^2 + \mathcal{O}\left(b^3\right). \tag{6.54}$$

In the BEC limit, $\gamma = 1$. This means

$$f_{denominator} = \frac{1}{b} I_0. \tag{6.55}$$

For this integral

$$I_0(b) = -\ln(1-b)\int_0^{-\ln(1-b)} \left(1 - \frac{1}{b}\left(1 - e^{-\xi}\right)\right) \tag{6.56}$$

we can find the exact solution,

$$I_0(b) = -\ln(1-b), \tag{6.57}$$

or the Taylor Series expansion,

$$I_0(b) = b + \frac{1}{2}b^2 + \mathcal{O}\left(b^3\right). \tag{6.58}$$

6.2.4 Anharmonic correction in the BEC-BCS crossover

Combining the correction to μ_G, the numerator, and the denominator from equations (6.27), (6.40), and (6.51), we can solve for the speed of sound in a strongly interacting gas at zero temperature in a gaussian trap,

$$f_{SI} = \sqrt{\left(\frac{I_2(b)}{b/3}\right)^{-1/3} \frac{\frac{I_{3/2}(b)}{2b/5}}{\frac{I_{1/2}(b)}{2b/3}}}, \tag{6.59}$$

or in Taylor series form

$$f_{SI} = \left(1 - \frac{83}{840}b + \frac{17771}{470400}b^2 + \mathcal{O}\left(b^3\right)\right). \tag{6.60}$$

Combining the correction to μ_G, the numerator, and the denominator from equations (6.36), (6.44), and (6.55), we can solve for the anharmonic correction to the

speed of sound in a BEC,

$$f_{BEC} = \sqrt{\left(\frac{I_{3/2}(b)}{2b/5}\right)^{-2/5 \ \frac{\frac{I_1(b)}{b/2}}{\frac{I_0(b)}{b}}}}, \tag{6.61}$$

or in a Taylor Series expansion

$$f_{BEC} = \left(1 - \frac{59}{420}b + \frac{6583}{117600}b^2 + \mathcal{O}\left(b^3\right)\right). \tag{6.62}$$

For some positive values of $1/(k_F a)$ the gas is neither a strongly interacting Fermi gas nor a BEC, but something in between. In general we consider a gas to be in the BEC range when $1/(k_F a) \geq 1$ and a gas is strongly interacting when $1/(k_F a) = 0$ when $1/(k_F a) < 0$ the gas is moving from the unitary regime to the weakly interacting regime and the unitary correction holds. In the in between can we take a linear combination of the two correction factors f_{SI} and f_{BEC}.

$$\frac{1}{k_F a} \leq 0 \quad : \quad f = f_{Unitary} \tag{6.63}$$

$$0 < \frac{1}{k_F a} < 1 \quad : \quad f = (1 - \frac{1}{k_F a}) f_{Unitary} + \frac{1}{k_F a} f_{BEC} \tag{6.64}$$

$$\frac{1}{k_F a} \geq 1 \quad : \quad f = f_{BEC} \tag{6.65}$$

Above, we calculated what the sound velocity would be for a unitary gas and a BEC in an gaussian trap. The data we would like to present would be the simplest case for theorists to work with. Therefore we will correct for the anharmonicity of the trap and report the sound velocity for harmonic trap.

6.3 Correction to atom number N

Precise determination of the atom number is important in our measurements of sound. In previous experiments it was normal to see about a 15% variation in the number of atoms measured for a set of repeated experiments. As the Fermi velocity $v_F \propto N^{(1/6)}$ this results in a 2.5% uncertainty in v_F due to atom measurement alone. In order to increase the accuracy of this measurement it is necessary to take a close look as to how atom number varies. There are several factors that can cause variation in the measured atom number. By closely examining these factors we can decouple variations due actual number variation from systematic effects. The three main sources of variation in the measured atom number are:

- Variation in the number of the actual number of atoms loaded into the trap
- Instability in the frequency of the laser light used to image the atoms
- Instability in the magnetic field at which the atoms are imaged

It is the first item on the list that we wish to report. It will be the goal of this section to decouple this information from the data.

6.3.1 Probability distributions

In order to determine the actual atom number (N) from the measured atom number (N_{Meas}) we will need to arrange our data into probability distributions and employ a few statistical techniques. A probability distribution $p_i(x)$ provides the probability of a measured value x. We can characterize any distribution with a mean $\langle x \rangle$ and a standard deviation σ_x,

$$\langle x \rangle = \int x p_i(x) dx \tag{6.66}$$

$$\sigma_x = \sqrt{\int \left(\langle x \rangle - x\right)^2 p_i(x) dx} \tag{6.67}$$

In order to obtain a probability distribution for the measured atom number we require a large set of measurements. In a single day we conducted 330 measurements of the atom number. Figure 6.1 shows the probability distribution $P_{Meas}(N_{Meas}/\langle N_{Meas} \rangle)$ for the measured atom number. In order to obtain P_{Meas} each atom number is first normalized to the mean measured atom number and then divided into bins. For example, if 10 trials resulted in an atom number between 55% and 65% of the mean then $P_{Meas}(0.6) = 10$. The distribution is then normalized such that $\int P_{Meas}(x)dx = 1$. Therefore, each point on the probability distribution represents the probability of measuring the atom number at a particular fraction of the mean measured atom number.

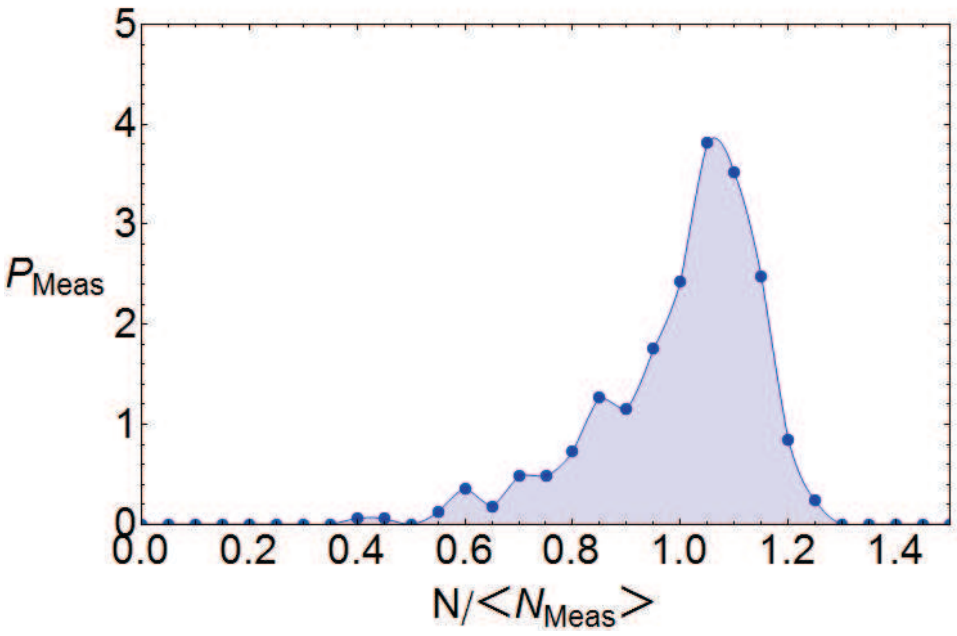

Figure 6.1: 330 atom number measurement divided by the average number of atoms and normalized to form a probability distribution of the measured atom number.

For the measured atom number the mean is $\langle N_{Meas} \rangle$ and $\sigma_{Meas} = 0.13 \langle N_{Meas} \rangle$. As in any measurement some of the values for atom number are greater than the mean and some are less than the mean. Note the shape of P_{Meas}. The distribution is not symmetric, it has a long tail for lower atom numbers. If the variation in atom number was only due to a random event like loading atoms into a trap we would expect a symmetric distribution. Therefore there must be other contributing factors.

If there are two contributing factors to a probability distribution, the combined probability distribution can be obtained by taking the convolution of the contributing probability distributions. For example, if there are two ways in which atom number can vary, each with respective probability distributions $f(x)$ and $g(x)$ then the combined probability distribution is,

$$p(x) = \int_{\infty}^{\infty} f(k) g(x-k) dk. \tag{6.68}$$

P_{Meas} is a combined probability distribution. We will employ equation (6.68) obtain the actual probability distribution P_{Atoms}. Through this analysis we will determine the correction factor for bias in the mean atom number $\langle N \rangle$ and atom standard deviation σ_N in order to determine the true atom number and its associated error,

$$\langle N \rangle = f_N \langle N_{Meas} \rangle \tag{6.69}$$

$$\sigma_N = f_\sigma \sigma_N. \tag{6.70}$$

where f_N is the correction factor for atom number and $f_{\Delta N}$ is the correction factor for atom number standard deviation.

6.3.2 Variation in atom number

Our goal is to extract the probability distribution of the actual atom number P_{Atoms}, from the probability distribution of the measured atom number, P_{Meas}. We can assume a normal distribution for the actual number of atoms,

$$P_{Atoms}(N/\langle N\rangle) = \frac{1}{\sqrt{2\pi}\sigma_{Atoms}} \exp\left[-\frac{(N/\langle N\rangle - 1)^2}{2\sigma_{Atoms}^2}\right]. \tag{6.71}$$

Here $\langle N\rangle$ is the mean value for this probability distribution and the atom number standard deviation σ_{Atoms} are is in units of $\langle N\rangle$. Figure 6.2 shows the actual atom probability distribution with an assumed value of σ_{Atoms}.

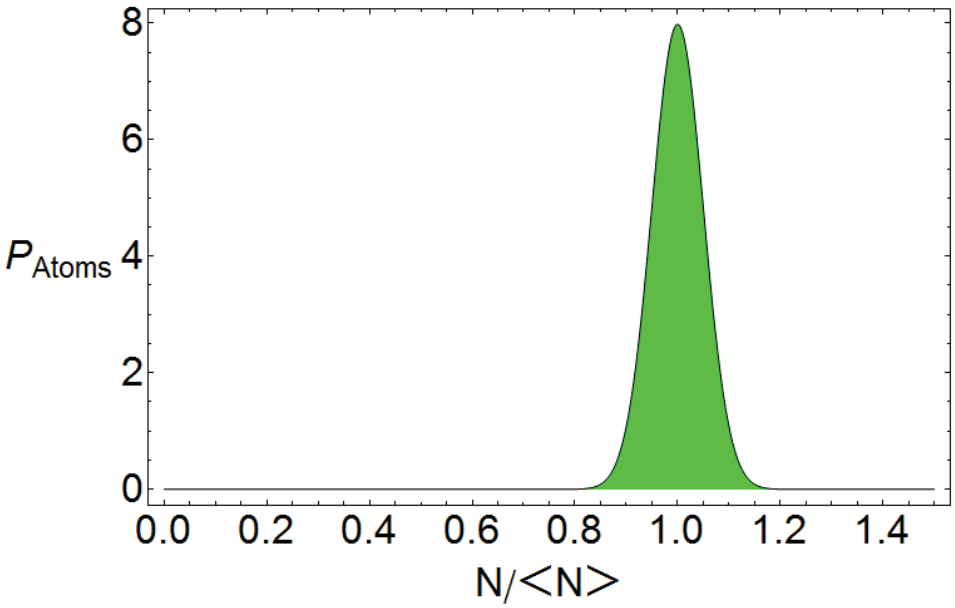

Figure 6.2: The probability distribution of the actual number can be characterized by a normal or gaussian distribution. This distribution is symmetric as we only expect random factors to effect the atom number variation.

What we now need to determine is the probability distribution due to alternate sources of atom number variation. Consider the variation in the frequency of the laser

light used to image the atoms and the variation in the magnetic field at which the atoms are imaged. Both factors influence the detuning from the atomic transition when the atoms are imaged. Detuning always reduces the value of the measured number of atoms. We define ω as the frequency of the laser light, and ω_0 as the atomic transition frequency, which depends on the magnetic field. The detuning is then,

$$\delta = \omega - \omega_0 \tag{6.72}$$

When we measure the laser frequency jitter associated with ω we find that the 95% confidence interval is 3 MHz. We can determine our magnetic field to 1 Gauss at a 95% confidence interval. The atom transition frequency, ω_0 depends on the magnetic field at about 2.8 MHz per Gauss. This means that our 95% confidence interval for ω_0 is 2.8 MHz. We assume that the probability distributions for the variations in laser frequency ω and atomic resonance frequency ω_0 are normal distributions.

We know from equation (6.68) that the convolution of two distributions gives a combined distribution. The convolution of two gaussian distributions gives a third gaussian distribution whose width is the square root of the sum of the squares of the original two widths. Therefore, the probability distribution of the detuning is normal with a 95% confidence interval of $\sqrt{(2.8\,MHz)^2 + (3\,MHz)^2} = 4.1 MHz$.

We try our best to match the laser frequency to the atomic resonance frequency so the mean of the detuning probability will be zero. In statistics, the 95% confidence comprises four standard deviations in a normal distribution. Therefore, the probability distribution has a standard deviation of 1.03 MHz.

We still need to relate the variation in frequency to our atom number measurement. When we determined the density distribution from our absorption images in Section

5.5, we found from equation (5.21), that the measured atom number varies as a Lorentzian with respect to frequency due to the variation in the absolute cross section with respect to detuning.

$$\frac{N}{\langle N\rangle} \propto \frac{1}{1+\left(\frac{\delta}{\Gamma_S/2}\right)^2}, \tag{6.73}$$

where $\Gamma_S = 5.9\,MHz$ is the 1/2-linewidth of the transition. It is clear from equation (6.73) that any non-zero value for δ will result in a decrease of the measured atom number.

Using Mathematica, I generated a random set of 10^5 frequency detunings centered at 0 MHz using normal probability distribution with a standard deviation of $\sigma = 1.03\,MHz$. I then determined $N/\langle N\rangle$ from equation (6.73) as a function of each of these detuning values resulting in a set of 10^5 values of $N/\langle N\rangle$. This set was binned from 0 to 1 with a bin width of .025. This binned distribution was then normalized. The result was a probability distribution $P_\delta(N/\langle N\rangle)$ for the atom number with variation due solely to variation in the detuning. Meaning that for a trap that is consistently loaded with the exact same number of atoms $\langle N\rangle$, we might expect the distribution in our atom number measurement to look like P_δ (see Figure 6.3).

We have determined probability distribution due to detuning $P_\delta(N/\langle N\rangle)$ and measured atom number $P_{Meas}(N/\langle N_{Meas}\rangle)$. Moreover we know the form of the actual atom number probability distribution $P_{Atoms}(N/\langle N\rangle)$. There is one more factor to consider. In $P_{Meas}(N/\langle N_{Meas}\rangle)$ the atom number is normalized to the mean measured atom number $\langle N_{Meas}\rangle$ while in our other two probability distributions the atom number is in units of the actual atom number $\langle N\rangle$. We need to make our probability distributions consistent. In order to do this we must determine $\langle N_{Meas}\rangle$ as a function of $\langle N\rangle$. Fortunately, we have already defined our correction factor $f_N = \langle N\rangle/\langle N_{Meas}\rangle$.

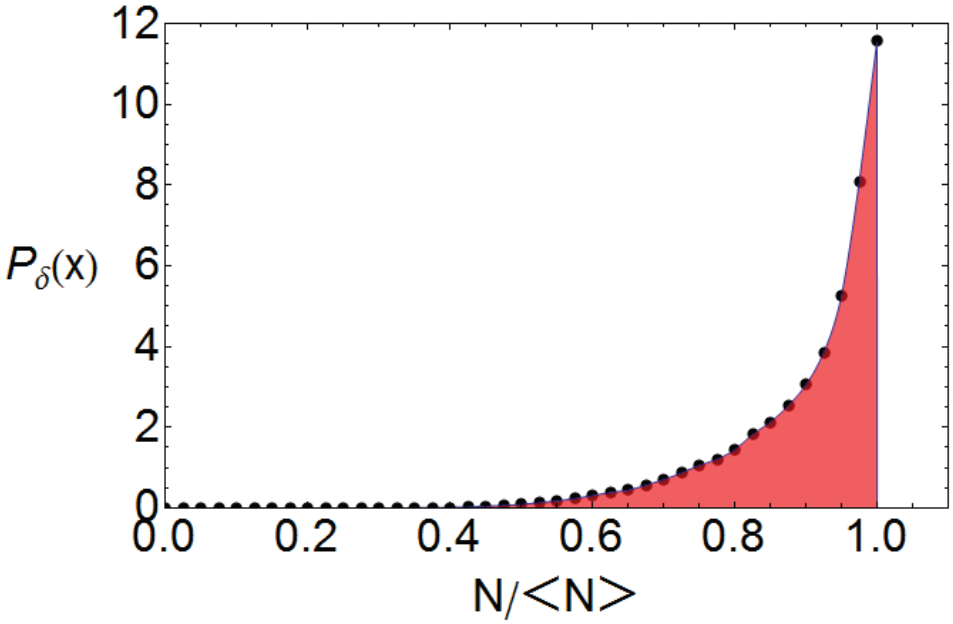

Figure 6.3: The atom number can only decrease as a result of detuning. Using numerical simulation and a constant actual atom number this probability distribution reflects the variation in measured atom number due to frequency detuning, δ

We need to insure that the probability distribution still normalizes to one. This is accomplished by taking the product of P_{Meas} and f_N,

$$P_{Meas}(N/\langle N_{Meas}\rangle) \rightarrow P_{Meas}(N/\langle N_{Meas}\rangle f_N) f_N. \tag{6.74}$$

Now all of our probability distributions are consistent. The probability distributions for the measured atom number $P_{Meas}(N/\langle N_{Meas} f_N\rangle) f_N$ is the convolution probability distribution of the actual atom number $P_{Atoms}(N/\langle N\rangle)$ and the probability distribution of atom number due to frequency detuning $P_\delta(N/\langle N\rangle)$.

$$P_{Meas}(x) f_N = \int_\infty^\infty P_{Atoms}(k) P_\delta(x-k) dk, \tag{6.75}$$

where $x = N/\langle N\rangle$.

In Mathematica I perform a 2-parameter χ-squared fit between the measured atom number probability distribution and equation (6.75). First, I select a value for σ_{Atoms} and then perform the integral on the right hand side of equation (6.75). Next, I fit the resulting curve to our measured atom probability distribution by varying f_{Atoms} until I minimized the square of the difference between the calculated curve and the measured distribution. I repeat this process for several values of σ_{Atoms} and report the values of σ_{Atoms} and f_N that minimize the square of the difference signal.

Figure 6.4 shows equation (6.75) and $P_{Meas}(x/f_N) f_N$ with values of f_N and σ_{Atoms} that minimize the chi-squared fit. I found that these values were $\sigma_N = 0.0542$ and $f_N = 1.12$. This means that our measured mean atom number was only 88.6% of the actual atom number, and our measured atom standard deviation over twice as much as the actual atom standard deviation. We can compute $f_{\Delta N} = 5\%/13\% = 0.38$.

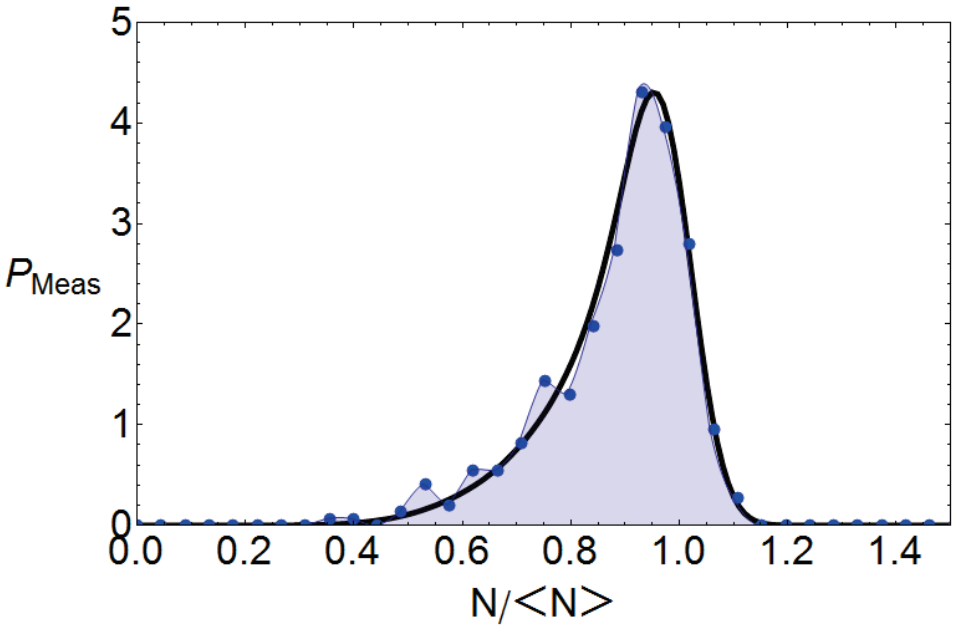

Figure 6.4: The probability distribution for the measured atom number (blue dots) is fit with the convolution of the probability distribution of the actual atom number and the probability distribution resulting from variation in measured atom number due to detuning (black curve).

With these correction factors we can compute the actual atom number,

$$N_{Atoms} = 1.13 N_{Meas} \tag{6.76}$$

and the actual atom number standard deviation

$$\Delta N_{Atoms} = 0.38 \Delta N_{Meas}. \tag{6.77}$$

6.4 c(0) in units of v_F versus $1/(k_F a)$ and their associated errors

We now have everything need to compute or reported values of $c(0)/v_F$ and $1/(k_F a)$.

The anharmonic corrections to sound was found for the strongly interacting Fermi gas f_{SI} and in weakly interacting BEC f_{BEC},

$$f_{SI} = 1 - \frac{83}{840}\frac{\mu_G}{V_0} + \frac{17771}{470400}\left(\frac{\mu_G}{V_0}|\right)^2 + \mathcal{O}\left(\frac{\mu_G}{V_0}^3\right), \tag{6.78}$$

and

$$f_{BEC} = 1 - \frac{59}{420}\frac{\mu_G}{V_0} + \frac{6583}{117600}\left(\frac{\mu_G}{V_0}\right)^2 + \mathcal{O}\left(\frac{\mu_G}{V_0}^3\right). \tag{6.79}$$

where μ_G is the global chemical potential and V_0 is the amplitude of the trapping potential.

For all negative values of the gas we can use the f_{SI} correction. For some positive values of $1/(k_F a)$ the gas is neither a strongly interacting Fermi gas nor a weakly interacting BEC, but something in between. In general we consider a gas to be in the weakly interacting BEC regime when $1/(k_F a) \geq 1$ and a gas is strongly interacting

when $1/(k_F a) = 0$. When $1/(k_F a) < 0$ the gas is moving from the unitary regime to the weakly interacting BCS regime and the unitary correction holds. $0 < 1/(k_F a) < 1$ we take a linear combination of the two correction factors f_{SI} and f_{BEC}. The corrected sound velocity is then,

$$\frac{1}{k_F a} \leq 0 \quad : \quad c(0) = c_{meas}(0) f_{Unitary} \tag{6.80}$$

$$0 < \frac{1}{k_F a} < 1 \quad : \quad c(0) = c_{meas}(0)(1 - \frac{1}{k_F a}) f_{Unitary} + \frac{1}{k_F a} f_{BEC} \tag{6.81}$$

$$\frac{1}{k_F a} \geq 1 \quad : \quad c(0) = c_{meas}(0) f_{BEC} \tag{6.82}$$

Concurrent with each sound velocity experiment we run a breathing mode experiment. We measure the radial (x- and y- direction) breathing frequency, ω_{BM}. The anharmonically corrected breathing mode is

$$\omega_{BM} = f_{BM} \omega_{BM\ Meas}. \tag{6.83}$$

The breathing mode frequency, one half the parametric frequencies, and the slosh frequency are all used to calculate the average trap frequency $\overline{\omega}$ The equation for the average trap frequency is,

$$\overline{\omega} = \left(\frac{3}{10} \omega_{BM}^2 \sqrt{\frac{3}{10} (\lambda_z \omega_{BM})^2 + \omega_{zMag}(B)^2} \right)^{1/3}, \tag{6.84}$$

where $\lambda_z = \omega_z / \sqrt{\omega_x \omega_y}$ is the ratio of axial trap frequency to the geometric mean of the radial trap frequencies, and ω_{zMag} is the magnetic field slosh frequency. The total

error, $\Delta\overline{\omega}$, associated with the average trap frequency is,

$$\Delta\overline{\omega} = \sqrt{\sum_i \left(\frac{\partial\overline{\omega}}{\partial x_i}\Delta x_i\right)^2}, \tag{6.85}$$

Lets start with the error associated with λ_z. For each term in λ_z ($\omega_{x,y,z}$)we can compute the error contribution,

$$\frac{\partial\lambda_z}{\partial\omega_i}\frac{\Delta\omega_i}{\lambda_z} = \frac{\Delta\omega_i}{2\omega_i} \tag{6.86}$$

The total fractional error associated with λ_z is the square root of the sum of the squares of the individual contributions,

$$\frac{\Delta\lambda_z}{\lambda_z} = \sqrt{\left(\frac{\Delta\omega_x}{2\omega_x}\right)^2 + \left(\frac{\Delta\omega_y}{2\omega_y}\right)^2 + \left(\frac{\Delta\omega_z}{2\omega_z}\right)^2}. \tag{6.87}$$

The fractional error contributions from each term in $\overline{\omega}$ are,

$$\frac{\partial\overline{\omega}}{\partial\omega_{BM}}\frac{\Delta\omega_{BM}}{\overline{\omega}} = \frac{1}{3}\left(\frac{2}{\omega_{BM}} + \frac{\frac{3}{10}\lambda_z^2\omega_{BM}}{\frac{3}{10}\lambda_z^2\omega_{BM}^2 + \omega_{zMag}^2}\right)\Delta\omega_{BM} \tag{6.88}$$

$$\frac{\partial\overline{\omega}}{\partial\lambda_z}\frac{\Delta\lambda_z}{\overline{\omega}} = \frac{1}{10}\frac{\lambda_z\omega_{BM}^2}{\frac{3}{10}\lambda_z^2\omega_{BM}^2 + \omega_{zMag}^2}\Delta\lambda_z \tag{6.89}$$

$$\frac{\partial\overline{\omega}}{\partial\omega_{zMag}}\frac{\Delta\omega_{zMag}}{\overline{\omega}} = \frac{1}{3}\frac{\omega_{zMag}}{\frac{3}{10}\lambda_z^2\omega_{BM}^2 + \omega_{zMag}^2}\Delta\omega_{zMag}. \tag{6.90}$$

Therefore

$$\frac{\Delta\overline{\omega}}{\overline{\omega}} = \frac{1}{\overline{\omega}}\sqrt{\left(\frac{\partial\overline{\omega}}{\partial\omega_{BM}}\Delta\omega_{BM}\right)^2 + \left(\frac{\partial\overline{\omega}}{\partial\lambda_z}\Delta\lambda_z\right)^2 + \left(\frac{\partial\overline{\omega}}{\partial\omega_{zMag}}\Delta\omega_{zMag}\right)^2} \tag{6.91}$$

The sources of error is the average trap frequency are $\Delta\omega_{BM}$, $\Delta\lambda_z$, $\Delta\omega_{zMag}$. Of these

$\Delta\omega_{zMag}$ is consistently small and has no significant contribution to the overall error in $\overline{\omega}$.

In our paper on sound velocity we discounted the contribution of $\Delta\lambda_z$ and approximated the total error in the average trap frequency as, $\Delta\overline{\omega} \approx \frac{\Delta\omega_{BM}}{\omega_{BM}}\overline{\omega}$.

The final measurement we make is in Atom Number. In the previous section we developed a correction to atom number that corrects both the mean value as well as the error.

$$N = f_N N_{Meas} \tag{6.92}$$

$$\Delta N = f_{\Delta N}\Delta N_{Meas}. \tag{6.93}$$

where $f_N = 1.13$ and $f_{\Delta N} = 0.38$.

The average trap frequency and atom number are both used to determine the Fermi Energy, $E_F = \hbar\overline{\omega}(3N)^{1/3}$. The total error in the Fermi energy can be calculated from its constituents contributions,

$$\Delta E_F = E_F\sqrt{\left(\frac{\Delta\overline{\omega}}{\omega}\right)^2 + \left(\frac{\Delta N}{3N}\right)^2}. \tag{6.94}$$

From the total error in the Fermi energy we can determine total error in the Fermi velocity, $v_F = \sqrt{2E_F/m}$,

$$\Delta v_F = v_F\frac{1}{2}\frac{\Delta E_F}{E_F} \tag{6.95}$$

and the Fermi wave number, $\hbar k_F = \sqrt{2E_F m}$,

$$\Delta k_F = k_F\frac{1}{2}\frac{\Delta E_F}{E_F}. \tag{6.96}$$

The total error in our reported value of $c(0)/v_F$ can be calculated from its constituents

contributions,

$$\Delta\frac{c(0)}{v_F} = \frac{c(0)}{v_F}\sqrt{\left(\frac{\Delta c(0)}{c(0)}\right)^2 + \left(\frac{\Delta v_F}{v_F}\right)^2}. \tag{6.97}$$

Finally the total error in our reported value of $1/(k_F a)$ is simply,

$$\Delta\frac{1}{k_F a} = \frac{1}{k_F a}\frac{\Delta k_F}{kF}. \tag{6.98}$$

Chapter 7

Sound velocity results

We measured the sound velocity in an ultra-cold Fermi Gas comprised of the lowest two hyperfine states of ^{6}Li across a broad range of interaction strengths. In doing so we are able to test hydrodynamic models of sound propagation and predictions characterizing the equation of state of this gas.

First, I will compare the equations based upon plane wave propagation with those obtained from isotropic sound propagation. Next, I will introduce the dimensionless parameter $1/(k_F a)$, and explain why we characterize the various regions of interest near the Feshbach resonance by this parameter. Lastly, I will examine the data acquired across the whole BEC-BCS crossover and assess what we can learn from the data. Our sound velocity data are compared to the simple mean field model developed in Section 3.3.2, the zero temperature theory at the limits near a Feshbach resonance, and many-body models predicting a continuous equation of state in the BEC-BCS crossover. Focus will be placed on the BCS, Unitary, and BEC regimes individually as well as the crossover region in general.

7.1 Isotropic versus plane wave propagation

In previous chapters we discussed the theory behind the propagation of sound in a trapped gas. One thing that has been left out, however, is a review of isotropic sound propagation. Isotropic sound propagation assumes a gas in equilibrium and evaluates the speed of sound in terms of the density,

$$c_I(n) = \sqrt{n\frac{\partial \mu_L}{\partial n}/m}. \tag{7.1}$$

In the general case for a power law equation of state, $\mu_L = \mathcal{C}n^\gamma$ so the isotropic sound velocity is,

$$c_I(n) = \sqrt{\gamma \mathcal{C} n^\gamma / m}. \tag{7.2}$$

Using the local density approximation where the global chemical potential is $\mu_G = \mu_L + V_{Ext}$ we can get the position dependent isotropic sound for a gas trapped in a harmonic potential,

$$c_I(x,y,z) = \sqrt{\frac{\gamma \mu_G}{m}}\left(1 - \frac{x^2}{R_x^2} - \frac{y^2}{R_y^2} - \frac{z^2}{R_z^2}\right)^{1/2}. \tag{7.3}$$

When we take the line of sight average (i.e. the velocity averaged in the direction of propagation of the camera beam) we find,

$$\langle c_I(y,z)\rangle = \frac{\int n(x,y,z)c(x,y,z)dx}{\int n(x,y,z)dx}. \tag{7.4}$$

We are interested in the line of sight average, as the 2-dimensional density distribution we obtain from our images is just this, an average in the direction of the propagating

camera beam. If we perform the above integral we find that the line of sight average of isotropic sound equation is,

$$\langle c_I(y,z)\rangle = \frac{128}{45\pi}\sqrt{\frac{\gamma\mu_G}{m}}\left(1-\frac{y^2}{R_y^2}-\frac{z^2}{R_z^2}\right)^{1/2}. \tag{7.5}$$

Further, if we were to average over the other radial direction as well, $\langle c(z)\rangle = \int n(x,y,z)c(x,y,z)dxdy/\int n(x,y,z)dxdy$, we would find that the equation for the radially (x- and y-direction) averaged isotropic sound is,

$$\langle c_I(z)\rangle = \frac{5}{6}\sqrt{\frac{\gamma\mu_G}{m}}\left(1-\frac{z^2}{R_z^2}\right)^{1/2}. \tag{7.6}$$

However, we excite the sound wave with a repulsive sheet potential. According the hydrodynamic theory the velocity should not depend on the radial coordinates of the trap (x- and y- direction). Instead the density perturbation created by a sheet potential travels in the z-direction as a plane wave. We found that the equation for sound velocity under these conditions is,

$$c = \left(\frac{1}{m}\frac{\int n_0 d^2\rho}{\int \left(\partial\mu/\partial n|_{n=n_0}\right)^{-1} d^2\rho}\right)^{1/2}. \tag{7.7}$$

In the general case for a zero temperature gas that obeys a power law equation of state ($\mu_L = \mathcal{C}n^\gamma$), is trapped in a harmonic potential, and follows the LDA ($\mu_G = \mu_L + V_{Ext}$), we have shown that the above equation reduces to,

$$c(z) = \sqrt{\frac{\gamma\mu_G}{m(1+\gamma)}}\left(1+\frac{z^2}{R_z^2}\right)^{1/2}, \tag{7.8}$$

where c(z) is the speed of sound in the axial (z-direction) center of the trap. This

equation depends upon γ and μ_G, the global chemical potential.

We want to observe that the sound propagates according to the theory [58] discussed in Chapter 3. It is important to test our theory against the data. There are two significant qualitative results derived in the section covering hydrodynamic theory. First, the sound velocity is constant over the radial direction (x- and y- direction) of the trap (i.e velocity should not have any dependence on the radial position of the trapped gas). This is different from isotropic sound propagation where the velocity does vary in the radial of the atomic cloud.

In order to confirm the velocity remains constant over the radial direction of the trap find the velocity in small radial bin. Instead of integrating across the radial direction of the trap to obtained a fully binned distribution, we measure the speed of the propagating features at specific values of ρ. The the sound velocity as a function of ρ is shown in Figure 7.1. We find that the velocity remains constant across most

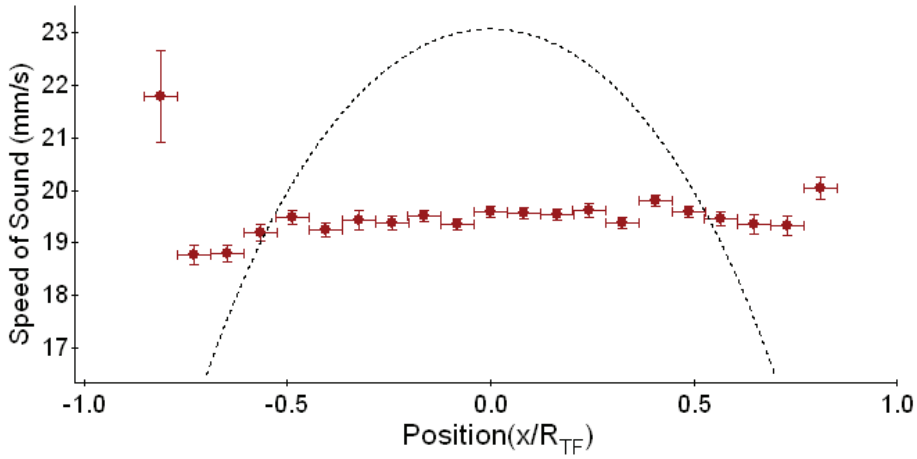

Figure 7.1: The sound velocity is plotted as a function of the radial (ρ) coordinate. We find the velocity remains constant across the radius of the cloud. The dotted line is isotropic sound propagation at z=0.

of the cloud. We can plainly see that the velocity does not propagate according

to isotropic sound theory (dotted line). Thus we can conclude that our plane wave description of the sound pulse is valid.

Second, dependence of the position and velocity of the sound pulse on time is sinusoidal, equations (3.40) and (3.41).

$$z(t) = R_z \sin\left(\frac{c(0)t}{R_z}\right) \tag{7.9}$$

$$v_z(t) = c(0)\cos\left(\frac{c(0)t}{R_z}\right). \tag{7.10}$$

This is actually true for isotropic sound propagation as well. Note that in both in equation for isotropic sound propagation and plane wave propagation, that the sound velocity $\propto \left(1+\frac{z^2}{R_z^2}\right)^{1/2}$. As the density wave travels through the gas it moves from an area of high density at the center to low density at the edge. As one might expect the speed at which the perturbation travels at the edge is slower than in the center of the trap. In order to account for this variation the position versus time data was not fit to a straight line. Instead we used a sine wave fit as predicted from our hydrodynamic model. We then extrapolate the velocity at the center of the trap. When we track the position of the wave versus time we find that a sin function provides a good fit to the data.

In Figure 7.2 I present the position versus time data in a new form. Recall that we track four independent features, two peaks (regions of increased density) and two valleys (regions of decreased density). In this figure, I have changed the sign of the time values for two of the features in order to more clearly display the sine function fit. Further, as the peak position is not in the center of the trap in at $t = 0$ I have shifted the entire the peak data set by $\Delta t = \pm\Delta z/c(0)$. Note that the period and amplitude of the sine function is different for the peak and valley data. This is consistent as the

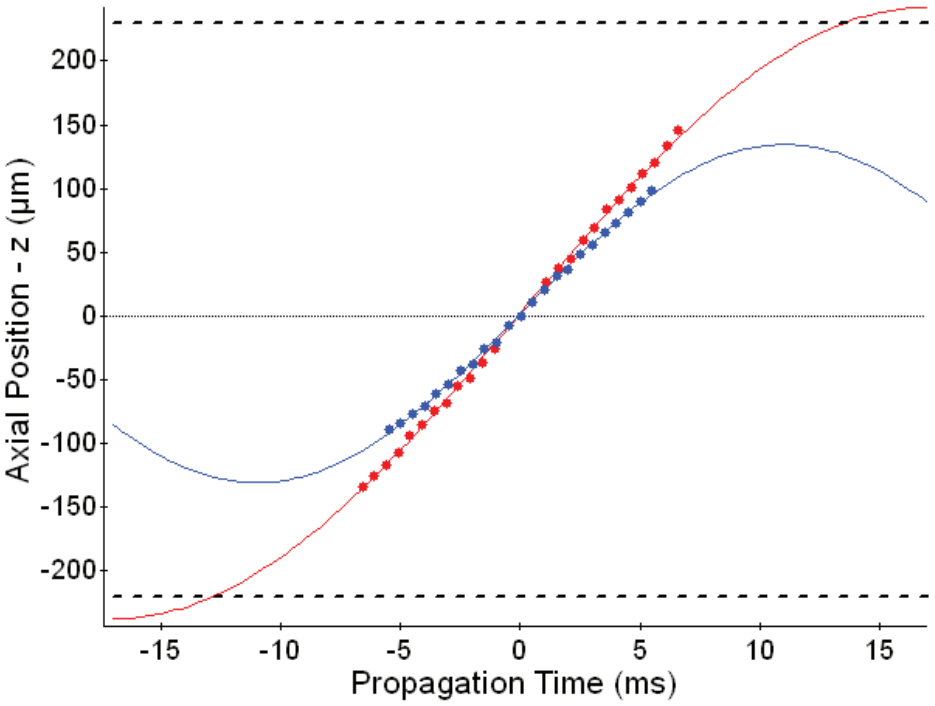

Figure 7.2: Peak (red dots) and Valley (blue dots) position plotted versus time and fit with a sine function (red and blue curves). The cloud edge (dotted lines) is shown as well.

valley are regions of low density and the peaks are regions of high density relative to the equilibrium density.

By examining the ρ-dependence of the sound velocity, I have verified that the velocity is indeed propagating as a plane wave. Also, the sinusoidal variation in the position versus time has been confirmed. These tests help us insure that we are utilizing the correct hydrodynamic model of sound propagation.

7.2 Dimensionless parameter $1/(k_F a)$

In Section 2.3 we discussed the interparticle interaction at the limits of the crossover region. Previously we discussed theories corresponding to the limits of the crossover region as a function of the s-wave scattering length:

$$\begin{aligned} a_s \to 0^- &: \textit{Ideal Fermi Gas} \\ a_s \to \pm\infty &: \textit{Unitary Gas} \\ a_s \to 0^+ &: \textit{Bose Gas}. \end{aligned}$$

The generally accepted way to characterize our gas near the Feshbach resonance is to utilize the dimensionless quantity $1/(k_F a)$. Here k_F is the global Fermi wave number and a is the s-wave scattering length. In previous chapters it was important to distinguish local and global quantities and we denoted the global Fermi wave vector as k_{F0}. However, in this chapter I will use k_F to denote the global quantity. There are two main advantages in using the dimensionless quantity $1/(k_F a)$ to organize our data. First, the quantity does not diverge at the Feshbach resonance when $a \to \pm\infty$.

Second, the value k_F contains important information about the length scale of the trapped gas without being dependent on the magnetic field. For example, we can adjust the value of $1/(k_F a)$ by adjusting the trap depth instead of the magnetic field. Unless of course the magnetic field is tuned to the Feshbach resonance in which case $1/(k_F a) = 0$ at all trap depths.

In characterizing the trapped gas by $1/(k_F a)$ we can identify regions of interactions as opposed to limits. Strong interactions exist on both sides of the resonance where $|k_F a| > 1$. Outside of this region the Fermi wave number is greater than the scattering length and the gas can be characterized as weakly interacting. The regions that will be investigated in this chapter are,

$$\begin{aligned}
\frac{1}{k_F a} < -1 \quad &: \quad \textit{Weakly Interacting BCS} \\
-1 < \frac{1}{k_F a} < 0 \quad &: \quad \textit{Strongly Interacting BCS} \\
\frac{1}{k_F a} = 0 \quad &: \quad \textit{Unitary Gas} \\
0 < \frac{1}{k_F a} < 1 \quad &: \quad \textit{Strongly Interacting BEC} \\
1 < \frac{1}{k_F a} \quad &: \quad \textit{Weakly Interacting BEC}.
\end{aligned}$$

In our experiment on sound velocity we took data over a range of magnetic fields and trap depths. Recall that the magnetic field determines the s-wave scattering length,

$$a = a_{bg}\left(1 - \frac{\Delta_B}{B - B_0}\right), \tag{7.11}$$

where a_{bg} = -1405 a_0 (a_0 is the Bohr radius), B_0 = 834.149 G, and Δ_B = 300 G [76].

A plot of the scattering length versus magnetic field across this resonance is shown in Figure 2.3. Also the global Fermi wave number is a function of the Fermi energy,

$$\hbar k_F = \sqrt{2mE_F}, \tag{7.12}$$

where $E_F = \hbar\overline{\omega}(3N)^{1/3}$ depends upon the number of trapped atoms as well as the geometry and intensity of the trapping potential.

7.3 Sound velocity in the BEC-BCS crossover

When we take data at 834G, the Feshbach resonance, $1/(k_F a) = 0$ regardless of the value of the Fermi wave vector as the s-wave scattering length diverges, $a \to \pm\infty$. These means that the value of $c(0)/v_F$ taken at resonance should be constant at any trap depth. The density at the center of the trap is a function of the trap intensity. In order to insure that the value of $c(0)/v_F$ remains constant with density (i.e. $c(0)$ and v_F scale together as a function of density) we performed the experiment over a large range of trap depths varying the intensity of the laser at the final trap depth from 0.068% to 10%. This corresponds to a factor of 50 in density at the center of the trap.

The experiment is so sensitive that it actually revealed an error in our magnetic field calibration. Originally, what we thought was 834 G turned out to be 820 G. We were able to see the value of $c(0)/v_F$ vary as the final trap depth became extremely shallow, and the value of k_F approach the s-wave scattering length. Figure 7.3 shows the sound velocity as a function trap depth of the data taken at 820 G. See how the velocity at the lowest two trap depths are significantly lower than the velocity at the

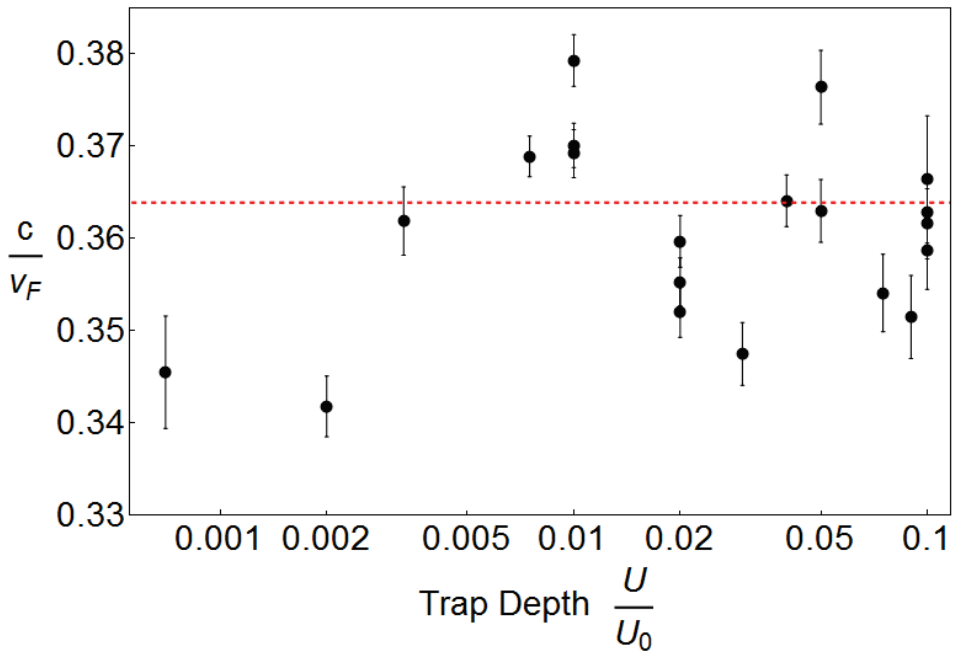

Figure 7.3: Sound velocity, $c(0)/v_F$ as a function of trap depth, U/U_0 at 820G.

higher trap depths. This is due to the fact that at the low trap depth the value of the Fermi wave vector k_F, which scales as $n^{1/3}$, is very small. The small value of k_F competes with the very large value of the s-wave scattering length a, and the value of $1/(k_F a)$ is non-zero.

After calibrating the magnetic field we found that this effect went away. Figure 7.4 shows the value of $c(0)/v_F$ versus the fractional trap depth at resonance. When we use the correct magnetic field, the data varies statistically about an average as is not a function of the final trap depth.

The equation for the sound velocity in a unitary gas at the axial center of the trap is,

$$\frac{c(0)}{v_F} = \frac{(1+\beta)^{1/4}}{\sqrt{5}}. \tag{7.13}$$

The average value of $c(0)/v_F$ is used to determine β. β as a function of the sound

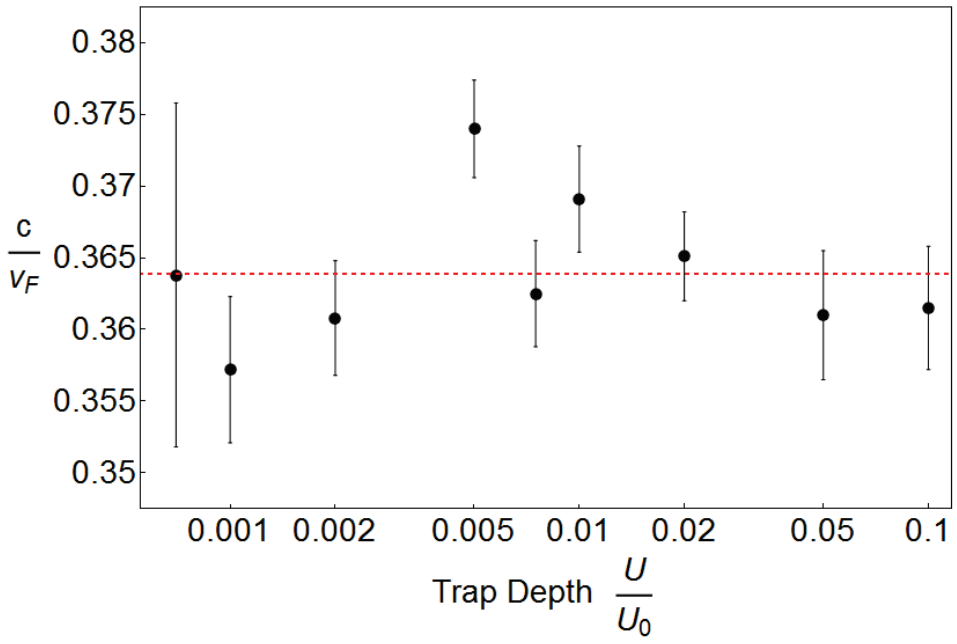

Figure 7.4: Sound velocity, $c(0)/v_F$ as a function of trap depth, U/U_0 at 834G

velocity is,

$$\beta = \left(\sqrt{5}\frac{c(0)}{v_F}\right)^4 - 1. \tag{7.14}$$

Table 7.1 gives a summary of the sound velocity data taken in the unitary gas. In our experiment we measured the sound velocity of a unitary gas and determined the value of $c(0)/v_F = 0.364(0.005)$ and $\beta = -0.561(0.025)$. The errors reported are the standard deviation of the data. Note that the standard deviation associated with the β measurement is much greater in proportion to the value of β as it depends on the sound velocity to the fourth power.

One further note on the β determination, in our paper on sound velocity [19] we reported that $\beta = -0.564(0.002)$. Here we choose to include data from 820 G excluding only the two data points taken at the lowest trap depths. Also, the error reported is the standard error.

Trap Depth	$\mathbf{c(0)/v_F}$	β
0.07%	0.364	-0.562
0.10%	0.357	-0.593
0.20%	0.361	-0.576
0.50%	0.374	-0.511
0.75%	0.363	-0.568
1.00%	0.369	-0.536
2.00%	0.365	-0.556
5.00%	0.361	-0.575
10.00%	0.362	-0.573
Average	**0.364(0.005)**	**-0.561(0.025)**

Table 7.1: Sound velocity, $c(0)/v_F$, and β taken at 834 G over a range of trap depths.

In addition to the data taken on resonance we measured the sound velocity over a range of magnetic fields (650G to 1100G) and trap depths (0.02% to 10%) corresponding to a range of values in $1/(k_F a)$ (-1.3 to 6). Figure 7.5, shows the sound velocity ($c(0)/v_f$)as a function of $1/(k_F a)$. In addition to the data I have included the curves we generated in Section 3.3.2 using a simple mean field model. For negative values of $1/(k_F a)$, the data agrees well with the simple mean field curve generated in the BCS limit (blue/upper curve). The BCS curve also agrees well with the data for a unitary gas at $1/(k_F a) = 0$ and beyond into the strongly interacting BEC region, $0 < 1/(k_F a) < 0.5$. At some point ($1/(k_F a) \approx 0.5$) the data diverges from the BCS curve and starts to resemble the simple mean field curve generated in the BEC limit (red/lower curve). In the weakly interacting BEC region, $1/(k_F a) > 1$ the data agrees well with the BEC curve. However, in the farthest BEC limit there are some discrepancies that will be discussed later in this section.

We are interested in how the sound velocity approaches the zero temperature theory in the limits near our Feshbach resonance at 834 G. Equation (7.13) is the

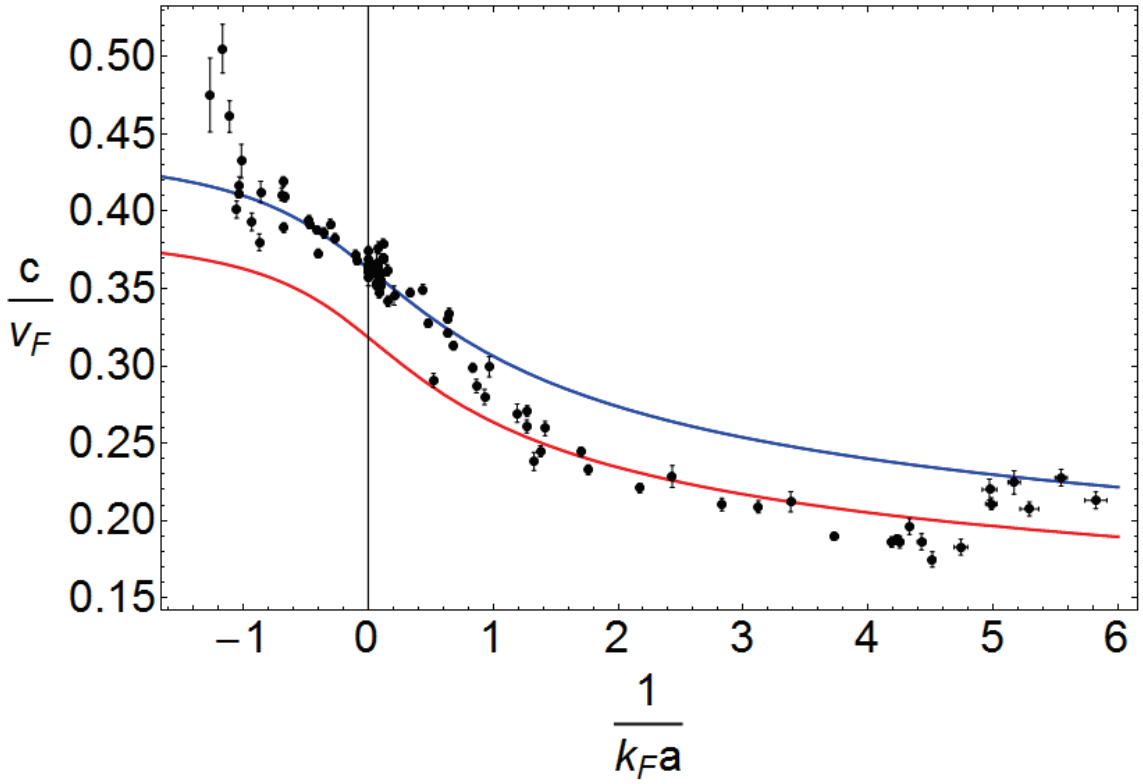

Figure 7.5: Sound velocity, $c(0)/v_F$ as a function of $1/(k_F a)$ (Black Dots). Curves are generated from a simple mean field model. Upper curve (Blue) corresponds to the BCS mean field curve. Lower curve (Red) corresponds to the BEC mean field curve.

velocity at resonance. The equation for the sound velocity in an ideal gas is,

$$\frac{c(0)}{v_F} = \frac{1}{\sqrt{5}}. \tag{7.15}$$

The velocity should approach equation (7.15) as the gas is tuned further into the BCS limit. The equation for the sound velocity in a BEC is,

$$c(0) = \frac{1}{4}\left(\frac{5}{2}a_{mol}k_F\right)^{1/5} v_F, \tag{7.16}$$

where a_{mol} is the molecular scattering length which depends on a. Note that the above equation varies with $1/(k_F a)$. By comparing to BEC theory we will be able to make an evaluation as to the dependance of $a_{mol}(a)$ on a. Figure 7.6 shows the sound velocity data taken over the crossover along with the zero temperature theoretical curves in the limits of the crossover region.

Note that the value of $c(0)/v_F$ increase as we move further into the BCS regime (more negative) from the unitary gas limit ($1/(k_F a) = 0$. I mentioned that the region of strong interactions is considered to be where $|k_F a| > 1$. When we cross this threshold the gas is no longer hydrodynamic. We find that as we tune further into the BCS regime, the gas becomes ballistic. It becomes difficult to image the density perturbation as it traverses the atomic cloud. As the measurement becomes more difficult the error in the measurement increases. Note the large error bars associated with the most negative values of $1/(k_F a)$. Eventually, the system is no longer hydrodynamic and we cannot observe the hydrodynamic sound propagation at all.

However, one can see that the gas does behave how we expect it to. The sound velocity is indeed approaching the ideal gas value (dashed line). It is only due to the

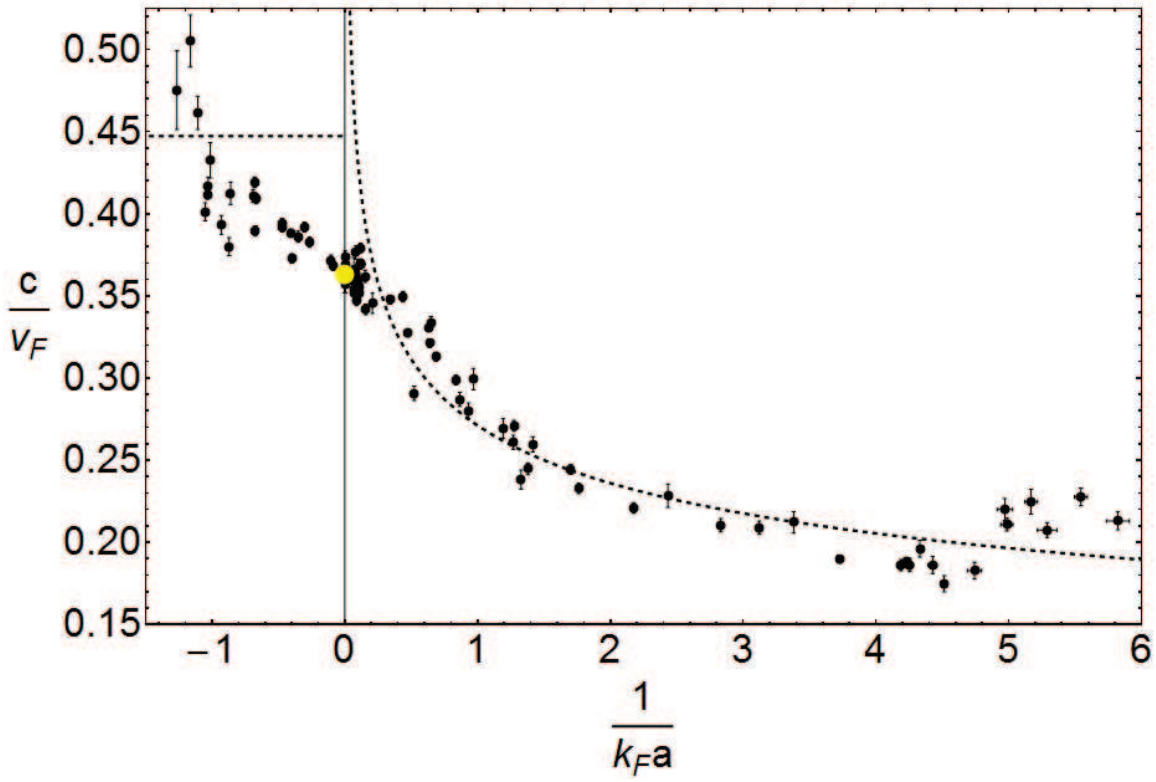

Figure 7.6: Sound velocity, $c(0)/v_F$ as a function of $1/(k_F a)$ (Black Dots). The sound velocity in a unitary gas is represented by the large yellow dot. The sound velocity in the BCS (negative values of $1/(k_F a)$) and BEC (positive values of $1/(k_F a)$ are represented by the black dashed curves.

fact that as we proceed further into the weakly interacting region the hydrodynamics fail that we cannot see sound propagate in an ideal gas under the current experimental procedure.

When we tune the magnetic field towards the BEC side of resonance the fermions become diatomic molecules. These molecules are comprised of two fermions and are bosons. When the gas is cooled to sufficiently cool temperature the gas becomes a fully condensed BEC. There is much debate as to what the equation of state should be for the strongly interacting region on this side of the resonance, $0 < 1/(k_F a) < 1$. This is the in-between region where the gas in neither a unitary gas nor a weakly interacting BEC.

We use the predictions from Reference [29], where an exact solution to the four-fermion scattering problem gives $a_{mol}(a) = 0.6a$ in the zero temperature BEC theory curve. For smaller values of $1/(k_F a)$,$(1 < 1/(k_F a) < 3)$ the data agrees well with the zero temperature BEC theory (dashed line). However, in the far molecular regime $(3 < 1/(k_F a) < 5)$ the data is systematically lower than either curve, and in the furthest molecular regime $(5 < 1/(k_F a))$ the data is systematically higher than either curve.

The lower measured speed may arise from coupling of first and second sound. Second sound is predicted to travel slower than first sound [46]. It does not appear that temperature is a concern as we observe no thermal component (as shown in Appendix B). In the furthest molecular regime the trap depth and magnetic field were tuned to minimize k_F and a simultaneously. In this case, after release the chemical potential was not large enough compared to the remaining magnetic trapping potential to obtain adequate expansion for ideal absorption imaging.

Finally, we compare our data to models predicting the sound velocity across

the entire crossover region. Figure 7.7 shows our sound velocity data along with two curves. The first curve is a mean field model based on the Legget ground state (purple/upper) [17]. The second is from a quantum Monte Carlo calculation (green/lower) [30]. The Legget curve (purple/upper) predicts a significantly higher sound velocity for all but the most negative points. In the BEC region this is mainly due to the fact that the Legget ground state predicts $a_{mol}(a) = 2a$. The quantum Monte Carlo result is in much better agreement with our data. Although the data are slightly lower than the prediction for $1/(k_F a) > 1$. Our data can used to test prediction of the equation of state for the entire crossover region.

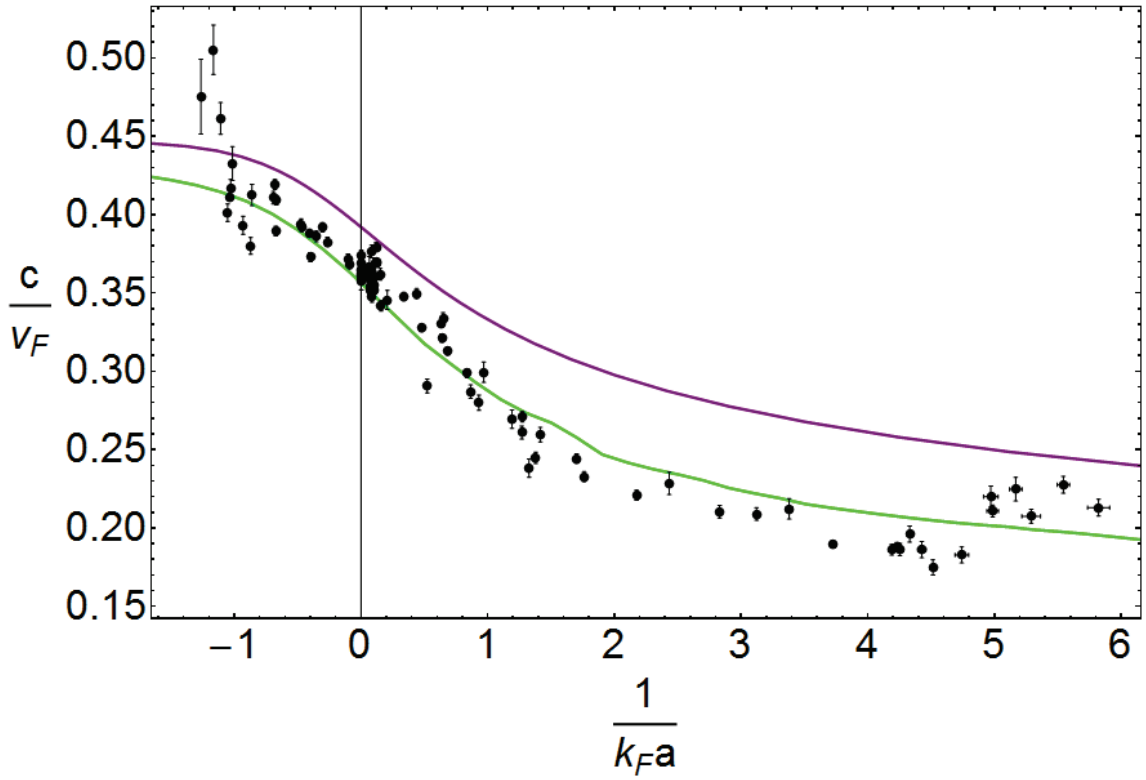

Figure 7.7: Sound velocity, $c(0)/v_F$ as a function of $1/(k_F a)$ (Black Dots). Curves are generated from a simple mean field model. The upper curve (Purple) corresponds to a mean field model based on the Legget ground state. The lower curve (Green) corresponds to a quantum Monte Carlo calculation.

Chapter 8

Conclusion

This dissertation highlighted a precision measurement of the sound velocity near a Feshbach resonance. This measurement was made possible through the implementation of various procedural upgrades on an existing cooling and trapping apparatus [62–67]. Our experiment is the first to measure sound in an ultracold Fermi gas over the entire BEC-BCS crossover.

In a near zero temperature unitary gas the average sound velocity at the axial center was measured, $c(0)/v_F = 0.364(0.005)$, as well as the universal constant, $\beta =$ -0.565(0.015). The measured sound velocity in units of the Fermi velocity was used to evaluate many-body theories predicting the equation of state. The data agrees will with weakly interacting Bose theory in the far BEC regime with a molecular scattering length of $a_m = 0.6a$, [29]. On the BCS side and at resonance the data agrees with a simple mean field model developed by Cheng Chin [28], who is now at the University of Chicago. I extended the simple mean field model to provide predictions of the sound velocity in a trapped gas. Through the entire crossover region the data most closely resembles the results of a quantum Monte Carlo calculation provided to us by Gregory Astrakharchik who works at the Universitat Politcnica de Catalunya, in Barcelona, Spain. We found that in our experiment sound propagated as a plane wave as described by Pablo Capuzzi [58] from Pisa, Italy.

Deep insight into the dynamics of sound propagation in our system allowed us to conduct a precision measurement. We were careful to take into account nonlinear effects and systematic errors in our measurement to insure that the data reflected the sound velocity of a gas trapped in a harmonic potential. In this dissertation I provided a complete analysis of the error associated with our measurement.

In the remaining sections of this chapter, I will provide a brief summary of the bulk of this dissertation. Next, I will discuss anticipated upgrades to the experimental system, both procedural and technical. Finally, I will speculate on the promise of future experiments on the system

8.1 Chapter summary

In Chapter 1, I began by observing the field of atom trapping and cooling from a historical perspective. Our experiment was also placed in the context of ongoing work, both theoretical and experimental. A direct connection was made to the fast expanse of theoretical prediction of the equation of state through the BEC-BCS crossover and to other strongly interacting systems in nature.

I highlighted the basic theoretical background required for understanding the trapping of Fermi gases near a Feshbach resonance in Chapter 2. Then, I outlined the physics of a dipole trap and the various zero temperature theories associated with the limits of the BEC-BCS crossover region: the ideal gas limit, the unitary gas limit, and the weakly interacting Bose gas limit. Chapter 2 also provided a description of the electronic states of ^6Li in a magnetic field, which was the basis of my discussion of the s-wave scattering length between the lowest two hyperfine states of ^{6}Li near a Feshbach resonance.

Chapter 3 included a description of the theory of hydrodynamic plane wave sound propagation in a trapped gas. The hydrodynamic theory of sound propagation was used to evaluate the theoretical zero temperature sound velocity in the limits near a Feshbach resonance. Chapter 3 concluded with a description from a simple mean field model of the equation of state and the sound velocity prediction resulting from this model in the BEC-BCS crossover.

Chapter 4 summarized the basic experiment apparatus. Highlighted in Chapter 4 are the procedures employed to produce a near zero temperature gas over a range of interaction energies. I illuminated the physics underlying each stage of the experimental procedure, and provided a detailed account of important cooling and trapping techniques.

In Chapter 5, I described the details the sound velocity experiment. Beginning with the experimental set up of the blue detuned beam used to excite sound waves in our experiment, I went on to outline our analysis of the propagation dynamics of a density perturbation in a trapped gas. Chapter 5 also provided a detailed account of the evolution of the sound velocity experiment. I described a few potential sources of bias in our measurement and what we did to eliminate them. In addition to the sound measurement, I described the complementary measurements needed to determine the characteristic energy of the gas, the Fermi energy E_F.

Chapter 6 outlined the error analysis of our measurement. I showed how we determined the correction factors pertaining to anharmonic trapping conditions and bias in the atom number measurement. Previously I had detailed how I acquired a velocity for a moving density perturbation. In Chapter 6, I detailed the steps taken to transform that velocity into a measure of the speed of sound at the axial center of a harmonic trap in units of the fermi velocity as well as the error associated with

reported values.

In Chapter 7 I discussed the results of our experiment. I showed that sound travels as a plane wave in our experiment. I also compared our data to the zero temperature theories in the limit of the BEC-BCS crossover, a mean-field theory based on the Legget ground state, a quantum Monte Carlo calculation, and the simple mean field model presented earlier in this dissertation. The value of the universal sound velocity in units of the Fermi velocity and the universal constant β are reported in Chapter 7 as well.

8.2 Future experimental system upgrades

Recently, construction has been completed on an overhaul of the experimental apparatus I used to take the sound velocity data. The new lab is now more closely resembles the system constructed by Bason Clancy and Le Luo, former members of our group. The new experimental apparatus is more compact and less complicated. In the immediate future the green beam conditioning optics can be reinstalled. In addition to the schematic shown in Figure 5.1 an AO has been purchased for the 532 nm beam. This allows for greater control of the intensity of the and opens up new realms of experimentation.

Another avenue that is currently being investigated is replacing the dye laser system with a diode pumped solid state laser. Laser technology is constantly improving and there are currently lasers on the market which would suit our needs. A lot of effort is expended to maintain our dye laser system. We lose precious time waiting for the laser to stabilize, aligning the laser, and periodically changing out the dye. The advantages of a turn key laser system would be immense in terms of ease of use

and stability.

Finally, the major undertaking of revamping the experimental apparatus allows us a golden opportunity to refine our experimental processes. This is a chance to take a step back and reevaluate experimental procedures. By making the two labs as similar as possible we can optimize our productivity by sharing insights, procedural know-how, and control software between the two labs.

8.3 Outlook

The shaped laser light from the Verdi laser gives us a powerful experimental tool. We have used the repulsive potential generated by the green beam to excite a sound wave in our gas. With the additional intensity control of an AO we are able to perform additional experiments. We had already begun to take some of preliminary data before the overhaul of the experimental apparatus. Two experiments in particular appear to be relevant to the ongoing work on trapped gasses. First, we measured the sound velocity in finite temperature gases on resonance. Second, by increasing the intensity of the potential we are able to completely separate the gas. When the repulsive potential is removed, the two atomic clouds accelerate towards each other and collide. As a result we are able to observe interesting non-linear effects in the unitary gas.

Another possibility is using the repulsive potential of the green beam to excite the atoms locally. By modulating the intensity of the green beam at specific frequencies we might be able to excite localized parametric or slosh modes. These experiments may lead to the observation of second sound in the form of a thermal wave, as we might be able to heat the trapped atoms locally. Another exciting possibility is the

measurement of viscosity. We might be able to create a local deformation of the trapped atoms from which we would be able to measure the shear viscosity.

There are an infinite number of experiments that could be run. In determining the next are of exploration we must take into account the tools available to us, the feasibility of the experiment, and the importance of the work in a broader context. With the simplicity of our system as compared to other atom trapping experiments and the experience of the current lab members, we are in a position to conduct some very interesting experiments.

Appendix A

Sound data tables

In this Appendix I report all of the data and associated that is contained in the figures in Chapter 7.

Date	Field	% CO_2 Power	$c(0)$ (mm/s)	v_F (mm/s)	$\frac{c(0)}{v_F}$	$\Delta\frac{c(0)}{v_F}$	$\frac{1}{k_F a}$	$\Delta\frac{1}{k_F a}$
7/25/2006	700	0.02%	4.44	20.86	0.2130	0.0054	5.822	0.087
7/25/2006	700	0.03%	4.76	22.95	0.2075	0.0045	5.290	0.074
7/25/2006	700	0.04%	4.99	21.90	0.2276	0.0054	5.544	0.048
7/25/2006	700	0.04%	5.28	23.49	0.2247	0.0075	5.168	0.049
7/24/2006	700	0.05%	5.13	24.35	0.2108	0.0038	4.986	0.046
7/24/2006	700	0.05%	5.37	24.43	0.2200	0.0067	4.971	0.058
7/21/2006	700	0.06%	4.68	25.61	0.1828	0.0051	4.742	0.054
7/21/2006	700	0.07%	4.70	26.90	0.1748	0.0049	4.514	0.026
9/28/2006	700	0.07%	5.39	28.98	0.1861	0.0034	4.190	0.029
9/28/2006	700	0.07%	5.31	28.54	0.1862	0.0040	4.254	0.028
9/28/2006	700	0.07%	5.40	28.71	0.1881	0.0027	4.230	0.027
10/24/2006	700	0.07%	5.50	28.04	0.1961	0.0051	4.331	0.023
7/26/2006	709	0.03%	4.50	24.18	0.1862	0.0052	4.427	0.033
7/26/2006	709	0.07%	5.45	28.73	0.1898	0.0024	3.725	0.024
10/24/2006	720	0.07%	6.12	29.29	0.2089	0.0040	3.122	0.019
7/26/2006	724	0.03%	5.41	25.51	0.2122	0.0065	3.380	0.027
7/26/2006	724	0.07%	6.41	30.46	0.2104	0.0041	2.831	0.013
7/28/2006	740	0.07%	6.86	31.04	0.2209	0.0032	2.175	0.019
10/24/2006	740	0.07%	6.34	27.75	0.2284	0.0071	2.433	0.019
9/29/2006	740	0.20%	8.93	38.35	0.2328	0.0031	1.761	0.009
10/17/2006	748	0.75%	13.40	49.72	0.2694	0.0059	1.192	0.005
7/28/2006	753	0.07%	7.82	31.99	0.2443	0.0030	1.702	0.007
9/29/2006	759	0.20%	10.41	38.44	0.2709	0.0033	1.273	0.008
10/17/2006	759	0.20%	10.07	38.59	0.2609	0.0042	1.269	0.007
9/29/2006	759	0.75%	15.13	50.53	0.2994	0.0065	0.969	0.005
10/24/2006	764	0.07%	7.92	32.34	0.2448	0.0036	1.379	0.007
7/31/2006	768	0.07%	7.41	31.11	0.2382	0.0058	1.327	0.016
10/17/2006	768	0.07%	7.57	29.16	0.2596	0.0046	1.416	0.011
9/29/2006	779	0.20%	11.68	39.09	0.2988	0.0029	0.837	0.005
9/20/2006	779	0.75%	16.84	50.49	0.3335	0.0039	0.648	0.003
9/20/2006	779	0.75%	16.47	51.28	0.3212	0.0026	0.638	0.003
9/20/2006	779	0.75%	17.01	51.43	0.3307	0.0022	0.636	0.002
9/26/2006	779	0.75%	14.96	47.78	0.3130	0.0027	0.685	0.003
7/31/2006	783	0.07%	8.97	32.03	0.2799	0.0049	0.931	0.005
10/24/2006	788	0.07%	8.73	30.40	0.2870	0.0043	0.866	0.005
8/2/2006	799	0.20%	13.13	40.06	0.3276	0.0024	0.477	0.002
8/1/2006	799	0.33%	15.24	43.59	0.3496	0.0032	0.439	0.002
8/1/2006	799	1.00%	19.66	56.54	0.3477	0.0026	0.338	0.002

Table A.1: Sound Velocity Data

Date	Field	% CO_2 Power	$c(0)$ (mm/s)	v_F (mm/s)	$\frac{c(0)}{v_F}$	$\Delta\frac{c(0)}{v_F}$	$\frac{1}{k_F a}$	$\Delta\frac{1}{k_F a}$
10/24/2006	803	0.07%	9.26	31.85	0.2907	0.0044	0.523	0.003
8/2/2006	821	0.07%	10.88	31.48	0.3455	0.0061	0.208	0.003
8/2/2006	821	0.20%	14.04	41.09	0.3418	0.0033	0.159	0.001
7/17/2006	821	0.33%	15.62	43.15	0.3619	0.0037	0.152	0.001
8/31/2006	821	0.75%	19.99	54.19	0.3689	0.0022	0.121	0.000
7/17/2006	821	1.00%	20.40	55.13	0.3701	0.0024	0.119	0.000
8/25/2006	821	1.00%	20.80	54.85	0.3793	0.0028	0.119	0.000
8/29/2006	821	1.00%	21.39	57.94	0.3692	0.0026	0.113	0.000
9/11/2006	821	2.00%	23.40	65.05	0.3597	0.0028	0.101	0.001
9/12/2006	821	2.00%	22.06	62.07	0.3553	0.0026	0.105	0.000
9/12/2006	821	2.00%	22.25	63.21	0.3520	0.0027	0.104	0.000
7/17/2006	821	3.00%	26.11	75.15	0.3475	0.0034	0.087	0.001
8/30/2006	821	4.00%	28.41	78.04	0.3641	0.0028	0.084	0.000
8/8/2006	821	5.00%	29.81	79.20	0.3764	0.0040	0.083	0.000
9/7/2006	821	5.00%	28.90	79.61	0.3630	0.0034	0.082	0.000
8/22/2006	821	7.50%	31.78	89.76	0.3541	0.0042	0.073	0.000
8/30/2006	821	9.00%	33.10	94.18	0.3515	0.0045	0.070	0.000
7/13/2006	821	10.00%	34.98	96.39	0.3629	0.0040	0.068	0.000
7/17/2006	821	10.00%	34.87	96.44	0.3616	0.0038	0.068	0.000
8/8/2006	821	10.00%	35.64	97.27	0.3664	0.0069	0.067	0.000
8/22/2006	821	10.00%	34.78	96.95	0.3587	0.0042	0.068	0.000
12/5/2006	834	0.07%	11.03	30.31	0.3638	0.0120	0.002	0.000
12/6/2006	834	0.10%	10.91	30.55	0.3572	0.0051	0.002	0.000
12/5/2006	834	0.20%	14.19	39.32	0.3608	0.0040	0.002	0.000
12/6/2006	834	0.50%	17.20	45.99	0.3740	0.0034	0.002	0.000
12/5/2006	834	0.75%	18.55	51.16	0.3625	0.0037	0.001	0.000
12/5/2006	834	1.00%	20.71	56.11	0.3691	0.0037	0.001	0.000
12/6/2006	834	2.00%	22.28	61.03	0.3651	0.0031	0.001	0.000
12/6/2006	834	5.00%	29.01	80.36	0.3610	0.0045	0.001	0.000
12/5/2006	834	10.00%	35.27	97.56	0.3615	0.0043	0.001	0.000
10/6/2006	847	0.75%	21.02	56.54	0.3718	0.0031	0.103	0.000
9/11/2006	847	2.00%	24.06	65.31	0.3684	0.0030	0.089	0.000
8/21/2006	867	0.20%	15.18	39.33	0.3860	0.0034	0.352	0.002
10/10/2006	876	0.20%	15.96	42.81	0.3728	0.0028	0.400	0.001
10/6/2006	876	0.75%	22.05	56.26	0.3919	0.0030	0.304	0.001
9/11/2006	876	2.00%	24.59	64.27	0.3826	0.0030	0.266	0.001
8/21/2006	906	0.20%	15.45	39.66	0.3895	0.0031	0.673	0.004

Table A.2: Sound Velocity Data (continued)

Date	Field	% CO_2 Power	$c(0)$ (mm/s)	v_F (mm/s)	$\frac{c(0)}{v_F}$	$\Delta\frac{c(0)}{v_F}$	$\frac{1}{k_F a}$	$\Delta\frac{1}{k_F a}$
10/6/2006	906	0.75%	22.28	56.87	0.3917	0.0026	0.469	0.002
10/6/2006	906	0.75%	22.29	56.58	0.3940	0.0033	0.472	0.002
9/11/2006	906	2.00%	25.34	65.26	0.3883	0.0024	0.409	0.002
8/21/2006	946	0.20%	15.61	39.70	0.3932	0.0057	0.930	0.006
8/31/2006	946	0.75%	22.78	54.33	0.4192	0.0032	0.680	0.003
10/10/2006	950	0.20%	16.50	43.42	0.3800	0.0054	0.871	0.003
10/6/2006	950	0.75%	23.21	56.72	0.4091	0.0030	0.667	0.003
8/29/2006	961	1.00%	23.88	58.14	0.4108	0.0040	0.691	0.002
8/21/2006	985	0.20%	18.66	40.44	0.4614	0.0101	1.108	0.008
10/10/2006	1014	0.20%	21.56	42.67	0.5052	0.0158	1.164	0.004
10/6/2006	1014	0.75%	23.83	57.74	0.4126	0.0068	0.860	0.003
10/10/2006	1053	0.20%	20.71	43.58	0.4753	0.0239	1.264	0.003
10/2/2006	1097	0.75%	24.31	58.33	0.4168	0.0056	1.029	0.004
10/2/2006	1097	0.75%	23.80	57.88	0.4112	0.0022	1.037	0.005
10/2/2006	1097	0.75%	22.89	57.06	0.4012	0.0055	1.052	0.006
10/6/2006	1097	0.75%	25.61	59.20	0.4326	0.0108	1.014	0.006

Table A.3: Sound Velocity Data (continued)

Appendix B

Condensate Fraction

In the bulk of this thesis I discussed the various zero temperature theories associated with the limits near a Feshbach resonance. One of these limits is the BEC limit where the Fermoion atoms pair and become Bose molecules. In this Appendix I will explore finite temperature Bose thermodynamics. The goal of this appendix is to discover a density distribution that can be used to fit finite temperature Bose gases. In a Bose gas at finite temperature below the critical temperature, T_C, a portion of the molecules will form a condensate and the rest, the thermal component will obey Boltzman statistics. By comparing the actual density distribution that we obtain from our absorption images to the theoretical curve we can determine the BEC fraction.

B.1 One Dimensional Profiles

The theory of uniform Bose gases is found in most texts on statistical mechanics and thermal physics [81], [82], [69]. The ratio of the density of thermal atoms, n_T, to the overall density, n, can be related to ratio of the temperature, T, over the critical temperature, T_C,

$$\frac{n_T}{n} = \left(\frac{T}{T_C}\right)^{3/2}. \tag{B.1}$$

This means that the ratio of the atoms in the condensate, n_{BEC}, to the overall density is,

$$\frac{n_{BEC}}{n} = 1 - \left(\frac{T}{T_C}\right)^{3/2}. \tag{B.2}$$

The critical temperature can be considered a local quantity. The critical temperature varies with overall density according to the equation,

$$k_B T_C = \left(\frac{1}{2.612}\right)\frac{\hbar^2}{m} n^{2/3}, \tag{B.3}$$

where m is the molecular mass and k_B is Boltzmann's constant.

The above equations hold for temperatures $T < T_C$. In a trapped gas in thermal equilibrium the temperature is constant, and the density varies spatially, densest in the center at diffuse at the edges. This means that the local critical temperature $T_C(\mathbf{r})$ will be greater than the temperature of the gas in some regions and less than the temperature of the gas in others. As a consequence, portions of the gas will be completely thermal while others will be a mixture of thermal and condensed atoms.

If the temperature is greater than the critical temperature ($T > T_C$) the distribution of thermal atoms follows the Maxwell Boltzman distribution [26],

$$n_T(\mathbf{r}) = \left(\frac{2\pi\hbar^2}{m k_B T}\right)^{-3/2} e^{-V_{HO}(\mathbf{r})/k_B T}. \tag{B.4}$$

When temperature is less than the critical temperature (i.e. $T < T_C(\mathbf{r})$) we can combine equations (B.1) and (B.3) to obtain,

$$n_T(\mathbf{r}) = \frac{1}{2.612}\left(\frac{m k_B T}{\hbar^2}\right)^{3/2}. \tag{B.5}$$

Note that in equation (B.5) the thermal density distribution depends only on temperature and does not vary in space.

Now lets do the same thing for the condensate density distribution n_{BEC}. For temperatures, $T > T_C$ there will be no condensate and $n_{BEC} = 0$. For temperatures below the critical temperature, $T < T_C$ the condensate fraction density distribution will scale according to zero temperature Bose statistics which we have already worked out in the bulk of this thesis. The condensate density distribution in a harmonic trap from the Bose equation of state and the local density approximation is,

$$n_{BEC}(\mathbf{r}) = \frac{\mu_G}{\mathcal{C}} \left(1 - \frac{r^2}{\sigma_r^2}\right), \tag{B.6}$$

where $\sigma_r = \sqrt{\frac{2\mu_G}{m}} \frac{1}{\omega_{HO}}$.

The critical temperature is a local quantity that depends on density. It is important to note the for a finite temperature gas μ_G depends upon the trap frequencies, total number of molecules, *and* the temperature, and will not be equivalent to the global chemical potential at zero temperature. Therefore, at some critical spatial position, σ_C, corresponding to a critical density n_C, there is a transition from the completely thermal gas at the edge of the cloud to a mixture of condensate and thermal components in the center. We already have defined the radius at which the condensate fraction goes to zero, thus we can equate this with the critical radius, $\sigma_C = \sigma_r$.

Figure B.1 shows the overall density distribution of a BEC with a thermal component. At the edge of the gas the density follows the Maxwell Boltzman distribution and the gas is comprised solely of thermal molecules. Once the local critical temperature exceeds the temperature of the gas, the gas is a mixture of a condensate

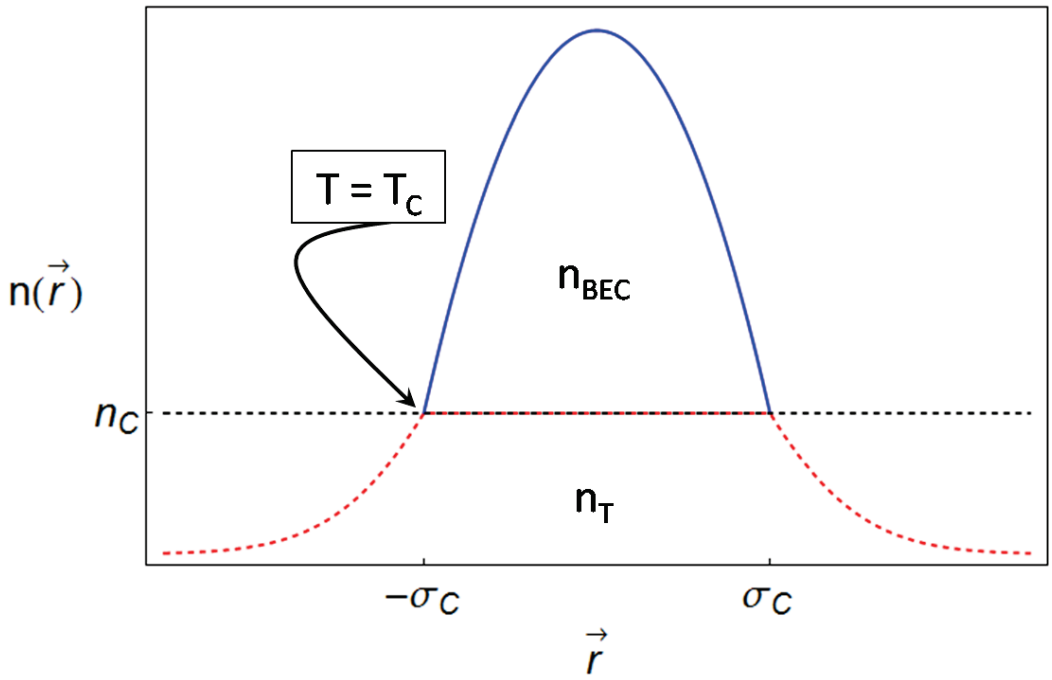

Figure B.1: Density distribution in a finite temperature Bose gas.

molecules and thermal molecules. The density of the thermal molecules remains constant while the density of the condensate molecules can be determined from zero temperature Bose statistics. The overall density distribution is the sum of the density of the thermal molecules and the density of the condensate molecules,

$$n(\mathbf{r}) = n_T(\mathbf{r}) + n_{BEC}(\mathbf{r}). \tag{B.7}$$

We use 2-dimensional absorption imaging to extract data from our experiment. One these images are obtained they are converted into 2D density distributions which are line of sight averages of the density. The 2D density distributions are then binned to create a 1D density profile. Therefore, we need to determine the 1D density distribution for both the thermal and condensate distributions. Assuming cylindrical symmetry and the normal cigar-shape of the trap the 1 D density profile is,

$$n(z) = 2\pi \int_0^\infty n(\rho, z)\rho d\rho. \tag{B.8}$$

When we break the overall density into its constituent parts we find,

$$n(z) = 2\pi \int_0^\infty n_T(\rho, z)\rho d\rho + 2\pi \int_0^\infty n_{BEC}(\rho, z)\rho d\rho. \tag{B.9}$$

Lets start with the condensate density. We need to define two critical radii, $\sigma_{\rho C} = \sqrt{\frac{2\mu_G}{m}}\frac{1}{\omega_\perp}$ and $\sigma_{zC} = \sqrt{\frac{2\mu_G}{m}}\frac{1}{\omega_z}$ such that beyond the ellipsoid bound by the surface $\rho^2/\sigma_{\rho C}^2 + z^2/\sigma_{zC}^2 = 1$ the condensate fraction is zero. For the 1D density profile this gives,

$$n_{BEC}(z) = 2\pi \int_0^{\sqrt{1-z^2/\sigma_{zC}}\sigma_{rC}} \frac{\mu_G}{\mathcal{C}} \left(1 - \frac{\rho^2}{\sigma_{\rho C}^2} - \frac{z^2}{\sigma_{zC}^2}\right) \rho d\rho, \tag{B.10}$$

for $|z| < \sigma_{zC}$ and

$$n_{BEC}(z) = 0, \tag{B.11}$$

for $|z| > \sigma_{zC}$. There is a change in variables that will greatly simplify our calculation. Let $\rho \rightarrow \rho'/\sigma_{\rho C}$ and $z \rightarrow z'/\sigma_{zC}$. Now the equation for the non-zero 1D profile on the condensate density becomes,

$$n_{BEC}(z) = 2\pi \frac{\mu_G}{\mathcal{C}} \sigma_{\rho C}^2 \int_0^{\sqrt{1-z'^2}} \left(1 - \rho'^2 - z'^2\right) \rho' d\rho'. \tag{B.12}$$

Once we solve this integral the 1 D condensate density is,

$$n_{BEC}(z) = \frac{\pi}{2} \frac{\mu_G}{\mathcal{C}} \sigma_{\rho C}^2 \left(1 - \frac{z^2}{\sigma_{zC}^2}\right)^2 : |z| < \sigma_{zC} \tag{B.13}$$

$$n_{BEC}(z) = 0 : |z| > \sigma_{zC} \tag{B.14}$$

Now lets consider the thermal distribution. Lets define the thermal amplitude, $A_T = \left(\frac{2\pi\hbar^2}{m k_B T}\right)^{-3/2}$, and thermal radii, $\sigma_{\rho T} = \frac{\sqrt{2k_BT/m}}{\omega_\perp}$, $\sigma_{zT} = \frac{\sqrt{2k_BT/m}}{\omega_z}$. Now the equation for the thermal density outside the critical ellipsoid defined by the surface, $\rho^2/\sigma_{\rho C}^2 + z^2/\sigma_{zC}^2 = 1$, is,

$$n_T(\rho, z) = A_T e^{-\frac{\rho^2}{\sigma_{\rho T}^2} - \frac{z^2}{\sigma_{zT}^2}}. \tag{B.15}$$

and the thermal density inside the ellipsoid is simply the thermal density at the surface because the thermal density is constant in the thermal/condensate mixture.

$$n_T(\rho, z) = A_T e^{-\frac{\sigma_{\rho C}^2}{\sigma_{\rho T}^2}} = A_T e^{-\frac{\sigma_{zC}^2}{\sigma_{zT}^2}}. \tag{B.16}$$

The ratios $\sigma_{\rho C}/\sigma_{\rho T}$ are equivalent σ_{zC}/σ_{zT} and equal to $\mu_G/(k_B T)$.

The 1D density profile can be calculated as,

$$n_T(z) = 2\pi \int_0^\infty A_T e^{-\frac{\rho^2}{\sigma_{\rho T}^2} - \frac{z^2}{\sigma_{zT}^2}} \rho d\rho, \tag{B.17}$$

for $|z| > \sigma_{zC}$. When $|z| < \sigma_{zC}$ we need to be careful. Part of the integral will occur outside the critical ellipsiod where the thermal density varies according to the Maxwell Boltzman distributions and part of the integral will occur inside the critical ellipsoid where the thermal density is constant. The surface of the ellipsiod is defined as $\rho^2/\sigma_{\rho C}^2 + z^2/\sigma_{zC}^2 = 1$. Therefore the point where we need to switch the equation for thermal density from constant to Maxwell Boltzmann is $\rho = \sqrt{1 - z^2/\sigma_{zC}^2}^2 \sigma_{\rho C}$. The integral is then,

$$n_T(z) = 2\pi \int_0^{\sqrt{1-z^2/\sigma_{zC}}\sigma_{\rho C}} A_T e^{-\frac{\sigma_{\rho C}^2}{\sigma_{\rho T}^2}} \rho d\rho + 2\pi \int_{\sqrt{1-z^2/\sigma_{zC}}\sigma_{\rho C}}^\infty A_T e^{-\frac{\rho^2}{\sigma_{\rho T}^2} - \frac{z^2}{\sigma_{zT}^2}} \rho d\rho, \tag{B.18}$$

for $|z| < \sigma_{zC}$.

Once we perform the integral the 1D profile reduces to

$$n_T(z) = \pi A_T \sigma_{\rho T}^2 \left[e^{-\frac{z^2}{\sigma_{zT}^2}} e^{-\left(1-\frac{z^2}{\sigma_{zC}^2}\right)\frac{\sigma_{\rho C}^2}{\sigma_{\rho T^2}}} + \frac{\sigma_{\rho C}^2}{\sigma_{\rho T}^2} e^{-\frac{\sigma_{\rho C}^2}{\sigma_{\rho T^2}}} \left(1 - \frac{z^2}{\sigma_{zC}^2}\right) \right] : |z| < \sigma_{zC} \tag{B.19}$$

$$n_T(z) = \pi A_T \sigma_{\rho T}^2 e^{-\frac{z^2}{\sigma_{zT}^2}} : |z| > \sigma_{zC} \tag{B.20}$$

This combined with our equation for the 1D condensate density profile is the overall density of a finite temperature BEC.

B.2 Curve Fitting

The 1 Dimensional profiles we worked out in the previous section may seem complicated. But when you break them down it turns out that we can fit the finite temperature profiles with just four fitting parameters. Lets make the following substitutions and see what happens.

$$\begin{aligned} \frac{\pi}{2}\frac{\mu_G}{\mathcal{C}}\sigma_{\rho C}^2 &\rightarrow A_1 \\ \pi A_T \sigma_{\rho T}^2 &\rightarrow A_2 \\ \frac{\sigma_{\rho C}}{\sigma_{\rho T}} &\rightarrow R \end{aligned}$$

The 1D BEC density profiles can be expressed,

$$n_{BEC}(z) = A_1\left(1-\frac{z^2}{\sigma_{zC}^2}\right)^2 : |z| < \sigma_{zC} \tag{B.21}$$

$$n_{BEC}(z) = 0 : |z| > \sigma_{zC} \tag{B.22}$$

and the 1D thermal density profiles can be expressed,

$$n_T(z) = A_2\left[e^{-\frac{z^2}{\sigma_{zT}^2}}e^{-\left(1-\frac{z^2}{\sigma_{zC}^2}\right)R^2} + R^2 e^{-R^2}\left(1-\frac{z^2}{\sigma_{zC}^2}\right)\right] : |z| < \sigma_{zC} \tag{B.23}$$

$$n_T(z) = A_2 e^{-\frac{z^2}{\sigma_{zT}^2}} : |z| > \sigma_{zC}. \tag{B.24}$$

The variable in the fits are σ_{zT},σ_{zC},A_1,A_2, and R. However, we know that the ratios $\frac{\sigma_{zC}}{\sigma_{zT}} = \frac{\sigma_{rC}}{\sigma_{rT}} = R$. Therefore R is not a free parameter and we can fit with four variables. Figure B.2 shows the 1-dimensional profiles.

Once we have the four parameter fit we can calculate the condensate fraction by

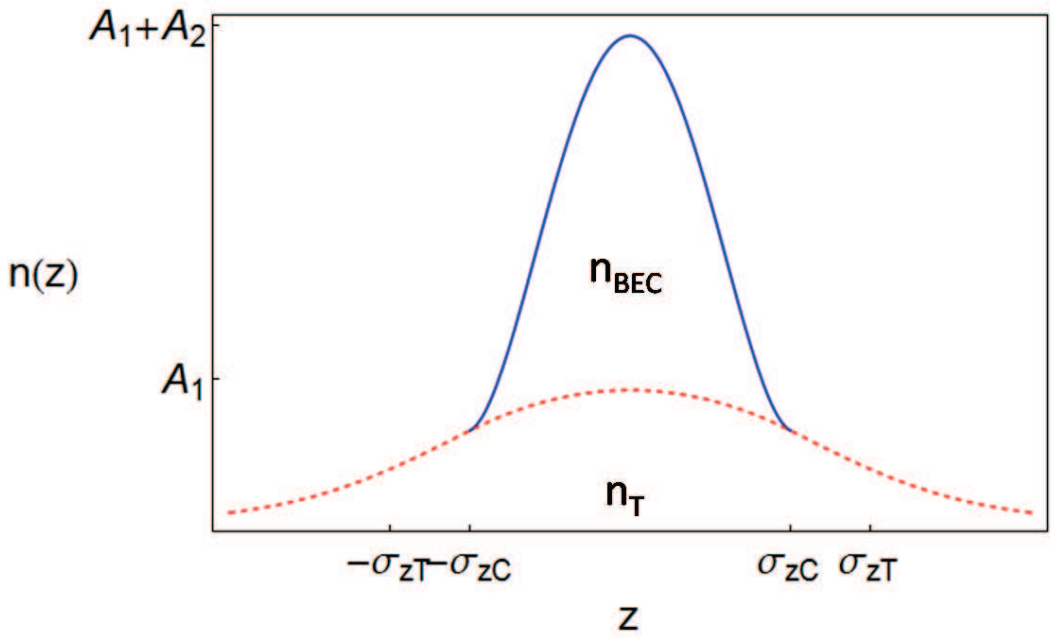

Figure B.2: Integrated density distribution in a finite temperature Bose gas.

integrating the 1-D densities over the z-direction,

$$\frac{N_{BEC}}{N} = \frac{\int_{-\infty}^{\infty} n_{BEC}(z)dz}{\int_{-\infty}^{\infty} n_T(z) + n_{BEC}(z)dz}. \tag{B.25}$$

The temperature of the gas is a function of the condensate fraction,

$$\frac{T}{T_{C0}} = \left(1 - \frac{N_{BEC}}{N}\right)^{2/3}, \tag{B.26}$$

where T_{C0} is the global critical temperature which is the critical temperature at the center of the trap according to equation (B.3).

Figure B.3 shows the results of fits using Igor to density profiles of BECs at various condensate fractions.

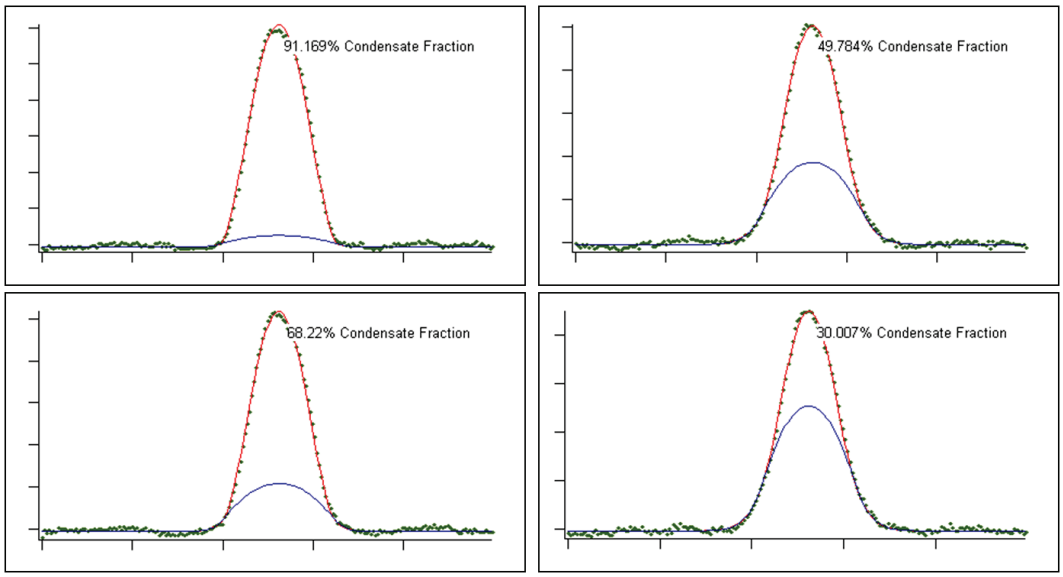

Figure B.3: 1-dimensional profiles of several BECs at various condensate fractions. Condensate fraction is noted. Fits include overall density $n(x)$ (Red) and thermal density $n_T(x)$ (Blue).

Appendix C

Simple Mean Field Model

The mathematic code used to produce the figures in this thesis pertaining to the Simple Mean Field Model

```
α = 2.338107410459767;
am = .6 a;
A = (am/a 4π)^(-2/3) (6π^2)^(2/3);
B = (am/a 4π)^(1/3) / (6π^2)^(1/3);
eq1 = AiryAiPrime[-α μ] == -AiryAi[-α μ] α^(1/2) x;
eq2 = 1/(x α^(1/2)) == -AiryAi[-α μ]/AiryAiPrime[-α μ];
eq3 = AiryAiPrime[-A μ] == -x/B AiryAi[-A μ];
eq4 = B/x == -AiryAi[-A μ]/AiryAiPrime[-A μ];
Eb[x_] := If[x < 0, 0, x^2]

Quiet[
 μ1 = Table[{i, μ /. FindRoot[eq1 /. x → i, {μ, 1}]}, {i, -100, -2.1, .1}];
 μ2 = Table[{i, μ /. FindRoot[eq1 /. x → i, {μ, .55}]}, {i, -2.0, 0.3, .1}];
 μ3 = Table[{i, μ /. FindRoot[eq1 /. x → i, {μ, -i^2}]}, {i, 0.4, 6, .1}];
 μ4 = Table[{i, μ /. FindRoot[eq2 /. x → i, {μ, -i^2}]}, {i, 6.1, 100, .1}];
]

Quiet[
 μ5 = Table[{i, μ /. FindRoot[eq3 /. x → i, {μ, .4}]}, {i, -100, -1.0, .1}];
 μ6 = Table[{i, μ /. FindRoot[eq3 /. x → i, {μ, .25}]}, {i, -0.9, 0.3, .1}];
 μ7 = Table[{i, μ /. FindRoot[eq3 /. x → i, {μ, -i^2}]}, {i, 0.4, 5, .1}];
 μ8 = Table[{i, μ /. FindRoot[eq4 /. x → i, {μ, -i^2}]}, {i, 5.1, 100, .1}];
]

μBCS = Interpolation[Join[μ1, μ2, μ3, μ4]];
μBEC = Interpolation[Join[μ5, μ6, μ7, μ8]];
Plot[{μBCS[x], -Eb[x], μBEC[x]}, {x, -√2, √2}, PlotRange → {-2.05, 2.05}, AxesLabel → {"1"/"k_F" <> "a", "μ"/"ε_F"},
 AxesStyle → Directive[32, FontFamily → "Helvetica", Thickness[0.002]], PlotStyle → {{Blue, Thickness[0.003]}, {Black, Thickness[0.002], Dashed}, {Red, Thickness[0.003]}}]
```

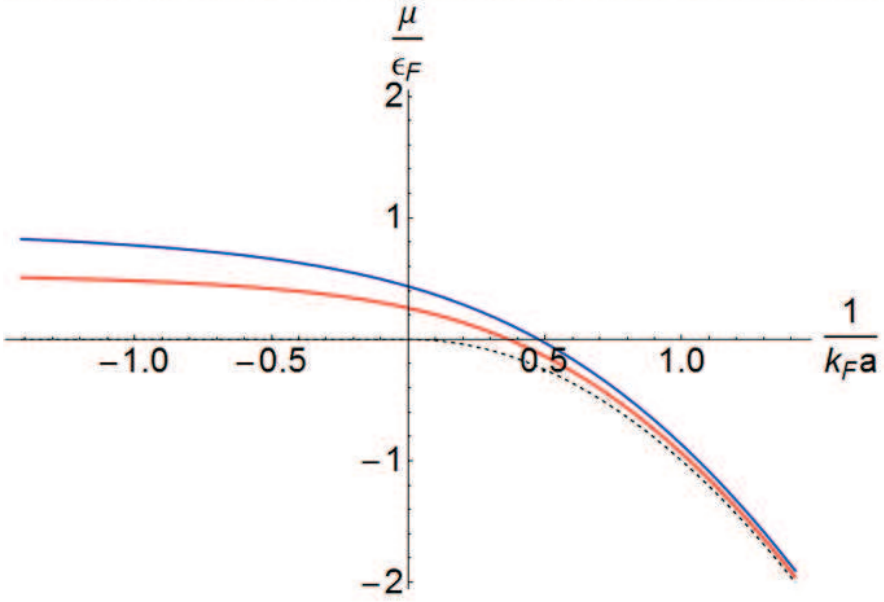


```
γBCS[x_] := 2/3 (1 + Eb[x]/μBCS[x])^(-1) (1 + 1/2 α^(-3/2) x μBCS[x]^(-2))/(1 + x^2 μBCS[x]^(-1))
γBEC[x_] := 2/3 (1 + Eb[x]/μBEC[x])^(-1) (1 + 1/2 A^(-3/2) x μBEC[x]^(-2))/(1 + x^2 μBEC[x]^(-1))
Show[Plot[{γBCS[x]}, {x, -2.5, 2.5}, PlotRange → {.5, 1.05}, AxesLabel → {"1"/"k_F" <> "a", "γ"}, AxesStyle → Directive[32, FontFamily → "Helvetica", Thickness[0.002]],
  PlotStyle → {Black, Thickness[0.003]}], Plot[1, {x, 0, 2.5}, PlotStyle → {Black, Dashed, Thickness[0.002]}],
 Plot[2/3, {x, -2.5, 0}, PlotStyle → {Black, Dashed, Thickness[0.002]}]]
```

```
Show[Plot[{γBCS[x]}, {x, -2.5, 2.5}, PlotRange → {.5, 1.05}, AxesLabel → {"1/(k_F <> a)", "γ"}, AxesStyle → Directive[32, FontFamily → "Helvetica", Thickness[0.002]],
  PlotStyle → {Black, Thickness[0.003]}], Plot[1, {x, 0, 2.5}, PlotStyle → {Black, Dashed, Thickness[0.002]}],
 Plot[2/3, {x, -2.5, 0}, PlotStyle → {Black, Dashed, Thickness[0.002]}]]
```

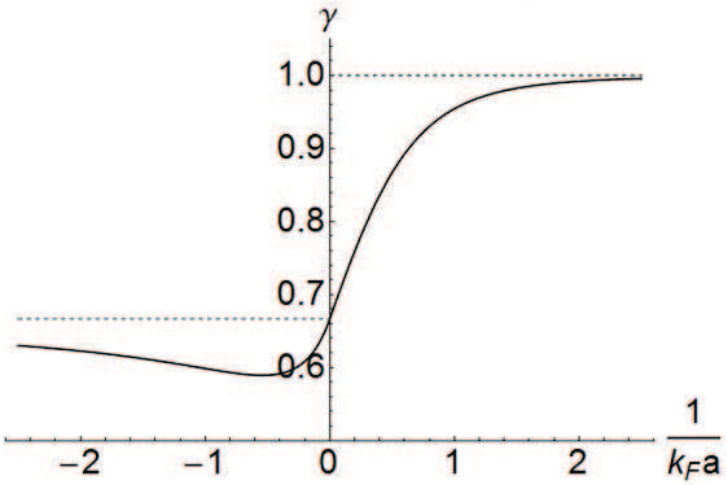


```
μdenBCS[x_, n_] := ((n)^(2/3) μBCS[x (n)^(-1/3)]) + Eb[x];
μdenBEC[x_, n_] := ((n)^(2/3) μBEC[x (n)^(-1/3)]) + Eb[x];
```

```
BECList = {};
For[x = -2.20, x < 6, x = x + .2;
 {denμ = Interpolation[Join[{{0, 0}}, Table[{μdenBEC[x, n], n}, {n, 0.01, 25, .01}]]];
  I2[μG_] := 32/π NIntegrate[denμ[μG - ρ] 1/2 √ρ, {ρ, 0, μG}];
  μrep = μG /. FindRoot[I2[μG] - 1 == 0, {μG, .5, 0, 1}, AccuracyGoal → 4];
  DμDn = Interpolation[Table[{i, D[μdenBEC[x, n], n] /. n → i}, {i, 0.01, 10, .01}]];
  cc = √(1/2 NIntegrate[r denμ[μrep - r^2], {r, 0, √μrep}] / NIntegrate[r (DμDn[denμ[μrep - r^2]])^-1, {r, 0, √μrep}]);
  BECList = Append[BECList, {x, cc}];
  Print[x];
 }]
```

```
BCSList = {};
For[x = -2.20, x < 6, x = x + .2;
 {denμ = Interpolation[Join[{{0, 0}}, Table[{μdenBCS[x, n], n}, {n, 0.01, 25, .01}]]];
  I2[μG_] := 32/π NIntegrate[denμ[μG - ρ] 1/2 √ρ, {ρ, 0, μG}];
  μrep = μG /. FindRoot[I2[μG] - 1 == 0, {μG, .5, 0, 1}, AccuracyGoal → 4];
  DμDn = Interpolation[Table[{i, D[μdenBCS[x, n], n] /. n → i}, {i, 0.01, 10, .01}]];
  cc = √(1/2 NIntegrate[r denμ[μrep - r^2], {r, 0, √μrep}] / NIntegrate[r (DμDn[denμ[μrep - r^2]])^-1, {r, 0, √μrep}]);
  BCSList = Append[BCSList, {x, cc}];
  Print[x];
 }]
```

```
BECList
```

```
{{-2., 0.376198}, {-1.8, 0.374537}, {-1.6, 0.372519}, {-1.4, 0.370026}, {-1.2, 0.366894}, {-1., 0.362893}, {-0.8, 0.357709}, {-0.6, 0.350938},
 {-0.4, 0.34216}, {-0.2, 0.331188}, {-2.77556×10^-16, 0.318535}, {0.2, 0.305452}, {0.4, 0.292971}, {0.6, 0.281812}, {0.8, 0.272057}, {1., 0.263578},
 {1.2, 0.256193}, {1.4, 0.24972}, {1.6, 0.244005}, {1.8, 0.23892}, {2., 0.234361}, {2.2, 0.230244}, {2.4, 0.226502}, {2.6, 0.223077},
 {2.8, 0.219929}, {3., 0.217021}, {3.2, 0.214322}, {3.4, 0.211808}, {3.6, 0.209455}, {3.8, 0.207248}, {4., 0.205171}, {4.2, 0.203211},
 {4.4, 0.201356}, {4.6, 0.199597}, {4.8, 0.197925}, {5., 0.196331}, {5.2, 0.19481}, {5.4, 0.193356}, {5.6, 0.217525}, {5.8, 0.190633}, {6., 0.189351}}
```

```
BCSList
```

```
{{-2., 0.426386}, {-1.8, 0.4243}, {-1.6, 0.421786}, {-1.4, 0.418717}, {-1.2, 0.41492}, {-1., 0.410168}, {-0.8, 0.404168}, {-0.6, 0.39659},
 {-0.4, 0.387145}, {-0.2, 0.375782}, {-2.77556×10^-16, 0.3631}, {0.2, 0.35009}, {0.4, 0.337408}, {0.6, 0.325815}, {0.8, 0.315464}, {1., 0.306303},
 {1.2, 0.298201}, {1.4, 0.29102}, {1.6, 0.284609}, {1.8, 0.278864}, {2., 0.273682}, {2.2, 0.26898}, {2.4, 0.264689}, {2.6, 0.260753},
 {2.8, 0.257124}, {3., 0.253765}, {3.2, 0.250641}, {3.4, 0.247727}, {3.6, 0.244998}, {3.8, 0.242435}, {4., 0.240021}, {4.2, 0.23774}, {4.4, 0.235582},
 {4.6, 0.233533}, {4.8, 0.231585}, {5., 0.229729}, {5.2, 0.227957}, {5.4, 0.226264}, {5.6, 0.224642}, {5.8, 0.223087}, {6., 0.221594}}
```

```
SoundBEC = Interpolation[BECList];
SoundBCS = Interpolation[BCSList];

μGBEC[x_] := 1/4 (5/2 .6/x)^(2/5)

BECTheory[x_] := 1/2 √μGBEC[x]

Data = Import["C:\Users\Owner\Documents\Thesis\data.txt", "TSV"];
SoundData = Table[{Data[[All, 8]][[i]], Data[[All, 6]][[i]]}, {i, 2, Length[Data[[All, 6]]]}];

p1 = Plot[SoundBCS[x], {x, -2, 1}, PlotStyle → {Blue, Thickness[0.003]}];
p2 = Plot[SoundBCS[x], {x, 1, 5}, PlotStyle → {Blue, Thickness[0.003], Dashed}];
p3 = Plot[SoundBEC[x], {x, -2, 1}, PlotStyle → {Red, Thickness[0.003], Dashed}];
p4 = Plot[SoundBEC[x], {x, 1, 5}, PlotStyle → {Red, Thickness[0.003]}];
p5 = Plot[BECTheory[x], {x, 0, 5}, PlotStyle → {Purple, Thickness[0.003]}, PlotRange → {{-1.5, 5}, {.15, .55}}];
p6 = ListPlot[{{0, 1/√5 (1 - 0.561)^(1/4)}}, PlotStyle → {Black, PointSize[0.02]}];
p7 = ListPlot[{{0, 0}, {0, 1}}, PlotStyle → {Black}, Joined → True];

Show[p1, p2, p3, p4, p5, p6, p7, PlotRange → {{-1.5, 5}, {.15, .525}}, Axes → False, Frame → True, FrameLabel → {1/"k_F" <> "a", "c"/"v_F", , },
 FrameStyle → Directive[32, FontFamily → "Helvetica", Thickness[0.002]], RotateLabel → False]
```

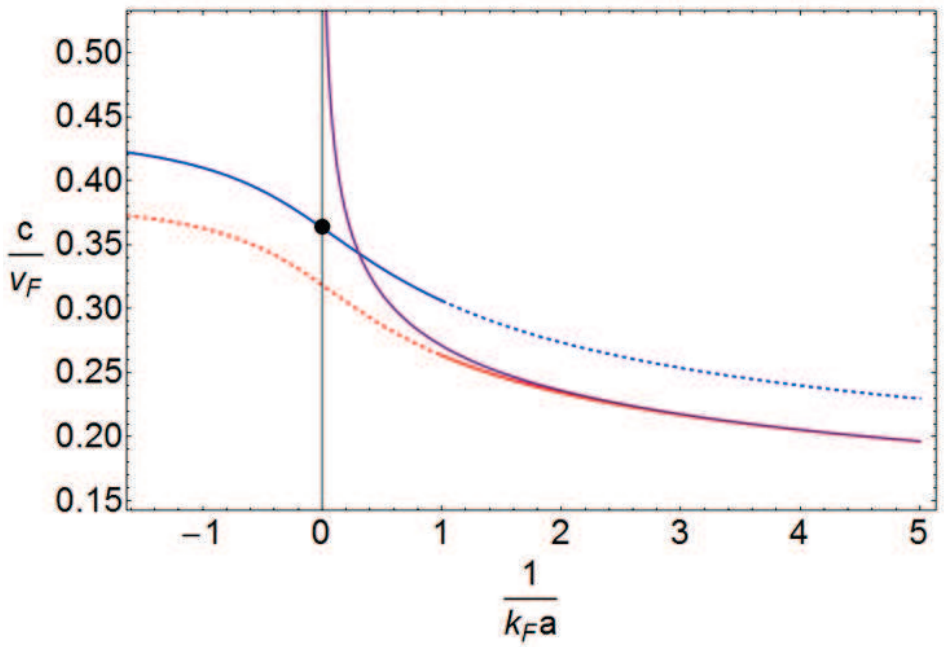

Bibliography

[1] M. Riordan and L Hoddeson *Crystal Fire.* W. W. Norton and Company, New York, First Edition, 1997.

[2] M. H. Anderson, J. R. Ensher, M. R. Matthews, C. E. Wieman, and E. A Cornell. Observation of Bose-Einstein condensation in a dilute atomic vapor. *Science*, 269:198 1995.

[3] K. B Davis, M. O. Mewes, M. R. Andrews, N. J. van Druten, D. S. Durfee, D. M. Kurn, and W. Ketterle. Bose-Einstein condensation in a gas of sodium atoms. *Phys. Rev. Lett.*, 75:3969, 1995.

[4] C. C. Bradley, C. A. Sackett, J. j. Tollett, and R. G. Hulet. Evidence of Bose-Einstein concensation in an atomic gas with attractive interactions. *Phys. Rev. Lett.*, 75:1687, 1995.

[5] B. DeMarco and D. S. Jin. Onset of Fermi degeneracy in a trapped atomic gas. *Science*, 285:1703, 1999.

[6] S. R. Granade, M. E. Gehm, K. M. O'Hara, and J. E. Thomas. All-Optical Production of a Degenerate Fermi Gas". *Phys. Rev. Lett.*, 88:120405 2002

[7] L. N. Cooper. Bound electron pairs in a degenerate Fermi gas. *Phys. Rev.*, 104:1189, 1956.

[8] F. Schreck, L. Khaykovich, K. L. Corwin, G. Ferrari, T Bourdel, J. Cubizolles, and C. Salomon. Quasipure Bose-Einstein Condensate Immersed in a Fermi Sea. *Phys. Rev. Lett.*, 87:080403, 2001.

[9] A. G. Truscott, K. E. Stecker, W. I. McAlexander, G. B. Partridge, and R. G. Hulet. Observation of Fermi Pressure in a Gas of Trapped Atoms. *Science*, 291:2570, 2001.

[10] T. Köhler, K. Goral, and P.S. Julienn. Production of cold molecules via magnetically tunable Feshbach resonances. *Rev. Mod. Phys.*, 78:1311, 2006.

[11] T. L. Ho. Universal thermodynamics of degenerate quantum gases in the unitary limit. *Phys. Rev. Lett.*, 92:090402.

[12] G. A. Baker Jr. Neutron matter model. *Phys. Rev. C.*, 60:054311, 1999.

[13] J. E. Thomas, J. Kinast, and A. Turlapov. Virial theorem and Universality in a Unitary Fermi Gas *Phys. Rev. Lett.*, 95:120402 2005.

[14] K. M. O'Hara, S. L. Hemmer, M. E. Gehm, S. R. Granade, and J. E. Thomas. Observation of a strongly interacting degenerate Fermi gas of atoms. *Science*, 251:1194, 1991.

[15] J. Kinast, S. L. Hemmer, M. E. Gehm, A. Turlapov, and J. E. Thomas. Evidence for Superfluidity in a Resonantly Interacting Fermi Gas. *Phys. Rev. Lett.*, 92:150402, 2004.

[16] M. W. Zwierlein, J. R. Abo-Shaeer, A. Chirotzek, C. H. Schunck, and W. Ketterle. Vortices and superfluidity in a strongly interacting Fermi gas. *Nature*, 435:1047, 2005.

[17] P.Nozieres and S. Schmtt-Rink. Bose condensation in an attractive fermion gas: From weak to strong coupling superconductivity. *J. Low Temp. Phys.*, 59:195 (1985).

[18] S. Giorgini, L. P. Pitaevskii, S. Stringari. Theory of ultracold atomic Fermi gases. *Rev. Mod. Phys.*, 80:1215, 2008.

[19] J. Joseph, B. Clancy, L. Lu, J. Kinast, A. Turlapov, and J. E. Thomas. Measurement of sound velocity in a Fermi gas near a Feshbach resonance. *Phys. Rev. Lett.*, 98:170401, 2007.

[20] S. N. Bose. Plancks Gesetz und Lichtquantenhypothese *Zeitschrift fr Physik*, 26:178, 1924

[21] A. Einstein. Quantentheorie des einatomigen idealen Gases. *Sitzungsberichte der Preussischen Akademie der Wissenschaften*, 1:3, 1925.

[22] D. M. Eagles. Possible Pairing without Superconductivity at Low Carrier Concentrations in Bulk and Thin-Film Superconducting Semiconductors. *Phys. Rev.*, 186:456, 1969.

[23] A. L. Migdall, J. V. Prodan, W. D. Phillips, T. H. Bergeman, and H. J. Metcalf. First observation of magnetically trapped neutral atoms. *Phys. Rev. Lett.*, 54:2596, 1985.

[24] H. J. Metcalf and P. van der Straten. *Laser Cooling and Trapping*. Springer, New York, 1999.

[25] G. F. Bertsch proposed the problem of determining the ground state of a two-component Fermi gas with a long scattering length.

[26] F. Dalfovo, S. Giorgini, L. P. Petaevskii, S. Stringari. Theory of Bose-Einstein condensation in trapped gases. *Rev. Mod. Phys.*, 71:463, 1999.

[27] A. J. Legget. Diatomic molecules and cooper pairs. *Modern Trends in the Theory of Condensed Matter*, 115:13, 1980.

[28] A Simple Mean Field Model

[29] D.S. Petrov, C. Salomon, and G.V. Shlyapnikov. Weakly Bound Dimers of Fermionic Atoms. *Phys. Rev. Lett.*, 93:090404, 2004.

[30] G. E. Astrakharchik, J. Boronat, J. Cassulleras, and S. Giorgini. Equation of state of a Fermi gas in the BEC-BCS crossover: A quantum monte carlo study. *Phys. Rev. Lett.*, 93:200404, 2004.

[31] S.Y. Chang, V. R. Pandharipande, J. Carlson, and K. E. Schmidt. Quantum Monte-Carlo studies of superfluid Fermi gases. *Phys. Rev. A*, 70:043602, 2004.

[32] K. A. Olive. The quark-hadron transition in cosmology and astrophysics. *Science*, 251:2179, 1991.

[33] U. Heinz. The quark-gluon plasma at RHIC. *Nucl. Phys. A*, 721:30, 2003.

[34] A. Turlapov, J. Kinast, B. Clancy, L. Luo, J. Joseph, and J. E. Thomas. Is a gas of strongly interacting atomic fermions a nearly perfect fluid? *Jour. Low Temp. Phys.*, 150:567, 2008.

[35] J. E. Thomas, Is an Ultra-Cold Strongly Interacting Fermi Gas a Perfect Fluid? *Nucl. Phys. A*, 830:665c, 2009.

[36] H. Heiselberg, Fermi systems with long scattering lengths, *Phys. Rev. A*, 63:043606, 2001.

[37] C. W. Chu. Superconductivity above 150 K in $HgBa_2Ca_2Cu_{3O8} + \overline{o}$ at high pressures. *Nature* 365:323, (1993).

[38] J. Bardeen, L. N. Cooper, and J. R. Schrieffer. Theory of superconductivity. *Phys Rev.* 108(5):1175, 1957.

[39] M. Houbiers and H. T. C. Stoof. Cooper-pair formation in trapped atomic Fermi gases. *Phys. Rev. A*, 59:1556, 1999.

[40] M. Holland, S. J. J. M. F. Kokkelmans, M. L. Chiofalo, and R. Wasler. Resonance superfluidity in a quantum degenerate Fermi gas. *Phys. Rev. Lett.*, 87:120406

[41] S. J. J. M. F. Kokkelmans, J. N. Milstein, M. L. Chiogalo, R. Wasler, and M. J. Holland. Resonance superfluidity: renormalization of resonance scattering theory. *Phys. Rev. A*, 65:053617, 2002.

[42] J. Stajic, J. N. Mistein, Q. Chen, M. L. Chiofalo, M. J. Holland, and K. Levin. Nature of superfluidity in ultracold Fermi gases near Feshbach resonances. *Phys. Rev. A*, 69:063610 2004.

[43] A. Perali, P. Pieri, L. Pisani, and G. C. Strinati. BCS-BEC crossover at finite temperature for superfluid trapped Fermi atoms. *Phys. Rev. Lett.*, 92:220404, 2004.

[44] J. Kinast, A. Turlapov, J. E. Thomas, Qijin Chen, J. Stajic, and K. Levin. Heat capacity of a strongly interacting Fermi gas. *Science*, 307:1296, 2005.

[45] L. Luo, B. Clancy, J. Joseph, J. Kinast, and J. E. Thomas. Measurement of the Entropy and Critical Temperature of a Strongly Interacting Fermi Gas. *Phys. Rev. Lett.*, 98:080402, 2007.

[46] H. Heiselberg. Sound Modes in the BCS-BEC Crossover. *Phys. Rev. A* 73:014607, 2006.

[47] T. Bourdel, L. Khaykovich, J. Cubizolles, J. Zhang, F. Chevy, M. Teichmann, L. Tarruell, S. J. J. M. F. Kokkelmans, and C. Salomon. Experimental Study of the BEC-BCS Crossover Region in Lithium 6. *Phys. Rev. Lett.*, 93:050401, 2004.

[48] C. A. Regal, M. Greiner, S. Giorgini, M. Holland, and D. S. Jin. Momentum Distribution of a Fermi Gas of Atoms in the BCS-BEC Crossover. *Phys. Rev. Lett.*, 95:250404, 2005.

[49] M. Bartenstein, A. Altmeyer1, S. Riedl, S. Jochim, C. Chin, J. Hecker Denschlag, and R. Grimm. Crossover from a Molecular Bose-Einstein Condensate to a Degenerate Fermi Gas. *Phys. Rev. Lett.*, 92:120401, 2004.

[50] M. L. Chiofalo, S. Giorgini, and M. Holland. Released Momentum Distribution of a Fermi Gas in the BCS-BEC Crossover. *Phys. Rev. Lett.*, 97:070404, 2006.

[51] Jelena Stajic, Qijin Chen, and K. Levin. Density Profiles of Strongly Interacting Trapped Fermi Gas. *Phys. Rev. Lett.*, 94:060401, 2005.

[52] J. Kinast, S. L. Hemmer, M. E. Gehm, A. Turlapov, and J. E. Thomas. Evidence for Superfluidity in a Resonantly Interacting Fermi Gas. *Phys. Rev. Lett.*, 92:150402, 2004.

[53] M. Bartenstein, A. Altmeyer1, S. Riedl, S. Jochim, C. Chin, J. Hecker Denschlag1, and R. Grimm. Collective Excitations of a Degenerate Gas at the BEC-BCS Crossover. *Phys. Rev. Lett.*, 92:203201, 2004.

[54] J. Kinast, A. Turlapov, and J. E. Thomas. Breakdown of hydrodynamics in the radial breathing mode of a strongly interacting Fermi gas. *Phys. Rev. A*, 70:051401(R), 2004.

[55] A. Altmeyer, S. Riedl, C. Kohstall, M. J. Wright, R. Geursen, M. Bartenstein, C. Chin, J. Hecker Denschlag, and R. Grimm. Precision Measurements of Collective Oscillations in the BEC-BCS Crossover. *Phys. Rev. Lett.*, 98:040401, 2007.

[56] Hui Hu, A. Minguzzi, Xia-Ji Liu, and M. P. Tosi. Collective Modes and Ballistic Expansion of a Fermi Gas in the BCS-BEC Crossover. *Phys. Rev. Lett.*, 93:190403, 2004.

[57] G. E. Astrakharchik, R. Combescot, X. Leyronas, and S. Stringari. Equation of State and Collective Frequencies of a Trapped Fermi Gas Along the BEC-Unitarity Crossover. *Phys. Rev. Lett.*, 95:030404, 2005.

[58] P. Capuzzi, P. Vignolo, F. Federici, and M. P. Tosi. Sound propagation in elongated superfluid fermionic clouds. *Phys. Rev. A*, Phys. Rev. A 73:021603(R) 2006.

[59] T. K. Ghosh and K. Machida. Sound velocity and multibranch Bogoliubov spectrum of an elongated Fermi superfluid in the BEC-BCS crossover. *Phys. Rev. A*, 73:013613, 2006.

[60] A. Perali, P. Pieri, and G. C. Strinati. Quantitative Comparison between Theoretical Predictions and Experimental Results for the BCS-BEC Crossover. *Phys. Rev. Lett.*, 93:100404, 2004.

[61] Aurel Bulgac and George F. Bertsch. Collective Oscillations of a Trapped Fermi Gas near the Unitary Limit. *Phys. Rev. Lett.*, 94:070401, 2005.

[62] M. E. Ghem. *Preparation of an Optically-trapped Degenerate Fermi gas of ^{6}Li: Finding the Route to Degeneracy*. PhD thesis, Duke University 2003.

[63] S. R. Granade. *All-optical Production of a Degenerate gas of ^{6}Li: Characterization of Degeneracy*. PhD thesis, Duke University, 2002.

[64] K. M. O'Hara. *Optical Trapping and Evaporative Cooling of Fermionic Atoms.* PhD thesis, Duke University, 2000.

[65] J. M. Kinast *Thermodynamics and Superfluidity of a Strongly Interacting Fermi Gas* PhD thesis, Duke University, 2006.

[66] Le Luo. *Entropy and Superfluid Critical Parameters of a Strongly Interacting Fermi gas* PhD thesis, Duke University, 2008.

[67] B. E. Clancy *Hydrodynamics of a Rotating Strongly Interacting Fermi Gas.* PhD thesis, Duke University, 2008.

[68] W.L. Wiese, M. W. Smith, B. M. Glennon, Atomic Transition Probabilities, National Standard Reference Data Series, National Bureau of Standards 4, May 20 1966.

[69] R. K. Pathria. *Statistical Mechanics.* Butterworth-Heinermann, Boston, 2nd edition, 1996.

[70] R Shankar. *Principles of Quantum Mechanics.* Plenum, New York, 2nd edition, 1994.

[71] J.J. Sakurai. *Modern Quantum Mechanics* Addison-Wesley, New York, revised edition, 1994.

[72] C. Cohen-Tannoudji, B. Diu, and F. Laloë. *Quantum Mechanics, Volume One.* John Wiley & Sons, New York, 1977.

[73] D. A. Butts, D. S. Rokhsar. Trapped Fermi gases. *Phys. Rev. A*, 55:4346, 1997.

[74] M. Houbiers, H. T. C. Stoof, W. I. McAlexander, and R. G. Hulet. Eleastic and ineleastic collisions of 6Li atoms in magnetic and optical traps. *Phys. Rev. A*, 57:R1497.

[75] M. Bartenstein, A. Altmeyer, S. Riedl, R. Geursen, S. Jochim, C. Chin, J. H. Denschlag, R. Grimm, A. Simoni, E. Tiesinga, C. J. Williams, and P. S. Julienne. Percise determination of ^{6}Li atoms in magnetic and optical traps. *Phys. Rev. Lett.*, 94:103201, 2005.

[76] M. Bertenstein, A. Altmeyer, S. Riedl, R. Geursen, S. Jochim, C. Chin, J. Hecker Denshlag, and R. Grimm. A simoni, E. Tiesinga, C.J. Williams, and P.S. Jilienne. Percise Determination of 6Li Cold Collision Parameters by Radio Frequency Spectroscopy and Weakly Bound Molecules. *Phys. Rev. Lett.*, 94:103201.

[77] A. Bulgac, J.E. Drut, and P. Magierski. Spin 1/2 fermions in the unitary regime: A superfluid of a new type. *Phys. Rev. Lett.*, 96:023617, 2006.

[78] J. Carlson, S.Y. Chang, V. R. Pandharipande, and K. E. Schmidt. Superfluid Fermi gases with large scattering length. *Phys. Rev. Lett.*, 91:050401.

[79] K.M. O'Hara, M.E. Ghem, S.R. Granade and J.E. Thomas. Scaling laws for evaporative cooling in time-dependent optical traps. *Phys. Rev. A*, 64:051403(R), 2001.

[80] Ingrid Thesis

[81] C. Kittel and H. Kroemer. *Thermal Physics*, W.H. Freeman and Company, New York, 2nd edition, 1980.

[82] C. Kittel. *Elementary Statistical Physics*, W.H. Freeman and Company, New York, 2nd edition, 1980.

[83] X. Du, L. Lu, B. Clancy, and J. E. Thomas. Observation of Anomalous Spin Segregation in a Trapped Fermi Gas. *Phys. Rev. Lett.*, 101:150401, 2008.

[84] M. Bartenstein, A. Altmeyer, S. Riedl, R. Geursen, S. Johim, C. Chin, J. Hecker Denschlag, and R. Grimm. A. Simoni, E. Tiesinga, C. J. WIlliams, and P. S. Julienne. Percise Determination of ^{6}Li Cold Collsion Parameters by Radio-Frequency Spectroscopy on Weakly Bound Molecules. *Phys. Rev. Lett.*, 94:103201, 2005.

[85] C. Chin, M. Bartenstein, A. Altmeyer, S. Riedl, S. Jochim, J. Hecker Denschlag, and R. Grimm. Observation of the Pairing Gam in a Strongly Interacting Fermi Gas. *Science*, 305:5687, 2004.

[86] G. B. Partridge, Wenhui Li, R. I. Kamar, Yean-an Liao, and R. G. Hulet. Pairing and Phase Separation in a Polarized Fermi Gas. *Science*, 311:5760, 2006.

[87] J. R. Taylor, *An Introduction to Error Analysis: The Study of Uncertainties if Physical Measurements*, University Science Books, 1982.

Biography

James Adlai Joseph was born December 29, 1978 in Chicago IL. After graduating from New Trier High School in 1997 he enrolled in the Pratt School of Engineering at Duke University. He graduated with a combined B.S.E in Electrical Engineering as Physics In May 2001. As an undergraduate we conducted an independent study into the properties of photonic crystals under the guidance of Professor Henry Everitt. In August 2001 he worked as a physicist for BNFL Inc. in Santa Fe New Mexico. There he was involved in multiple government nuclear decommissioning projects and worked in a managing capacity as well. In 2002 he continued his work as a consultant working from Chicago. In August 2003 he was accepted into the graduate school at Duke, pursuing a Ph.D. in Physics. In June 2004 he joined the quantum optics group lead by Professor John Thomas. There he conducted experiments measuring the sound velocity in ultracold Fermi gases. He received both the Firtz London Fellowship as well as the John Chambers Fellowship in 2008 before graduating with a Ph.D. in May 2010.

Publications

A. Turlapov, J. Kinast, B. Clancy, L. Luo, J. Joseph, and J. E. Thomas, "Is a gas of strongly interacting atomic fermions a nearly perfect fluid?," *Journal of Low Temperature Phyics* **150** 567 (2008)

J. Joseph, B. Clancy, L. Luo, J. Kinast, A. Turlapov, and J. E. Thomas, "Measurement of sound velocity in a Fermi gas near a Feshbach resonance," *Physical Review Letters*, **98**, 170401 (2007).

L. Luo, B. Clancy, J. Joseph, J. Knast, and J. E. Thomas, "Measurement of the entroy and critical temperature of a strongly interacting Fermi gas," *Physical Review Letters*, **98**, 080402 (2007).

L. Luo, B. Clancy, J. Joseph, J Kinast, and J. E. Thomas, "Evaporative cooling of a unitary Fermi gas mixtures in optical traps" *New Journal of Physics*, **8**, 213 (2006).

Selected Presentations

J. Joseph, B. Clancy, L. Luo, and J. E. Thomas. "Sound Propagation in an Trapped Fermi Gas" *Invited talk at University of Chicago.* Chicago, IL, presented by J. Joseph July, 2007.

J. Joseph and J. E. Thomas, "Direct Temperature Probe of Strongly Interacting and other Trapped Gases" *Invited talk at University of Chicago.* Chicago, IL, presented by J. Joseph January, 2009.